

(2)

AD-A198 56

DTIC FILE COPY

Air Flow Through a Deciduous Forest Edge Using High Frequency Anemometry



Final Technical Report

Harold W. Thistle, Jr.

June 1, 1988

U.S. Army Research Office
Grant Number DDA103-86-K-0081

DTIC
ELECTE
S AUG 1 2 1988 D
H

D.R. Miller and J.D. Lin, Principal Investigators
Departments of Natural Resources Management and Engineering and
Civil Engineering
The University of Connecticut
Storrs, Connecticut 06268

Approved for Public Release — Distribution Unlimited

Research in Microclimate at the Forest-Urban Interface, Progress Rpt #13

REPORT DOCUMENTATION PAGE

1a. REPORT SECURITY CLASSIFICATION <u>Unclassified</u>		1b. RESTRICTIVE MARKINGS	
2a. SECURITY CLASSIFICATION AUTHORITY		3. DISTRIBUTION/AVAILABILITY OF REPORT Approved for public release; distribution unlimited.	
2b. DECLASSIFICATION/DOWNGRADING SCHEDULE		5. MONITORING ORGANIZATION REPORT NUMBER(S) ARO 23446.3-GS	
4. PERFORMING ORGANIZATION REPORT NUMBER(S)		7a. NAME OF MONITORING ORGANIZATION U. S. Army Research Office	
6a. NAME OF PERFORMING ORGANIZATION U. of Connecticut		7b. ADDRESS (City, State, and ZIP Code) P. O. Box 12211 Research Triangle Park, NC 27709-2211	
6b. OFFICE SYMBOL (If applicable)		9. PROCUREMENT INSTRUMENT IDENTIFICATION NUMBER DAAL03-86-K-0081	
8a. NAME OF FUNDING/SPONSORING ORGANIZATION U. S. Army Research Office		10. SOURCE OF FUNDING NUMBERS	
8b. OFFICE SYMBOL (If applicable)		PROGRAM ELEMENT NO.	
8c. ADDRESS (City, State, and ZIP Code) P. O. Box 12211 Research Triangle Park, NC 27709-2211		PROJECT NO.	
		TASK NO.	
		WORK UNIT ACCESSION NO.	
11. TITLE (Include Security Classification) Air Flow Through a Deciduous Forest Edge Using High Frequency Anemometry			
12. PERSONAL AUTHOR(S) Harold W. Thistle, Jr. (author of report) D. R. Miller & J. D. Lin (principal investigator)			
13a. TYPE OF REPORT Final		13b. TIME COVERED FROM 5/1/86 TO 4/30/88	
14. DATE OF REPORT (Year, Month, Day) June 1, 1988		15. PAGE COUNT 211	
16. SUPPLEMENTARY NOTATION The view, opinions and/or findings contained in this report are those of the author(s) and should not be construed as an official Department of the Army position, policy, or decision, unless so designated by other documentation.			
17. COSATI CODES		18. SUBJECT TERMS (Continue on reverse if necessary and identify by block number)	
FIELD	GROUP	SUB-GROUP	
		from 19 → Air Flow, Deciduous Forest, Sensors, Foliage, Turbulence, Foliated Canopys, Terrain, Canopy Elements (Aw)	
19. ABSTRACT (Continue on reverse if necessary and identify by block number) → The air flow field through a deciduous forest edge was measured. Measurement was accomplished using orthogonal hot-film anemometers coupled with a direction sensor. This measurement system is called a TFWOES (Triple Film, Wind Octant Electronic Sensor). High frequency temperature data was also collected. → next page			
20. DISTRIBUTION/AVAILABILITY OF ABSTRACT <input type="checkbox"/> UNCLASSIFIED/UNLIMITED <input type="checkbox"/> SAME AS RPT. <input type="checkbox"/> DTIC USERS		21. ABSTRACT SECURITY CLASSIFICATION Unclassified	
22a. NAME OF RESPONSIBLE INDIVIDUAL		22b. TELEPHONE (Include Area Code)	
		22c. OFFICE SYMBOL	

→ Measurements are presented primarily for near-neutral conditions and indicate the role of foliage and the edge on this flow field. The edge displaces the mean flow upward but also acts as a longitudinal momentum source in the foliage in edge fetch flows. This flow is extremely complex with highest turbulent intensities in the trunk space. Spectral analysis indicates that there is increased spectral density here at length scales possibly corresponding to the height of the edge, local terrain and canopy elements. Comparison of the foliated and unfoliated flows indicates that the air is less effective penetrating the foliated canopy because of increased drag but that the relationship between foliage density and drag coefficient is complicated. *Keywords: → to field 18*

AIR FLOW THROUGH A DECIDUOUS FOREST EDGE USING HIGH FREQUENCY
ANEMOMETRY

Final Technical Report

Harold W. Thistle, Jr.

June 1, 1988

U. S. Army Research Office
Grant Number DDA103-B6-K-0081

D. R. Miller and J. D. Lin, Principal Investigators
Departments of Natural Resources Management and Engineering and
Civil Engineering
The University of Connecticut
Storrs, Connecticut 06268

Approved for Public Release - Distribution Unlimited

Research in Microclimate at the Forest-Urban Interface, Progress
Rpt #13

THE VIEW, OPINIONS, AND /OR FINDINGS CONTAINED IN THIS REPORT ARE THOSE OF THE AUTHOR AND SHOULD NOT BE CONSTRUED AS AN OFFICIAL DEPARTMENT OF THE ARMY POSITION, POLICY, OR DECISION, UNLESS SO DESIGNATED BY OTHER DOCUMENTATION.

LIST OF PUBLICATIONS TO DATE

Miller, D. R., J. D. Lin, Y. S. Wang and H. T. Thistle. 1988. A Combination Triple Hot-Film and Wind Octant Probe (TFWOES) for Turbulent Air Flow Measurements in and Near Plant Canopies. Agriculture and Forest Meteorology (In press).

Wang, Y. S. and D. R. Miller. 1987. Calibration of the Hemispherical Photograph Tedhnique to Measure Leaf Area Index Distributions in Hardwood Forests. Forest Sci. 33(1):210-216.

Lin, J. D. and D. R. Miller. 1987. A Spatial Averaging Scheme for Turbulent Flows in a Plant Canopy. Proc. 18th Conf. on Forest and Ag. Meteorology of the AMS. pp 1-2.

Thistle, H. T., D. R. Miller, and J. D. Lin. 1987. Turbulent Fow Characteristics at the Edge of A Foliated and Unfoliated Deciduous Canopy. Proc. 18th Conf. on Forest and Ag. Meteorology of the AMS. pp 179-180.

Li, Z. J., J. D. Lin and D. R. Miller. 1988. Air Flow Over and Through a Forest Edge; A Steady-State Numerical Simulation. Boundary-Layer Meteorology (submitted).

Thistle, H. W. 1988. Description of The Air Flow Through A Deciduous Foest Edge Using High Frequency Anemometry. PhD Dissertation, University of Connecticut. pp 211.

LIST OF PARTICIPATING SCIENTIFIC PERSONNEL

David R. Miller, Professor of Natural Resources
Jia D. Lin, Professor of Civil Engineering
Dean E. Anderson, Assistant Professor of Natural Resources
Harold W. Thistle, Jr. PhD 1988
Y. S. Wang, Research Assistant
M. A. Focazio, Research Assistant
Z. N. Lu, Research Assistant

ABSTRACT

The air flow field through a deciduous forest edge was measured. Measurement was accomplished using orthogonal hot-film anemometers coupled with a direction sensor. This measurement system is called a TFWOES (Triple Film, Wind Octant Electronic Sensor). High frequency temperature data was also collected.

Measurements are presented primarily for near-neutral conditions and indicate the role of foliage and the edge on this flow field. The edge displaces the mean flow upward but also acts as a longitudinal momentum source in the foliage in edge fetch flows. This flow is extremely complex with highest turbulent intensities in the trunk space. Spectral analysis indicates that there is increased spectral density here at length scales possibly corresponding to the height of the edge, local terrain and canopy elements. Comparison of the foliated and unfoliated flows indicates that the air is less effective penetrating the foliated canopy because of increased drag but that the relationship between foliage density and drag coefficient is complicated.

Accession For	
NTIS GRA&I	<input checked="checked" type="checkbox"/>
DTIC TAB	<input type="checkbox"/>
Unannounced	<input type="checkbox"/>
Justification	
By _____	
Distribution/	
Availability Codes	
Dist	Avail and/or Special
A-1	

QUALITY
INSPECTED
2

Table of Contents

Introduction	1
Literature Review	3
Instrumentation	26
Experimental Design	60
Statistical Methods	71
Results and Discussion	99
Conclusions	198

Bibliography	201
---------------------------	------------

Appendix A Software Systems	209
--	------------

List of Figures

Figure 1.	58
Figure 2.	59
Figure 3.	69
Figure 4.	70
Figure 5.	98
Figure 6.	151
Figure 7.	152
Figure 8.	153
Figure 9.	154
Figure 10.	155
Figure 11.	156
Figure 12.	157
Figure 13.	158
Figure 14.	159
Figure 15.	160
Figure 16.	161
Figure 17.	162
Figure 18.	163

Figure 19.	164
Figure 20.	165
Figure 21.	166
Figure 22.	167
Figure 23.	168
Figure 24.	169
Figure 25.	170
Figure 26.	171
Figure 27.	172
Figure 28.	173
Figure 29.	174
Figure 30.	175
Figure 31.	176
Figure 32.	177
Figure 33.	178
Figure 34.	179
Figure 35.	180
Figure 36.	181
Figure 37.	182
Figure 38.	183
Figure 39.	184
Figure 40.	185
Figure 41.	186
Figure 42.	187

Figure 43.	188
Figure 44.	189
Figure 45.	190
Figure 46.	191
Figure 47.	192
Figure 48.	193
Figure 49.	194
Figure 50.	195
Figure 51.	196
Figure 52.	197

SYMBOL LIST

A = area (m^2)

ASL = atmospheric surface layer

a_r = discrete Fourier coefficient

B = Bowen ratio

b_r = discrete Fourier coefficient

C_D = drag coefficient

$C(\omega)$ = co-spectral function

c_p = specific heat ($Jkg^{-1}^{\circ}K^{-1}$)

$D(t)$ = digital detection function

d = zero plane displacement (m)

d_L = characteristic length (m)

E = voltage (V)

F_D = drag force (kg ms^{-2})

f = frequency (s^{-1})

f = dimensionless frequency

g = acceleration of gravity (ms^{-1})

$g(\omega)$ = continuous Fourier coefficient

H = vertical heat flux (W m^{-2})

H = hole size in quadrant analysis

h = canopy height (m)

h_c = coefficient of convective heat transfer

h_p = pitch factor

I = current (Amps)

$I_{i,H}$ = intermittency function (Eqn. 5.42)

K_M = turbulent transfer coefficient of momentum

K_V = quantity threshold value

k = wave number (m^{-1})

k_H = thermal diffusivity m^2s^{-1}

k_s = von Karman's constant ($\sim .4$)

k_y = yaw factor

$k(\omega)$ = continuous Fourier coefficient

L = length of wire (m)

L = Eq 5.49

$L_{sub s}$ = scaling length (m) (Eq 1.28)

l_c = local mixing length (m)

N = number of data points

N_f = Nyquist frequency (s^{-1})

n = frequency (s^{-1})

P = period (s)

PBL = planetary boundary layer

p = static pressure (Nm^{-2})

Q = scalar quantity

Q_i = quadrant specifier, $i = 1,4$

$Q(\omega)$ = quadrature spectra function

R = resistance

R_s = autocorrelation function in space

R_t = autocorrelation function in time

$R(\tau)$ = autocorrelation function

Ri = Richardson number

S = Eqn. 2.17b

S_1 = gradient of windspeed in normalized profiles

S_{LH} = Stress fraction (Eqn. 40)

$S(f)$ = spectral density

s = Eqn. 2.17a

T = temperature ($^{\circ}K$)

T_0 = surface temperature ($^{\circ}K$)

T_{LH} = time fraction (Eqn. 5.41)

T_V = time interval (s)

t = time (s)

TI = turbulent intensity

TKE = turbulent kinetic energy m^2s^{-2}

u = air velocity (m s^{-1})

u_h = air velocity at the canopy top (ms^{-1})

u_* = friction velocity (ms^{-1})

v = lateral component of vector air velocity (ms^{-1})

w = vertical component of vector air velocity (ms^{-1})

w_* = Eqn. 2.26

x = space coordinate (m)

z = height (m)

z_i = PBL inversion height (m)

z_0 = roughness length (m)

α = (Eqn. 2.16)

α = damping coefficient (3.31b)

α = horizontal angle between vector and sensor

$\alpha_{i,f}$ = matrix of inter-sensor angles

B = volume coefficient of expansion

$\Gamma(\omega)$ = coherence function

ε = dissipation rate m^2s^{-3}

ε = emissivity

η = Kolmogorov length (m)

Θ = bivariate phase angle

θ = potential temperature ($^{\circ}K$)

θ = yaw angle

θ = phase lag

λ = wavelength (m)

λ_0 = acoustic wavelength (m)

λ_{\max} = maximum wavelength (m)

ξ = displacement (m)

ν = kinematic viscosity (m^2s^{-1})

ρ = density (kg m^{-3})

σ = Stefan - Boltzmann constant ($5.670310^{-8}\text{Wm}^{-2}\text{K}^{-4}$)

σ = standard deviation

τ = lag

τ = shear stress ($\text{kg m}^{-1}\text{s}^{-1}$)

τ = time constant (s)

ϕ = pitch angle

$\phi(\omega)$ = spectral density function

ψ = roll angle

Ω = resistivity

ω = angular frequency (s^{-1})

\angle = direction (360° = due north)

Subscripting and Superscripting Conventions

' (prime, superscripted) = fluctuating portion of quantity

- (overbar, superscripted) = mean portion of quantity

i,j,k (subscripted) = 3-D Cartesian tensor coordinates

Chapter I

Introduction

The purpose of this study is to better understand the interaction of a deciduous forest edge with the ambient air flow. This knowledge is pertinent to all problems of airborne transport in the atmospheric surface layer (ASL). Some applied problems which may be aided by this study are the spraying of insecticides, the transport of pollutants and the dispersion of pheromones.

This interaction will be described in terms of the mean flow, the turbulence, and various analyses which seek to describe the flow in terms of intermittency. Also, gustiness or 'structures' in the flow are investigated. Experiments are conducted in the edge canopy while it is foliated and again when it is unfoliated to directly measure the effect of the foliage on the flow.

Specifically, the goals of this study are:

- 1) To describe the role of the forest edge on the air flow in a mean sense.
- 2) To describe the spectral characteristics of turbulent flow around and through the forest edge.
- 3) To describe the forest edge air flow in terms of events or intermittency.
- 4) To statistically compare results between the foliated and unfoliated edge air flow fields.

The primary instrument system used here is the TFWOES system (Miller, et al., 1988). Since the nature and use of the instrumentation can determine the outcome of this type of experiment, instrumentation is discussed in detail. Due to the complexity of the flow in this forest edge system, every data collection run represents a unique flow field. This is a primary reason that this work has not been done in the past. With this in mind, data is carefully composited and compared to reveal the dominant length scales, the effectiveness of momentum penetration and the structure of the turbulence at the forest edge. Conclusions are successfully drawn and presented based on this process and considerable insight into this flow field is obtained.

Chapter II

Literature Review

2.1 Description and Analysis of Atmospheric Surface Layer Flow

Flow in the atmospheric surface layer (ASL) is turbulent. Turbulent flow may be envisioned as circular random vortices which are convected by the mean flow. In the ASL, the largest vortices are proportional to the depth of the planetary boundary layer (PBL), which is roughly defined as the atmospheric layer influenced by the surface. These large vortices are associated with turbulent production. The larger size of these vortices implies that they will take a longer time to pass a fixed point in an Eulerian system. Thus the period of passage of the vortices is longer and the frequency of passage is lower.

These low frequency vortices decompose into higher frequency vortices. In the absence of further turbulent production, large vortices decompose into vortices of

progressively higher frequency in the cascade of TKE (turbulent kinetic energy). Eventually the vortices become so small that the viscosity (molecular coherence) of the fluid dissipates the remaining TKE into heat. The highest frequency vortices in the flow are lost to dissipation.

Spectral analysis can be used to describe the distribution of vortical frequency in a time series of velocity (see Priestly, 1981 and Chapter 5 for detailed discussions of spectral analysis). Large eddies always breakdown into small eddies. Though this is a stochastic process, when viewed statistically using spectral analysis, this breaking down or cascading of eddies results in a characteristic slope in the graph of frequency versus variance density. This slope should always exist somewhere between the frequency of production and that of dissipation and indicates the inertial sub-range. In the inertial subrange , the density of the variance which occurs at k_1 is given by (Panofsky and Dutton, 1984)

$$S(k_1) = a\epsilon^{2/3} k_1^{-5/3} \quad (2.1)$$

where k_1 is a one-dimensional wave number , ($k_1 = \frac{f}{v}$ where f is frequency and v is velocity), ϵ is the dissipation rate and a is a constant. For a given series of velocity then Eqn. 1.1 can be written as

$$S(k_1) = Ck_1^{-5/3} \quad (2.2)$$

so that the graph of $\log S(k_1)$ versus $\log(k_1)$ will always show a $-5/3$ slope, which characterizes the inertial sub-range and is an important benchmark in the analysis of turbulence.

The end of the inertial sub-range and the beginning of the dissipation range occurs at a length known as the Kolmogorov microscale. This scale is defined as:

$$\eta = \left(\frac{\nu^3}{\epsilon} \right)^{1/4} \quad (2.3)$$

where ν is the fluid viscosity. In a neutral atmosphere, ϵ may be estimated by

$$\epsilon = \frac{u_*^3}{k_a z} \quad (2.4)$$

where k_a is the von Karman constant (approximately .4) and z is the height. u_* is the friction velocity defined in a neutral atmosphere over a smooth surface

$$u_* = k_a z \frac{du}{dz} \quad (2.5)$$

where u is the horizontal velocity. Note that ϵ is a function of height and air velocity. Typically, η is on the order of 1 mm in the atmosphere (Panofsky and Dutton, 1984) making it difficult to verify empirically.

The low frequency vortices in the atmospheric surface layer (ASL) show maximum wavelengths (λ_{\max}) on the order of the thickness of the planetary boundary layer (PBL, Kaimal, et al., 1976). This thickness is defined as the height to the first temperature inversion or capping inversion (z_i). Since z_i is strongly dependent on the direction and the magnitude of the surface heat flux, H , PBL thickness is a strong function of atmospheric stability (Caughey, 1982). Thus λ_{\max} in the ASL is also dependent on stability (Kaimal, 1972).

In the inertial sub-range, the differences in Eq 2.1 between velocity components (u, v, w representing the longitudinal, lateral and vertical components, respectively)

are compensated for by adjusting the constant a . In the energy containing range the spectra of u and v scale with stability, but the spectra of the vertical velocity (w) scales with the dimensionless height ($\frac{z}{z_i}$) (Kaimal et al., 1976). λ_{max} in the w -spectra shifts to shorter wavelengths as $\frac{z}{z_i}$ decreases because vertical velocity fluctuations are disrupted at the surface.

Another method of investigating the size of the dominant vortices in a flow is through correlation analysis. The integral scale of a velocity time series is defined as:

$$T = \int_0^{\infty} R(\tau) d\tau \quad (2.6)$$

where $R(\tau)$ is the auto-correlation coefficient of the series with lag τ . If the graph of $R(\tau)$ versus τ for a given series is examined, the number of lags that $R(\tau)$ remains significant can be interpreted as the length of the dominant vortices in the flow. The transposition of time and length (space) implicit in this interpretation is formalized by Taylor's hypothesis (Lumley and Panofsky, 1963). Using the temporal and spatial auto-correlation functions, this idea can be represented as

$$R_s(\bar{u}\tau) = R_t(\tau) \quad (2.7)$$

where $R_s(\tau)$ is the spatial autocorrelation function and $R_t(\tau)$ is the temporal autocorrelation function. This hypothesis is useful because it allows inference about spatial structure of the flow from point measurements. The usefulness of Taylor's hypothesis in the ASL is limited by the fact that it assumes a stationary flow (constant mean). Usefulness is further limited by the fact that there are multiple length

scales of importance in the ASL due to terrain and the heterogeneity of vegetative canopies.

Mathematically $R(\tau)$ is related to the spectra function $S(f)$ by the Fourier transform:

$$S(f) = \int_0^{\infty} R(\tau) e^{-i2\pi f\tau} d\tau \quad (2.8)$$

so similar information is attained by either analysis. It has become convention in PBL research to focus on spectral analysis.

From an analytical standpoint, a mean velocity profile over a smooth surface in a neutral surface layer may be derived (following Panofsky and Dutton, 1984) using

$$\frac{\tau}{k_a u_* z \rho} = \frac{\partial u}{\partial z} \quad (2.9)$$

and

$$u_* = \left(\frac{\tau}{\rho} \right)^{1/2} \quad (2.10)$$

Substituting Eq 2.10 into Eq 2.9 yields

$$\frac{\partial u}{\partial z} = \frac{u_*}{k_a z} \quad (2.11)$$

which is a rearrangement of Eq 2.5. If we integrate this result then

$$\bar{u} = \int_{z_0}^z \frac{u_*}{k_a z} dz \quad (2.12)$$

then

$$\bar{u} = \frac{u_*}{k_a} \ln\left(\frac{z}{z_0}\right) \quad (2.13)$$

Eq 2.13 is often referred to as the logarithmic wind profile. Over tall roughness elements the mean wind profile departs from the logarithmic shape described by Eq. 2.13 before it reaches z_0 , therefore a further adjustment to Eq. 2.13 is made using a displacement length d . Over tall roughness elements

$$\bar{u} = \frac{u_*}{k_a} \ln\left(\frac{z-d}{z_0}\right) \quad (2.14)$$

where d is typically about .75 element height. Further adjustments to Eq 2.14 are needed to adequately describe the mean profile in a non-neutral atmosphere (see Panofsky and Dutton, 1984). Eq 2.14 is applicable for z sufficiently $> d$ but it is not useful when $z < d$. In this study the flow below d in the forest is of interest.

2.2 In-canopy Flow

In a vegetative canopy, Cionco (1962) proposed a mean wind profile of the form

$$\bar{u} = \bar{u}_h e^{\alpha\left(\frac{z}{h} - 1\right)} \quad (2.15)$$

where h is canopy height and

$$\alpha = h\left(\frac{s}{2l_c^2}\right)^{1/3} \quad (2.16)$$

where

$$s = \frac{1}{2} C_d A \quad (2.17a)$$

and l_c is the local mixing length, C_d is the drag coefficient and A is the leaf area density in $\frac{m^2}{m^3}$. Later, Cionco (1985) replaces s in Eq 2.17a by

$$S = \frac{1}{2} \rho C_d A_z \quad (2.17b)$$

where ρ is the air density and a_z is the derivative of the leaf area density with respect to z . This approach by Cionco is important because it relates canopy drag to the impedance of flow.

As the development of canopy flow theory gained in sophistication and computational technology improved, the emphasis in modeling in-canopy flow shifted to the equation of motion and Reynolds stress closure. The governing equations for the instantaneous velocity and kinematic pressure are second-order, non-linear partial differential equations. and may be stated as:

$$\underbrace{\frac{\partial u_i}{\partial t}}_A + \underbrace{u_j \frac{\partial u_i}{\partial x_j}}_B = - \underbrace{\frac{\partial p}{\partial x_i}}_C + \underbrace{\delta_{i3} g \frac{\theta}{T}}_D + \underbrace{\nu \frac{\partial^2 u_i}{\partial x_j \partial x_j}}_E \quad (2.18)$$

and

$$\frac{\partial u_i}{\partial x_i} = 0 \quad (2.19)$$

where g is the acceleration of gravity, θ is potential temperature, and T is reference temperature. In Eq 2.18, A represents the local rate of change of momentum, B is the advection of momentum, C is the pressure force, D represents the bouyant force and E is the viscous force. If this equation is averaged over a horizontal plane large

enough to eliminate horizontal variations due to canopy inhomogeneity and the quantities are expanded into their mean and fluctuating parts, Eq 2.19 becomes (Wilson and Shaw, 1977):

$$\frac{\partial \bar{u}_i}{\partial t} + \bar{u}_j \frac{\partial \bar{u}_i}{\partial x_j} + \frac{\partial \overline{u'_i u'_j}}{\partial x_j} = - \frac{\partial \bar{p}}{\partial x_i} - \frac{\partial \bar{p}'}{\partial x_i} + g \frac{\bar{\theta}}{T} \delta_{i3} + \nu \frac{\partial^2 \bar{u}_i}{\partial x_j \partial x_j} + \nu \frac{\partial^2 \overline{u'_i}}{\partial x_j \partial x_j} \quad (2.20)$$

In Eq 2.20, terms 2 and 5 on the r.h.s. represent the canopy element drag force.

For the purpose of closure, the Reynolds stress equation for canopy flow, Eq 2.21, may be obtained as

$$\begin{aligned} & \frac{\partial \overline{u'_i u'_k}}{\partial t} + \bar{u}_j \frac{\partial \overline{u'_i u'_k}}{\partial x_j} + \overline{u'_k u'_j} \frac{\partial \bar{u}_i}{\partial x_j} + \overline{u'_i u'_j} \frac{\partial \bar{u}_k}{\partial x_j} + \frac{\partial \overline{u'_i u'_k u'_j}}{\partial x_j} \\ &= - \left(\frac{\partial \overline{u'_k p'}}{\partial x_i} + \frac{\partial \overline{u'_i p'}}{\partial x_k} \right) + (\bar{u}_k \frac{\partial \bar{p}'}{\partial x_i} + \bar{u}_i \frac{\partial \bar{p}'}{\partial x_k}) + \overline{p' \left(\frac{\partial u'_k}{\partial x_i} + \frac{\partial u'_i}{\partial x_k} \right)} \\ &+ \frac{g}{T} (\overline{\theta' u'_i} \delta_{k3} + \overline{\theta' u'_k} \delta_{i3}) + \nu \frac{\partial^2 \overline{u'_i u'_k}}{\partial x_j \partial x_j} - 2\nu \frac{\partial \bar{u}'_i}{\partial x_j} \frac{\partial \bar{u}'_k}{\partial x_j} \end{aligned} \quad (2.21)$$

Distinguishing this as a canopy equation are the terms inside the second set of parentheses on the r.h.s. Notice in Eq 2.21 the emergence of a triple correlation term as the last term on the l.h.s. of the equation. The pressure-velocity correlations on the r.h.s. of Eq 2.21 introduce more closure difficulty.

The second order closure scheme of Wilson and Shaw (1977) for one-dimensional canopy flow assumed that the vegetative drag was due to pressure forces and parameterized the mean fluctuating pressure as

$$- \frac{\partial \bar{p}'}{\partial x_i} = C_D A |\bar{u}_i| \bar{u}_i \quad (2.22)$$

The equations were closed by specifying the triple covariance in terms of second-order Reynolds stresses. Viscous dissipation (last terms on the rhs of Eq. 2.21) is modeled using an expression similar in form to Eq. 2.4.

The models examined to this point treat the canopy elements themselves as static sinks of momentum. In reality, canopy elements move or wave in the wind. The plants store mean kinetic energy (MKE) as strain potential and release it half a waving cycle later as turbulent kinetic energy (TKE) (Raupach and Thom, 1981). Finnigan (1979) quantifies this waving in a wheat canopy as

$$\xi(x) = \xi_0(x)e^{2\pi i(\frac{x}{\lambda_p} - ft)} \quad (2.23)$$

where $\xi(x)$ is the x direction displacement of the stalk from a mean position, $\xi_0(x)$ is the vibration amplitude, λ_p is the wavelength and f is the frequency of stalk vibration. This is the equation of a simple harmonic travelling wave. The significance of this is that it approximates the actual movement of an individual canopy element. The periodic nature of this function explains the apparent coherent, wavelike motion, termed honami, which is often observed in grain crops. A strong gust of wind with frequency $\frac{\bar{u}}{\lambda_{max}}$ exerts a discrete force imparting MKE of the air to a group of spatially congregated stalks and bending them. As the gust abates the stalks wave in unison at their natural frequency (n_f) until the stored strain energy is dissipated in the air as TKE. As the gust translates along the surface it forces different stalks at different times, therefore introducing a waving motion and giving the visual impression of progressive waves rolling over the surface of the grain. It is difficult to extrapolate this periodic, semi-deterministic motion to non-homogeneous canopies. In a forest, all plants have a n_f but they are all different depending on the distribution of mass and the elastic properties of the plant.

Finnigan (1985) presents the turbulent flux equation for a scalar quantity, c , which is time and volume averaged at second-order inside a flexible plant canopy. This relationship is presented here to gain physical insight and emphasize the complex nature of the flow. The concentration flux ($\overline{u'c'}$) is governed by the following

$$\underbrace{\{\overline{u_j}\} \frac{\partial}{\partial x_j} \overline{\{u_i'c'\}}}_{\text{A}} + \underbrace{\frac{\partial}{\partial x_j} \overline{F} da_j}_{\text{B}} + \underbrace{\overline{\{u_i'u_j'\}} \frac{\partial}{\partial x_j} \{c\}}_{\text{C}} + \underbrace{\overline{P} d_b}_{\text{D}} \quad (2.23a)$$

$$+ \underbrace{\overline{\{u_j'c'\}} \frac{\partial}{\partial x_j} \{\overline{u_i}\}}_{\text{E}} + \underbrace{\overline{P} d_c}_{\text{F}} + \underbrace{\frac{\partial}{\partial x_j} \overline{\{u_i'u_j'c'\}}}_{\text{G}} - \underbrace{\overline{\{p' \frac{\partial c'}{\partial x_i}\}}}_{\text{H}} + \underbrace{\frac{\partial}{\partial x_j} \overline{\{p'c'\}}}_{\text{I}}$$

$$= \frac{1}{V} \sum_I \left(\underbrace{\iint_{S_i} \overline{c'(p'n_i - v \frac{\partial u_i'}{\partial n})} ds}_{\text{J}} - \underbrace{\iint_{S_i} \overline{k_c v_i' \frac{\partial c'}{\partial n}} ds}_{\text{K}} - \underbrace{(k_c + v) \left\{ \frac{\partial u_i'}{\partial x_j} \frac{\partial c'}{\partial x_j} \right\}}_{\text{L}} \right)$$

$$+ \underbrace{\{(k_c + v) \frac{\partial}{\partial x_j} \overline{\{u_i'\}} \frac{\partial}{\partial x_j} \{c'\}\}}_{\text{M}} + \underbrace{\{v\{c'\} \frac{\partial^2}{\partial x_j^2} \{u_i'\}\}}_{\text{N}} + \underbrace{k_c \{u_i'\} \frac{\partial^2}{\partial x_j^2} \{c'\}}_{\text{N}} + \underbrace{\frac{g}{\theta} \overline{\{T_V'c'\}}}_{\text{O}}$$

where

$$\bar{F}da_j = \{ \{ \bar{u}_j \} \{ \overline{u_i' u_j'} \} \} - \{ \bar{u}_j \} \{ u_i' c' \} + \{ \bar{u}_j'' \{ \overline{u_i' c'} \}'' \} + \text{mixed} \{ \} \text{terms} \quad (2.23b)$$

$$\bar{P}d_B = \{ \{ \overline{u_i' u_j'} \} \frac{\partial}{\partial x_j} \{ \bar{c} \} \} - \{ \overline{u_i' u_j'} \} \frac{\partial}{\partial x_j} \{ \bar{c} \} + \{ (\overline{u_i' u_j'})'' \frac{\partial}{\partial x_j} c'' \} + \dots \quad (2.23c)$$

$$P d_c = \{ \{ \overline{u_j' c'} \} \frac{\partial}{\partial x_j} \{ \bar{u}_i \} \} - \{ \overline{u_j' c'} \} \frac{\partial}{\partial x_j} \{ \bar{u}_i \} + \{ (\overline{u_j' c'})'' \frac{\partial}{\partial x_j} \bar{u}_i'' \} + \dots \quad (2.23d)$$

$$T_V = T(1 + .61q) \quad (2.23e)$$

In this equation k_c is the molecular diffusivity and q is specific humidity. In the surface integral terms, v_i is the velocity of the leaf, n is the unit normal vector from the leaf surface, s_i represents the surface of the m leaves in the volume, V , being spatially averaged. In Eq 2.23, the overbar represents a time average and the single prime (') represents a fluctuation around the time average. Brackets ({ }) represent a spatial average and the double primes (") are the fluctuations about that average.

It is instructive to examine equation 2.23 term by term following Finnigan (1985) and to compare Eq. 2.23 to Eq. 2.21. Term A is advection by the mean wind. B represents the contribution to advection by the dispersive terms which arise from the volume averaging of the advection term in the time average of scalar fluxes. It is important to note that in a non-homogeneous canopy, such as the forest edge, a representative volume is difficult to define and the dispersive terms become more important. C and E represent turbulent production while D and F are again dispersive terms arising from the volume averaging of the production terms. G is the turbulent transport or 'divergence' (Businger, 1982) and H and I are volume averaged pressure terms.

Terms J and K on the rhs of Eq 2.23 are the manifestations of the forest elements in this formulation. The terms encompass wake production of turbulence as p' minus viscous dissipation and the influence of the moving plant part on the scalar gradient. These terms couple moving plant elements to the turbulent air flow. L accounts for molecular dissipation. M considers variation in the molecular dissipation of the fluid and is probably small because ν may be considered constant. N is molecular diffusion and O is bouyant production.

Other recent work on canopy flow modeling includes Li (1982) and Bache (1986) among others. Though the physical understanding of canopy flows is advancing, measurements of in-canopy flows do not always conform to results anticipated by physics as they are currently understood. The third-order model of Meyers and Paw U (1986) does a reasonable job reproducing measured in-canopy profiles of mean wind but does less well predicting mean TKE profiles. Further, the question arises whether mean statistics are appropriate or useful descriptors of in-canopy flows.

2.3 Experimental Research in In-canopy Flows

The development of experimental research and the resulting descriptions of in-canopy flows paralleled the theoretical work, though recent advances in measurement technique and data collection and storage have accelerated the work. Allen (1968) measured turbulence in a large forest stand with cup anemometers and heated thermocouples. Mean velocity profiles are presented which indicate a secondary maxima of horizontal velocity in the trunk space, also a shift to a shorter integral scale inside the canopy compared to those above the canopy indicates that TKE is shifted to higher frequencies inside the canopy. Shaw et al. (1974) con-

ducted extensive turbulence measurements inside a corn canopy with a hot-film anemometer. These data indicate a decrease in both momentum and heat flux with height in the canopy. Velocity component-spectra are presented which indicate a shift in the equilibrium sub-range to higher frequencies inside the canopy. Seginer et al. (1976) presents turbulent statistics for a model canopy. These data indicates a decrease in turbulent intensity, TI , of all components with height above the canopy but marked differences in TI below the canopy exist between u, v and w . TI appears relatively constant with height below the canopy while TI_w increases and TI_v decreases. Also, Seginer indicates a strong maximum in shear stress at the top of the canopy. Many other studies of in-canopy turbulence have been conducted in model canopies with some of the most comprehensive and modern being Coppin et al. (1986), Legg et al. (1986) and Raupach et al. (1986).

Flow structure in a forest canopy can be classified using vertical variation in length scales and turbulence statistics. Immediately above the canopy is the roughness sublayer where the influence of the canopy on the flow is apparent. Here turbulent production is offset by dissipation and turbulent transport. Above this level is the equilibrium sublayer also known as the constant flux layer. Garratt (1980) defines a depth, z_* , from the surface as the layer in which the flow is affected by wakes from surface roughness elements. In this treatment z_* is typically between $3h$ and $8h$ and is dependent on tree spacing. Finnigan (1985) presents wind tunnel data which suggests that turbulent transport of TKE due to the influence of the canopy on the flow is negligible above $2h$. Immediately under the top of the canopy turbulent production and turbulent transport are important. Below this the main source of TKE is turbulent transport.

Parallel to the development of understanding canopy flow in the mean sense has been the awareness that in all boundary layer flows a disproportionate amount of momentum is transferred in short duration, low frequency, high energy events or gusts. The study of these events or coherent structures in laboratory flows is relatively recent (see Chen and Blackwelder (1978) for references and history from the standpoint of engineering fluid mechanics). The spectra of atmospheric turbulence has strong low frequency components with length scales proportional to z_i . These low frequency high energy events can be studied individually. Models are now being constructed which use filter functions to eliminate the high frequency turbulent components and focus on the lower frequency, energetic eddies. This is called large eddy simulation (Moeng, 1984).

The point to be made here is that a boundary layer flow always involves a vertical velocity gradient ($\frac{\partial u}{\partial z} > 0$) and typically in the atmosphere involves non-zero heat and humidity gradients. The surface is the momentum sink and can be a heat sink or source depending on the radiation balance. The surface velocity is said to be zero as required by the 'no-slip' surface boundary condition. Mean velocity then increases with height upward from the surface according to Eq 2.14 in the simplest case. Following this reasoning, it is apparent that an increase in horizontal velocity u at a given height above its mean value at that height should be accompanied by a down draft ($w' < 0$) which will transport higher velocity fluid from above. The 'eddy-correlation' term for momentum flux or shear stress is

$$\tau = \overline{\rho w' u'} \quad (2.24)$$

and a similar expression for thermal energy is

$$H = \rho c_p \overline{w' T'} \quad (2.25)$$

where the units of Eq. 2.24 are $\text{kg m}^{-1}\text{s}^{-2}$ (momentum flux) and those of Eq. 2.25 are Wm^{-2} (energy flux).

Though Eqs 2.24 and 2.25 are mean expressions, the eddy correlation terms can be used to describe instantaneous events. A strong downdraft ($-w$) may be expected to be associated with cooling ($-T'$) in the temperature series. This is because the downdraft will transport cooler fluid from above. The magnitude of the fluctuation in temperature will be dependent on \bar{w} and the thermal structure of the PBL. Large $-T'$ may be an indication of a large transporting structure or eddy. If the atmosphere is neutral ($\frac{d\theta}{dz} = 0$), $\frac{dT}{dz}$ may be too small to use this relationship.

Shaw et al., (1979) discussed the frequency of strong gusts of wind inside a canopy. If one Hz samples are distributed by velocity magnitude they are reasonably well described by an extreme value distribution. The work is important because the role of gusting is recognized and discussed. Many organisms require a wind above a threshold value to accomplish dispersion. In some cases, dispersion would not be accomplished at the mean wind speed and requires high velocity events. Thompson (1979) noted a saw-tooth structure in the time series of temperature over a forest. The explanation offered is that temperature dropped sharply as the front or down draft portion of a large vortex moved past then slowly rose toward equilibrium with ambient mean until another down draft or front passed. This is important to this study because it offers a specific shape or occurrence to search for in a time series in an effort to isolate and study these low frequency events.

One technique to detect the frequency of the anomalously large events is known as hole analysis (Shaw, et al (1983) Shaw (1985)). In this technique, the stress term, $u'w'$ is divided into four quadrants according to the sign of the two components

individually. It is expected that when $w' < 0$ (down) $u > \bar{u}$ and when $w' > 0$ $u < \bar{u}$. Shaw has shown that $u'w'$ are dominant in in-canopy flows. This technique is of great utility in this thesis and will be discussed in detail later. Another method used to identify and subsequently analyze high energy low frequency flow structure is the variable interval time average (VITA, Chen and Blackwelder (1978) Schols (1984)). This technique searches for abrupt or anomalous change in a given series. As has been explained, such changes may indicate passage of fluid moved rapidly over a large distance. Once an individual event is identified, its propagation in space and time, as well as its inherent properties, may be studied. This concept is used in this study and will be discussed in greater detail later.

Modern articles discussing flux profiles and scalar gradients in and above a forest canopy include Denmead et al., (1985), Lindroth (1984), Verma et al., (1985) and others. Dolman (1986) provides estimates of z_0 and d in a foliated and an unfoliated canopy. The wind profiles given by Dolman for foliated and unfoliated canopies are the only other profiles of this type available for comparison to data presented in this thesis. Generally the foliated velocity profiles show higher $\frac{d\bar{u}}{dz}$ than the unfoliated profiles above the canopy. These profiles do not extend down into the canopy.

Notable recent work on the flow field in monocultures and other homogeneous canopies has been conducted by Finnigan (1979) as referenced previously, Baldocchi et al., (1983) and Hayashi (1986). Hicks (1981) discusses the possibility for misuse of turbulence statistics and the use of Ri as opposed to z/L describing surface layer stability. Grant (1984) studied the air flow in and around individual spruce shoots demonstrating that C_d is a function of velocity. At low velocity the flow moved between the individual needles, but at a higher velocity, dependent on needle den-

sity, the flow moved around the shoot with needle density mediating the 'roughness' of the shoot surface.

Some recent work has focused directly on turbulent statistics in and near forest canopies and canopy edges. Anderson et al., (1986) offer an extensive treatment of the spectral characteristics of flow over a foliated forest canopy. Spectra of temperature, humidity and CO_2 are presented as are co-spectra of these three scalar quantities individually matched with vertical component (w). The u spectra presented by Anderson show λ_{max} at a normalized frequency .035 which is at slightly lower frequency than that reported over flat terrain. This shift may be due to the complexity of the terrain surrounding the experimental site. Baldocchi and Hutchison (1986) measured turbulent flow in an almond orchard and reported extensive turbulent statistics. Comparisons with their work must be made with caution due to the relatively low height and density of the canopy, and the fact that the trees are regularly spaced at the nodes of the grid. Gash (1986) reported measurements downwind of a forest edge. Although he deals primarily in mean statistics, this work demonstrates that the influence of an extensive forest stand on the down wind surface flow pattern may be detected for a substantial distance $O(100 \text{ m.})$.

A segment of the literature which requires further mention here is the development of spectral theory in the PBL and the subsequent development of spectral models. Kaimal et al., (1976) and Kaimal (1978) established the existence of controlling length scales in the PBL, the relative shape of the component spectra and the role of stability, etc. as discussed earlier. Kaimal demonstrated that many of the empirical results measured in the PBL were anticipated by theoretical fluid dynamics. Largely based on the work of Kaimal a body of literature has developed attempting to simulate and then predict atmospheric spectra under specified cir-

cumstances. Hojstrup (1982) modeled surface layer spectra as the sum of a mixed layer, stability dependent part and a surface layer part which is independent of stability. Claussen (1985) models ASL spectra using an energy cascade model. Claussen uses the model to predict similarity relationships relating momentum and heat flux.

Two unique studies of importance to this thesis have arisen out of this spectral modeling literature. Kristensen et al., (1979) offer a theoretical development of coherence among velocity components and compare the theoretically derived results with atmospheric data. Coherence decreases with distance in turbulent flows but the exact expression of this dependence is complex in isotropic turbulence and difficult to obtain in the atmosphere. Still, Kristensen obtains reasonable agreement between predicted lateral coherences and those obtained from the atmospheric measurement. These ideas are important when trying to relate multi-point time series in a two-dimensional instrument array. Hojstrup (1981) presents a scheme to model the adjustment of turbulent spectra down wind of a surface roughness change. The model consists of three basic parts. The first is a model of turbulence spectra over a homogeneous surface, the second describes the growth of a boundary layer across the roughness change and finally the expression of the adjustment of an eddy to the change.

2.4 ASL Flow in Complex Terrain

The next area which requires discussion here is the effect of complex terrain on flow in the surface layer. There is a multitude of literature discussing this topic.

Mason et al., (1979) and Mason (1986) observe an increase in mean flow over the top of a hill. This increase in velocity tends to distort eddies with length scale longer than the hill while the smaller scales are strongly disrupted. Smedman et al., (1984) also conducted turbulence measurements on a low hill while Arya et al., (1986) conducted wind tunnel experiments using simulated hills of various slope. It was found that a hill of 26.5° slope showed a definite recirculation in the lee of the hill, while a hill of 17.5° slope did not. Other researchers have developed physically based models to describe flow over uneven terrain (Taylor et al., (1983), Walmsley et al., (1986) and Jones et al., (1986)).

Since the experiment site is in a region of complex terrain of low to moderate base to peak height it is important to be able to anticipate (at least speculate) on the effect of terrain on the flow. The author selected three key studies to elucidate the topic. Hunt et al., (1984) gives a theoretical discussion of flow 'over one or two hills'. The flow over a hill is divided into three regions, the inner region where the flow follows the contours of the hill, outer region where flow velocity over a hill is equal to flow velocity at the same elevation over the surface upwind and a middle region which is transitional between the inner and outer regions. Hunt states that in the lee or wake flow 'behind' the hill, $\frac{d\bar{u}}{dz}$ may have a maximum value well above the surface. This elevated shear layer controls the generation of turbulence and the effect may be propagated downstream. Only scales smaller than the scale of the inner layer are determined locally, while longer scales are determined by advection or distortion in the middle layer. In the mean sense, the hill acts as an obstruction to flow. As the flow is locally constricted, velocity increases near the constriction and pressure drops according to Bernoulli's theorem. The change in pressure then propagates through the fluid as an acoustic wave so the effects of the obstruction above the surface show a phase lag proportional to the speed of sound.

Kaimal et al., (1982) and Panofsky et al., (1982) have conducted studies on the effect of complex terrain on ASL spectra. Downwind of surface roughness increases, the spectra is effected only in the inner region. Considering spectra of u' , high frequencies adjust quickly while low frequencies remain unaffected. Hilltop spectra show rapid adjustment in high frequency spectra but also show a depletion in low frequency spectral densities, possibly due to large eddy shearing in the high velocity region at the hilltop. Spectra of vertical velocity appear to always be in local equilibrium in complex terrain because of the small amount of low frequency energy in these spectra. Kaimal does report a shift in λ_{\max} of the w spectra to lower frequency over uneven terrain, though the cause of the shift is not well understood.

2.5 Scaling

The final body of literature which needs to be examined is that of scaling atmospheric flows. Scaling is necessary to generalize and compare results between sites and circumstances. The discussion here will be divided between ASL scaling and scaling in plant canopies, though it is difficult to decouple the two. The ASL can be defined as the layer in which wind shear is dominant (Caughey, 1982). In this layer, z , τ (Eq. 2.24), H (Eq. 2.25) and buoyant forces ($\frac{g}{\theta}$) are parameters which control the flow field. The flow in this layer typically scales with u_* (Eq. 1.5). Above the ASL is the free convection layer where τ is not important. Above the FCL is the mixed layer where neither τ nor z are important and z_i is the dominant length scale. In this layer scaling by w_* where:

$$w_* = \left(\frac{gH z_i}{c_p \rho T_0} \right)^{\frac{1}{3}} \quad (2.26)$$

is used. Scaling by w_* is appropriate at a height where, wind speed and roughness do not contribute to turbulence statistics or the velocity profile (Panofsky and Dutton, 1984). Finally, the highest layer in the PBL is the entrainment interfacial layer which is influenced by entrainment from the stable atmosphere above and by the characteristics of the capping inversion. Important discussions of PBL scaling are Panofsky (1978) and Holtslag et al., (1986). Hicks (1985) discusses the variance of turbulence statistics with height in the PBL and scaling above the ASL.

Traditional ASL scaling by u_* may not be appropriate in-canopy because of the failure of the logarithmic profile equations (Eqs 2.9-2.14). u_* is not a characteristic of the velocity profile in a forest canopy, instead it becomes a local quantity determined primarily by local canopy drag and density considerations. The complexity of the experimental site used in this study further complicates scaling, with the edge and the uneven terrain influencing the flow. Also, local C_d is a function of velocity and in-canopy length scales may increase by steps at certain threshold velocities (Grant, 1984) because of step increases in canopy element drag coefficients. This implies that in-canopy scaling schemes may be velocity dependent.

In this study, scaling of mean velocity will be provided by a reference anemometer stationed above a canopy. Scaling by \bar{u} at the reference (\bar{u}_{ref}) will be tested. One problem with this approach is that the reference anemometer is at a fixed height in all of these runs. Therefore, during unfoliated runs the anemometer is relatively higher because d is lower in the canopy than it is when the canopy is foliated. The displacement of d is accompanied by a shift in the roughness sub-layer and the nature of the associated turbulence at the reference anemometer. One way to alleviate or quantify this effect may be to compare reference velocities measured above the canopy with velocities measured above low vegetation outside the forest.

These measurements will also be influenced by seasonal changes in surface roughness as well as being subjected to different thermal considerations. Finally, measurements outside the edge would be strongly influenced by the edge during forest fetch flows since the anemometers are within $4H$ of the edge.

Scaling of spectra in the ASL is typically accomplished by plotting a normalized spectral density versus a dimensionless frequency, f , where

$$f = \frac{nz}{u} \quad (2.27)$$

n is frequency (cycles s^{-1}). The difficulty with this equation is the explicit scaling with z . Near a rough surface, $z-d$ may be used, but inside a canopy, $z-d$ maybe < 0 making this quantity meaningless. Height (z) is a length which makes intuitive sense in this expression because the surface truncates or disrupts vortical motion. One scheme is to substitute a length, λ_c which is a characteristic in-canopy scale (Silversides, 1974) dictated by the size of canopy elements. This is not suitable in a situation where the canopy is vertically non-homogenous, as is a deciduous forest, and horizontally non-homogenous, as is the case near a forest edge. Another technique under consideration is the use of a length scale L where

$$L_s = \left\{ \begin{array}{ll} |z-d| & \text{if } z < |z-d| \\ z & \text{if } z > |z-d| \end{array} \right\} \quad (2.28)$$

thus in-canopy spectra would be scaled with $|z-d|$ everywhere except in the lowest part of the trunk space where z , the height from the forest floor would be used. This approach assumes that vortices below d will be truncated by the dense part of the canopy or the ground, whichever is closer. A problem with this approach is that although d may be defined as a plane, it is better described as a layer in a foliated

forest canopy and this makes it difficult to scale spectra measured close to d . As $L \rightarrow 0$, $f \rightarrow 0$ which is not reasonable. One easy solution is to not allow $|z - d|$ to be below some threshold so that

$$|z - d| = \begin{cases} |z - d| & \text{if } |z - d| > T_h \\ T_h & \text{if } |z - d| < T_h \end{cases} \quad (2.29)$$

where T_h is a threshold length.

Other factors which must be considered in categorizing the flows in this study are stability as discussed previously and wind direction. Turbulence statistics will be effected by mean wind direction because of differences in fetch at the site. Runs are grouped into forest and edge fetch. Mean direction of edge fetch runs are compared to turbulent intensities in the forest to determine if varying the path length of the flow in the canopy will effect turbulent intensity.

Chapter III

Instrumentation

3.1 Introduction

The primary sensor system used in this study is the combination of a triple hot-film anemometer with an electronic direction sensor known as a TFWOES (Miller, et al., (1987)). This system was used in conjunction with a high frequency temperature sensing system. Also in the instrument array were three-dimensional propeller anemometers, a sonic vertical anemometer and a pyranometer. This chapter will focus on the instruments themselves and the general operational theory relating to the instrumentation. Included in this chapter will be a description of the analog to digital conversion system used ,along with a description of the field computer. Considerations of suitability to in-canopy flow research will be discussed here but the experimental design, such as array spacing and sampling frequency, used in this study is discussed in Chapter 4.

3.2 Hot-Film Anemometry

The general discussion of thermal anemometry presented here follows Lomas (1986). The primary velocity sensor in this study is a constant temperature hot-film anemometer. A heated electrical resistance element immersed in a fluid will lose heat by forced convection in proportion to the speed of the fluid flowing past the element. This heat loss is typically accompanied by a change in the resistance of the exposed element because resistance is a function of temperature in most materials. Therefore, by monitoring the resistance of the element, it is possible to infer a change in temperature which is proportional to the heat flux due to forced convection.

In a constant temperature anemometer (CTA) the exposed element is one leg of a Wheatstone bridge. The sensor leg of the bridge is opposed by a potentiometer so that a change in resistance at the sensing element is balanced by a change at the potentiometer. In the CTA configuration, a feedback amplifier is in parallel with the potentiometer. When the potentiometer indicates a bridge imbalance, the circuit compensates the current to the sensor element to keep the element at a constant temperature. It is the changing current to the bridge which is interpreted as the fluctuating fluid velocity at the sensing element. It is important to note that the circuit as described here cannot distinguish between ambient temperature and velocity fluctuations.

The sensitivity of a given system is indicated by the change in voltage (∂E) due to the change in velocity as

$$s_{\text{vel}} = \frac{\partial E}{\partial U} \quad (3.1a)$$

and in temperature as

$$s_{\text{temp}} = \frac{\partial E}{\partial T} \quad (3.1b)$$

resulting in

$$dE = \frac{\partial E}{\partial U} dU + \frac{\partial E}{\partial T} dT \quad (3.2a)$$

or

$$dE = s_{\text{vel}} dU + s_{\text{temp}} dT \quad (3.2b)$$

so dE is explicitly given as the sum of the velocity and temperature changes multiplied by system specific sensitivity coefficients. Typically, s_{temp} is made negligible, either through design or operating procedures.

If the sensing element is heated far above ambient, then the relative effect of ambient temperature fluctuations become negligible. Since sensor resistance, R_s , is proportional to temperature, the element to ambient temperature ratio is expressed as

$$a_H = \frac{R_s}{R_f} \quad (3.3)$$

where R_f is element resistance at the ambient fluid temperature. Eq 3.3 is known as the heat ratio.

Each hot-film consists of a thin metallic coating around a silica cylinder. So the problem effectively becomes one of heat transfer from a cylinder. Fritschen and Gay (1979) explain that heat transfer (H) from a heated sensing element is related to the Nusselt number (Nu)

$$Nu = \frac{H}{h(T_s - T_f)} \quad (3.4)$$

where h is the thermal conductivity of the fluid. At low velocities, Nu is a function of the Reynolds number (Re), relating kinetic to viscous forces

$$Re = \frac{Ud}{\nu} \quad (3.5)$$

The Prandtl number (Pr), relates the viscous dissipation and thermal diffusivity

$$Pr = \frac{\nu}{k_H} \quad (3.6)$$

and the Grashof number (Gr), the free and forced convection

$$Gr = \frac{g\beta(T_s - T_f)d^3_L}{\nu^2} \quad (3.7)$$

where β is the volume coefficient of thermal expansion

$$\beta = -\frac{1}{\rho} \left(\frac{\partial \rho}{\partial T} \right)_p \quad (3.8)$$

In Eqs 3.5 and 3.7, d is a characteristic length which in this discussion will be the diameter of the cylinder.

Lomas (1986) states that for a hot-wire sensor

$$Re_{min} = 1.85Gr^{.39} \left(\frac{T_s}{T_f} \right)^{.76} \quad (3.9)$$

where Re_{min} is the minimum Reynolds number at which these probes are useful. Though it is not valid from a quantitative standpoint to apply Eq 3.9 in this study due to the differences in sensor type, the relationship demonstrates certain points. Re_{min} may be thought of as indicating a minimum valid velocity if v and d are treated as constants. In Eq 3.7 it can be seen that as the overheat ratio increases, Gr increases. This indicates that free convection or bouyancy effects become more important. As Eq 3.9 indicates due to both the Grashof number and overheat ratio terms, increasing the overheat ratio causes an increase in minimum velocity which can be measured with the CTA. At very low velocities, the Grashof number becomes large and free convection created by the sensing element will dominate the local flow field. Conventional hot-wires have a lower velocity limit of .1 to .2 ms^{-1} (Lomas, 1986), hot films typically have a higher minimum velocity due to an increase in effective d . Where very low velocity flows are encountered, the CTA circuit can be coupled with a high frequency temperature sensor which allows differencing or compensation of temperature effects. The CTA system used in this study is not hardware temperature compensated. Calibration limitations control the minimum discernable velocity.

To understand the physics of the sensor itself, it is necessary to examine the heat balance equation of a sensor. First, the equation will be assembled for a differential length (dx) of a hot-wire of length l and cross-sectional area A . Following Lomas (1986), the heat transfer rate into the left end of dx is

$$-k_s A \frac{\partial T_s}{\partial x} dx \quad (3.10)$$

where k_s is the thermal conductivity of the sensor. Term 3.10 is negated by an equivalent term at the right end of dx leaving the change of 3.10 across dx

$$A \frac{\partial}{\partial x} (k_s \frac{\partial T_s}{\partial x}) dx \quad (3.11)$$

The heat generated in the sensor is

$$\frac{I^2 \Omega}{A} dx \quad (3.12)$$

where I is the current and Ω is the resistivity of the sensor material. The heat storage rate is given by

$$\rho_s c_s A \frac{\partial T_s}{\partial t} dx \quad (3.13)$$

where ρ_s and c_s are the density and specific heat of sensor material respectively. Notice that this term contains a time derivative. This is the term that controls sensor frequency response.

The term for convective heat transfer is

$$\pi d h_c (T_s - T_f) dx \quad (3.14)$$

where h is the coefficient of convective heat transfer. This is the loss term which needs to be dominant in an effective CTA sensor. The final term is the radiative term

$$\pi d \sigma \epsilon (T_s^4 - T_{sur}^4) dx \quad (3.15)$$

where σ is the Stefan-Boltzmann constant, ϵ is the emissivity of the sensor and T_{sur} is the temperature of the surroundings.

Assembling these terms, the heat balance equation is obtained

$$A \frac{\partial}{\partial x} (k_s \frac{\partial T_s}{\partial x}) + \frac{l^2 \Omega}{A} - \rho_s c_s A \frac{\partial T_s}{\partial t} - \quad (3.16)$$

$$\pi d h (T_s - T_f) - \pi d \sigma \epsilon (T_s^4 - T_{sur}^4) = 0$$

Before adjusting Eq 3.16 for hot-film sensors, it is possible to eliminate the radiative transfer term as being negligible (Lomas, 1986) for most sensor types.

Hot-film sensors are usually created by sputtering a metal heated above melting onto an insulator of low k and high Ω . The metal is often a nickel alloy and the substrate is usually glass. A very thin film is deposited, but the overall sensor (film and substrate) is larger and more rugged than a typical hot-wire.

Returning to Eq 3.16, considering a film, all the terms are affected through the system constants A and d . In term 3.11, A remains a circular cross-section but it is the sum of cross-sections of different thermal properties. During a dynamic response, the substrate response will lag the film response. Though there is a lagged heating effect with depth in hot-wires, it becomes more important in films because of the low k value of the substrate and larger d . Term 3.11 expands into

$$A_s \frac{\partial}{\partial x} (k_s \frac{\partial T_s}{\partial x}) + A_{sb} \frac{\partial}{\partial x} (k_{sb} \frac{\partial T_{sb}}{\partial x}) \quad (3.17)$$

distinguishing between conduction in the film and conduction in the substrate. Film substrates are intentionally chosen for low values of k to prevent significant heat

loss to the probe mounts ('end effects'). When considering a hot-wire sensor, the aspect ratio

$$a_R = \frac{L}{d} \quad (3.18)$$

where L is the length of the wire, is used to estimate heat loss to the mounts. As $a_R \rightarrow \infty$ these losses decrease. In the case of a hot-film, a_R is smaller than for a hot-wire due to larger d . To prevent large amounts of heat from being conducted to the probe mounts, the film itself only covers half of the substrate cylinder, with inlaid leads extending to the probe mounts. Thus, end effects are reduced due to the insulating properties of the substrate.

In term 3.12, A is the cross-section of a ring because heat is only generated in the metallic film. Term 3.13 must be decomposed into

$$\text{Heat storage rate} = (\rho_s c_s A_s \frac{\partial T_s}{\partial t} + \rho_{sb} c_{sb} A_{sb} \frac{\partial T_{sb}}{\partial t}) dx \quad (3.19)$$

where A_s is now the cross-section of a ring representing the film and A_{sb} is the circular cross-section of the substrate. Terms 3.14 and 3.15 both represent surface effects so the difference between the film and the wire is in the $(\pi d)dx$ factor which represents surface area and increases with increasing d . The radiative term is again considered negligible. Thus, the conversion of the heat balance equation from that of a heated wire to that of a heated film is accomplished by defining two cross-sectional areas, adjusting d and adding terms for substrate heat conduction and substrate heat storage.

To understand the frequency response of the films it is necessary to return to Fritschen and Gay (1979) for a discussion of time constants. For this discussion a measured scalar quantity Q will be considered. If the sensor is at equilibrium at $Q = Q_1$ and is moved to condition Q_2 , the sensor will asymptotically approach Q_2 . After this change, $\frac{dQ}{dt}$ is proportional to $Q_1 - Q_2$ so

$$\frac{dQ_1}{dt} = -\frac{1}{\tau} (Q_1 - Q_2) \quad (3.20)$$

where τ is a coefficient of proportionality known as the time constant of the sensor. Considering a step change in Q at the sensor

$$\int \frac{1}{(Q_1 - Q_2)} dQ_1 = \int \frac{-1}{\tau} dt \quad (3.21)$$

which integrates to

$$\ln(Q_1 - Q_2) + C = \frac{-t}{\tau} \quad (3.22)$$

solving for ΔQ

$$Q_1 - Q_2 = Ce^{-t/\tau} \quad (3.23)$$

if $t=0$ then Q_1 equals initial temperature Q_0 (note that C is a different constant in Eq 3.23 than in 3.22) and we have

$$Q_0 - Q_2 = C \quad (3.25a)$$

and

$$Q_1 - Q_2 = (Q_0 - Q_2)e^{-t/\tau} \quad (3.25b)$$

when $t = \tau$

$$\frac{Q_1 - Q_2}{Q_0 - Q_2} = \frac{1}{e} = .368 \quad (3.26)$$

Since from a theoretical standpoint

$$\lim_{t \rightarrow \infty} Q_1 = Q_2 \quad (3.27)$$

the time constant is defined as the time it takes .632 of the adjustment in Q to the new steady state to occur. Of course, turbulent flows do not usually vary by steps but are by definition continuously fluctuating. With this in mind, it is instructive to examine the case where Q varies as a sine wave. In this case Eq 3.20 is manipulated so the change in Q_1 follows a sine wave of amplitude Q_α and angular frequency ω ,

$$\frac{dQ_1}{dt} + \frac{Q_1}{\tau} = \left(\frac{Q_\alpha}{\tau} \right) \sin \omega t \quad (3.28)$$

3.28 has the analytic solution

$$Q_1 = C_1 e^{-t/\tau} + Q_\alpha [1 + (\omega\tau)^2]^{-1/2} \sin(\omega t - \arctan(\omega\tau)) \quad (3.29)$$

evaluating at t_0 yields

$$Q_1 = Q_\alpha \omega \tau (1 + (\omega\tau)^2)^{-1/2} e^{-t/\tau} + Q_\alpha (1 + (\omega\tau)^2)^{-1/2} \sin(\omega t - \arctan(\omega\tau)) \quad (3.30)$$

As $t \rightarrow \infty$ the first term on the rhs of Eq 3.30 approaches 0. Eq 3.30 can be reduced to

$$Q_1 = \alpha Q_\alpha \sin(\omega t - \theta) \quad (3.31a)$$

where

$$\alpha = (1 + (\omega\tau)^2)^{-1/2} \quad (3.31b)$$

$$\theta = \arctan(\omega\tau) \quad (3.31c)$$

where α is a damping coefficient and θ a phase lag. Thus the sensor cannot exactly follow the fluctuating quantity because it will underestimate the change and be out of phase with the fluctuations in time.

Lomas (1986) derives Eq 3.32 for τ of a constant current hot-wire (τ_{hw}) based primarily on Eq 3.16

$$\tau_{hw} = \frac{\rho_s c_s A_s L (\bar{R}_s - R_f)}{\bar{I}^2 \alpha_T R_f R_0} \quad (3.32)$$

where α_T is the temperature coefficient of resistivity, R_0 is resistance at some reference temperature. From this relationship it can be seen that τ_{hw} will increase as the storage term ($\rho_s c_s A_s L$) increases. τ_{hw} also increases with increasing overheat ratio ($\frac{(\bar{R}_s - R_f)}{R_f}$) though this effect is offset by a decrease in τ_{hw} with the inverse square of the mean current. An increase in overheat ratio is typically associated with increased current. In this study constant temperature anemometers are used. This complicates Eq 3.32 by introducing a fluctuating current, (I'), but results in a higher frequency response.

Frequency response is typically the inverse of τ in a given system, though in a randomly fluctuating system it is desirable to define τ at .99 or higher so that almost the entire fluctuation of a quantity at a specified frequency is obtained. Sensor frequency is a critical consideration in experimental design. In the application stu-

died here, sensor frequency response is an order of magnitude higher than sampling frequency so it is not a limiting factor.

The final aspect of hot-film anemometry which needs to be discussed in the general theoretical frame is the angular response of the sensors. The incidence angle of the wind vector with a hot-wire or hot-film sensor can be described uniquely by three angles. The first is called the yaw angle (θ) which is the angle between a line perpendicular to the sensor and the velocity vector, both lying in the plane of the long probe axis. This is the angle to which sensor response is most sensitive. The velocity measured by the sensor is called the effective velocity U_{eff} , and is actually the transverse component of velocity so (following Lomas (1986))

$$U_{\text{eff}} = U_x \quad (3.33)$$

since

$$U_x = U \cos \theta \quad (3.34a)$$

and

$$U_{\text{eff}} = U \cos \theta \quad (3.34b)$$

At very high aspect ratios (Eq 3.18) the cosine is altered by heat transport along the films. In the case of a hot-film, which has a relatively low aspect ratio, obstruction of flow by probe supports or aerodynamic 'end effect' also alters the cosine law and an explicit expression for the yaw sensitivity,

$$\theta_s = \frac{\partial E}{\partial \theta} \quad (3.35)$$

is necessary.

The second angle to be defined is the pitch angle (ϕ). This angle is defined as that made as the sensor is rotated about its own axis. Pitch sensitivity,

$$\phi_s = \frac{\partial E}{\partial \phi} \quad (3.36)$$

is not a strong function of pitch angle and is not dependent on aspect ratio. In most single sensor systems, ϕ_s is small and is due mainly to aerodynamic disruption of the flow passing through probe supports. The third angle to define is the roll angle (ψ). This is the angle made by rotating the probe about the long axis of the probe mount. Again a sensitivity can be defined as

$$\psi_s = \frac{\partial E}{\partial \psi} \quad (3.37)$$

but ψ_s is typically close to zero for cylindrical sensors such as hot-films.

Hinze (1959, referenced in Lomas (1986)) gives the equation

$$U_{\text{eff}}^2 = U_x^2 + k_y^2 U_y^2 \quad (3.39a)$$

where k_y is known as the yaw factor, this equation can be restated as

$$U_{\text{eff}}^2 = U^2 (\cos^2 \theta + k_y^2 \sin^2 \theta) \quad (3.39a)$$

In Eq 3.39, U is stated explicitly if θ is known or vice versa. It is important to remember that U and θ describe the velocity vector completely in two dimensions. Eventually, it will be necessary to describe the vector in three dimensions, determining U , θ and ϕ or U_x , U_y , and U_z (u, v, w). Note that Eq 3.39, when applied in atmospheric flows, is one equation with at least two unknowns.

Complicating the system is the fact that k_y may not be a predetermined constant, but instead it may be a function of θ .

To include pitch angle in this formulation, Jorgensen (1971) proposed

$$U_{\text{eff}}^2 = U_x^2 + k_y^2 U_y^2 + h_p^2 U_z^2 \quad (3.40)$$

where h_p is a pitch factor. Expanding

$$U_{\text{eff}}^2 = U^2 (\cos^2 \theta \cos^2 \phi + k_y^2 \sin^2 \theta \cos^2 \phi + h_p^2 \sin^2 \phi) \quad (3.41)$$

Here then is the beginning of a system of equations which contain all the variables necessary to describe a velocity tensor in space. Still, Eq 3.40 is one equation now incorporating at least three unknowns and possibly five if k_y and h_p are functions of yaw and pitch respectively.

3.3 The TFWOES

At this point in the discussion it becomes less productive to continue a general discussion of hot-film anemometry so the discussion will now become system specific. This section will require some discussion of the sensor operating environment to justify the complexity of the instrument system. The TFWOES system is innovative in many respects and the development, calibration and testing of the system was a group effort. This discussion will closely follow Miller et al., (1987) and personal communications with Dr. J.D. Lin and Y.S. Wang. Though this instrument system is not the focus of this dissertation, the correct interpretation and under-

standing of instrument characteristics is critical to understanding the data that have been collected.

The in-canopy air space is difficult to instrument for many reasons. Inter-element spaces tend to be small and the actual size is time variable as the elements move. Drag forces and body effects dominate so mean velocities are low and turbulent intensities are high. Using the Kolmogorov dissipation equation (Eq 2.3), Fricke (1987) estimates the ASL dissipation length at .7 mm, this agrees with the order of magnitude estimate from Panofsky and Dutton (1984) given in Chapter 2. Arbitrarily assuming a mean wind speed of 1 ms^{-1} and invoking Taylor's hypothesis, this indicates that there is TKE in the ASL at 1 KHz. Invoking Nyquist sampling theory (Eq 4.1), the description of this high frequency energy would require sampling at 2 KHz. Typically, sampling of velocity in the ASL is $O(10 \text{ Hz})$ (Anderson, et al., (1986), see Chapter 5 for discussion of sampling theory and considerations). Still, a fast response sensor is required to obtain information at 10 Hz. Also, an in-canopy sensor should be small so it is not disrupted by the moving canopy and so it does not spatially integrate small turbulent scales due to large sensor size. Further, it helps if the sensor is rugged so that it is not broken during mounting or by the waving of canopy elements.

As pointed out previously, the sensor must be capable of measuring a velocity vector specified by magnitude, orientation and sense. Very little a priori knowledge of the instantaneous flow is available because of the turbulent nature of airflow in the ASL. The velocity sensor chosen for in-canopy measurements is a Thermal Systems Inc. (TSI) model 1294 triple hot-film sensor. The sensor is composed of three mutually orthogonal hot-films. With this system Eq 3.39 can be used to resolve vector magnitude and direction, with the only unknown being the sign of the

vector. This directional ambiguity can be understood by envisioning a velocity vector incident on the three dimensional coordinate system with the three hot-films as the axes. If the direction of the tensor is reversed (rotated 180°), the cooling effect on all the wires would be the same as that with the unrotated tensor. Since reversing flows occur in the complex in-canopy flow field, the problem of directional ambiguity necessitated the development of the WOES.

Here it is necessary to examine a basic procedure for obtaining a velocity from voltages generated by an orthogonal triple-film probe (Gaulier (1977), the treatment in this article is for a triple, orthogonal hot-wire, but the geometry is basically the same). First, each wire must be individually calibrated to empirically quantify the relationship between output voltage and U_{eff} (The calibration procedures used in this research will be discussed in detail later in this chapter.) Though Eq 3.16 is theoretically sound, variations between probes during manufacture make calibration necessary. The basic relationship called King's Law is commonly given as

$$E^2 = A + BU_{\text{eff}}^n \quad (3.42)$$

where A and B are coefficients determined by monitoring E at known values of U_{eff} . The power n is also determined empirically. Many researchers use polynomials to relate E and U_{eff} , generally adding more terms to reduce RMS error between the calibration data and the polynomial. Gaulier (1977) uses

$$E^2 = A + BU_{\text{eff}}^n + CU_{\text{eff}} \quad (3.43a)$$

A is assigned the value of the bridge voltage at zero velocity squared (E_0^2) and is the zero or offset term. Thus

$$E^2 = E_0^2 + BU_{\text{eff}}^n + CU_{\text{eff}} \quad (3.43b)$$

where the coefficients are established by calculating E at various values of U_{eff} which are known by comparison to a calibrated anemometer.

When the voltage-velocity relationship is known for all three wires, a matrix can be written involving three equations and three unknowns. Using Eq 3.40 with the cautions concerning k_y and h_p noted,

$$U_{\text{eff},1}^2 = U_x^2 + k_{y,1}U_y^2 + h_{p,1}^2U_z^2 \quad (3.44a)$$

$$U_{\text{eff},2}^2 = U_x^2 + k_{y,2}U_y^2 + h_{p,2}^2U_z^2 \quad (3.44b)$$

$$U_{\text{eff},3}^2 = U_x^2 + k_{y,3}U_y^2 + h_{p,3}^2U_z^2 \quad (3.44c)$$

where the numeric subscripts indicate the three wires respectively. Note that the author has made k_y and h_p wire specific though Gaulier (1977) treats them as system specific so that

$$k_{y,1} = k_{y,2} = k_{y,3} \quad \text{and} \quad h_{p,1} = h_{p,2} = h_{p,3} \quad (3.45)$$

for a given sensor assembly. In the procedure used in this experiment, only the yaw correction (k) is utilized and it is made sensor specific.

The previous scheme for obtaining velocity from hot-wire output voltage was presented because of its clarity. The actual scheme used in this experiment takes a different tack and is substantially more complicated due to the inclusion of the WOES output signal to unambiguously describe the velocity sensor in three dimensions. The basis for the adopted scheme comes from TSI Technical Bulletin #8. Calibration and laboratory testing of the instruments was conducted in front of a circular, contracting wind nozzle, 8 cm in diameter. The air is pushed by a 40 cm

fan through drinking straws to remove large-scale vorticity and the flow is constricted to increase velocity and reduce the turbulent intensity. The velocity range that can be generated with this tunnel is 0 to 10 m s⁻¹, with baffling of the intake required to reduce the velocity below 1 m s⁻¹. A complete discussion of the wind tunnel and its flow characteristics is in Miller et al., (1987).

The films are 1 mm long and .051 mm in diameter including the substrate, with the space between mounting needles being 1.67 mm. The manufacturer specified frequency response is 200 kHz. Each wire was individually calibrated by positioning it perpendicular to the flow direction. The flow was also monitored by a pitot tube and a Datametrics model MM3 micromanometer. At each velocity, the micromanometer was allowed to come to equilibrium and a reading was taken. The anemometer output voltage was then either read by eye from a digital voltmeter or the average voltage of a 1 second, 20 Hz sample was recorded. This procedure was repeated for 20 values of velocity for each wire. The form of the calibration equation chosen was a fourth order polynomial

$$U_{\text{eff}} = C_1(\Delta E_i) + C_2(\Delta E_i)^2 + C_3(\Delta E_i)^3 + C_4(\Delta E_i)^4 \quad (3.46)$$

where C_i are empirically determined coefficients and

$$\Delta E_i = E_i - E_{0,i} \quad (3.47)$$

where E_0 is the bridge output voltage at zero velocity. This method was developed by Miller et al., (1987) as a way to compensate for ambient temperature fluctuations. Before a velocity time series is collected in the field, the sensors are covered and E_0 is obtained. This voltage is then input into the velocity calculation by the data processing software. This temperature compensation technique appears to

work well in the ambient temperature range encountered in these experiments (8° to 26° C). The process of obtaining E_0 for a given data set will subsequently be called a 'zero run'.

The next step is to relate U_{eff} to U and to obtain vector orientation. Begin with Eq 3.39 rearranged and subscripted

$$\frac{U_{\text{eff}i}^2}{U^2} = \cos^2 \phi_i + k_{y,i}^2(U) \sin^2 \phi_i \quad (3.48)$$

where k_y is explicitly given as a function of velocity and the i subscripts indicate films 1, 2, and 3. In the orthogonal system

$$\sum_{i=1}^3 \cos^2 \phi_i = \cos^2 \phi_1 + \cos^2 \phi_2 + \cos^2 \phi_3 = 2 \quad (3.49)$$

leaving four equations and four unknowns (ϕ_1 , ϕ_2 , ϕ_3 , U),

$$\frac{U_{\text{eff},1}^2}{U^2} = \cos^2 \phi_1 + k^2(U) \sin^2 \phi_1 \quad (3.50a)$$

$$\frac{U_{\text{eff},2}^2}{U^2} = \cos^2 \phi_2 + k^2(U) \sin^2 \phi_2 \quad (3.50b)$$

$$\frac{U_{\text{eff},3}^2}{U^2} = \cos^2 \phi_3 + k^2(U) \sin^2 \phi_3 \quad (3.50c)$$

$$2 = \cos^2 \phi_1 + \cos^2 \phi_2 + \cos^2 \phi_3 \quad (3.50d)$$

This system of equations can be used to solve for vector magnitude and direction as follows

$$U = \left[\frac{\sum_{i=1}^3 U_{\text{eff},i}}{2 + k^2(U)} \right]^{1/2} \quad (3.51)$$

then

$$\phi_i = \arcsin \left(\frac{1 - \frac{U_{\text{eff},i}^2}{U^2}}{1 - k^2(U)} \right)^{1/2} \quad (3.52)$$

and

$$U_i = U \sin \phi_i \quad (3.53)$$

where U_i is the vector component in the direction of each sensor. Operationally, Eq 3.52 causes difficulty due to the fact that if the bracketed term on the rhs of the equation is not between 0 and 1, the term is mathematically undefined. This problem apparently arises at high ϕ because k is a function of ϕ , as well as being a weak function of U and being somewhat sensor specific. Define

$$R_i = \left(\frac{1 - \frac{U_{\text{eff},i}^2}{U^2}}{1 - k^2} \right) \quad (3.54)$$

(following Lin (1986, unpublished)) the undefined cases are $R_i < 0$ and $R_i > 1$.

When $R_j < 0$, ϕ_j is set to zero. Then

$$U^2 = \sum_{\substack{i=1 \\ i \neq j}}^3 \frac{U_{\text{eff},i}^2}{(1+k^2)} \quad (3.55)$$

is calculated and solve Eq 3.52 for $i \neq k$.

Considering the case where $R_j > 1$, set $U_{\text{eff},j} = kU$ and $\phi_j = 90^\circ$. When the wind vector is parallel to one sensor in an orthogonal system it must be perpendicular to the other two so $U = U_{\text{eff},j}$ when $i \neq j$, since the two remaining vector magnitudes may not be exactly equal, use

$$U^2 = \frac{1}{2} \sum_{\substack{i=1 \\ i \neq j}}^3 U_{\text{eff},i}^2 \quad (3.56)$$

which averages the two $U_{\text{eff},i}$, $i \neq j$.

At this point, the signs of the component velocities, U_i , have not been assigned and it is necessary to combine the velocity data with the signal from the WOES. The idea of using a cube with opposing temperature sensitive bridges on each face to resolve vector direction was first investigated by Fox and Brazee (1978). The WOES used here is much smaller than that used previously, it is a one cm cube which is mounted approximately 5 cm from the triple hot-film sensors. It was constructed for these experiments by TSI. Opposing faces of the cube comprise opposite legs of a bridge circuit. Differential cooling by the wind causes a bridge

unbalance which is measured. Heating of the sensors allows enhanced sensitivity. There are three independent bridges because there are three sets of opposing faces on a cube.

To use the WOES, a zero voltage must be established because the it varies with ambient temperature. This voltage, $E_{0,w}$, is obtained at the same time E_0 for the film is obtained during a zero run before a measurement run. When exposed to a flow, each bridge shows an imbalance towards one face, when the signs from each pair of sensors are combined, the direction of flow is described to an octant of the sphere. The WOES is mounted so it shares the same reference coordinate system as the hot- film sensors it is mounted in conjunction with.

The final step in using the TFWOES is a coordinate transformation. The TF probe is manufactured such that if the positive axes of a 3- dimensional rectangular coordinate system are envisioned, the three orthogonal wires come towards each other with each wire representing an axis. If a line can be imagined extrapolated from each wire, following the long axis of the wire, the lines would intersect at the origin of the envisioned system. The problem is that due to the position of the mounting block and the fact that it is desirable to avoid the situation described previously where $R_j > 1$ (Eq 3.54), none of the three orthogonal planes in this system are parallel to the ground. To achieve the standard coordinates where U_x and U_y are in the horizontal plane and U_z is in the vertical , a coordinate rotation is required.

If two sets of orthogonal, 3-dimensional axes are overlaid with origins at the same point and one is rotated, each axis makes an angle with each axis of the other

system. If one set of axes is designated by the subscript i (instrument) and the other set by the subscript f (fixed), the angle matrix can be written

$$\begin{array}{cccc} & x_i & y_i & z_i \\ x_f & \alpha_{x,x} & \alpha_{x,y} & \alpha_{x,z} \\ y_f & \alpha_{y,x} & \alpha_{y,y} & \alpha_{y,z} \\ z_f & \alpha_{z,x} & \alpha_{z,y} & \alpha_{z,z} \end{array} \quad (3.57)$$

where $\alpha_{i,f}$ is the angle between the indicated axes. Then a velocity vector in instrument coordinates is transformed to the fixed coordinate system by

$$U_{f,x} = U_{i,x} \cos \alpha_{x,x} + U_{i,y} \cos \alpha_{x,y} + U_{i,z} \cos \alpha_{x,z} \quad (3.58a)$$

$$U_{f,y} = U_{i,x} \cos \alpha_{y,x} + U_{i,y} \cos \alpha_{y,y} + U_{i,z} \cos \alpha_{y,z} \quad (3.58b)$$

$$U_{f,z} = U_{i,x} \cos \alpha_{z,x} + U_{i,y} \cos \alpha_{z,y} + U_{i,z} \cos \alpha_{z,z} \quad (3.58c)$$

The fixed coordinate system used in this study has positive $U_{f,z}$ vertically upward. $U_{f,x}$ is in the horizontal plane either pointing west (towards the edge) or east into the forest depending on mean wind direction. $U_{f,y}$ is perpendicular to $U_{f,x}$ in the horizontal plane. Further vector rotations into the mean wind were performed and will be discussed later. It will facilitate the discussion to adopt meteorological convention and assign $U_{f,x}$, $U_{f,y}$ and $U_{f,z}$ to u , v and w respectively for the rest of this paper.

Field comparison tests of the TFWOES system with a Gill 3-dimensional propeller anemometer and a Campbell vertical sonic anemometer are discussed in Miller et al., (1987). There are many sources discussing specific applications and problems in hot-wire and hot-film anemometry. Discussions of ambient temper-

ature and humidity corrections (Machen ,1986, Larsen and Busch ,1980), calibration and measurement in flows of low velocity and/or high turbulent intensity (Aydin and Leutheusser ,1980, Acrivellis 1977, and Siefert and Graichen 1982), and contamination and calibration drifting (Zank ,1981, Martinez-Val, et al., 1982) are available in the literature.

A final consideration here is sensor fouling or contamination. The in-canopy environment is inherently dirty. Dust, dirt and organic debris can build up on a thermal sensor and lessen or alter the sensitivity by changing the parameters in Eq 3.16. Sensor frequency response is sensitive to fouling but since the sampling is not conducted near maximum frequency response, this is not a concern here. Miller, et al., (1987) gives results showing only a 3 % decrease in sensitivity after over a month of field runs. In less formal tests, the author and Y.S. Wang saw a decrease of less than 10 % occurring over a six month field season (4/85- 10/85). Another form of fouling which is of concern are step changes in wire resistances caused by larger particles or biological activity. Though occasional unexplained spikes do appear in these data, the only serious problems of this type which were encountered were due to creatures (probably spiders) building webs on the sensors. The webs effectively shorted the films together making them useless, but the problem is alleviated by removing the webs.

3.4 The Data Acquisition System

The data acquisition system is discussed here because the range and the resolution of the analog- to-digital converter (A \rightarrow D) used in the experiment establishes the interfacing considerations for the rest of the instrument systems.

The data acquisition system is run by a LSI 11/23 computer in a 9x4 Q- bus. The system includes a Scientific Micro-systems 35.6 megabyte Winchester hard disk. There is also 256K on board memory in the bus. For storing large data sets and for system back-up, the system includes a Digi-Data model 1740 9-track tape drive. Data collection is performed using two, 32 channel, differential input, Data Translation 3382-DI A \rightarrow D converters and the associated front panels with male BNC connectors for input. These are 12 bit A \rightarrow D converters with a range of +10 to -10 volts. A \rightarrow D converters consist of a series of test gates. At each gate an input signal is tested as to whether it is above or below a certain voltage. Above and below lead to different gates where another test is performed. In this way, a 12 bit A \rightarrow D converter can yield 2^{12} (4096) different 'answers'. If the range of the A \rightarrow D is +10 V to -10 V, then the resolution of the A \rightarrow D is $20/4096$ or 4.9 mV. Thus the fundamental resolution of this system is approximately 5 mV. Maximum sampling frequency in this system is 50 kHz per board. The maximum per channel frequency is 50 kHz divided by the number of channels being scanned. Access to the A \rightarrow D boards is obtained through system subroutines which contain the appropriate device calls and initiate sampling. Data is moved through the buffer and put on the hard disk. Software is discussed in more detail in Chapter 4. The system is run by the RT-11 operating system. The terminal is a VT-101 and the printer is a Decwriter IV.

The research group has become familiar with the data logging system over the past four years. It is a reliable system, though it has occasionally failed during the rigors of fieldwork. Some cautionary notes are required when using the system. First, abrupt power downs should be avoided, especially during disk write operations. It is possible for the write head to crash under such circumstances, damaging the hard disk. Second, the system is protected against input spikes up to 25 V

when power is off and 35 V when the system is powered up. If there is any chance of these values being exceeded, inputs should be removed from the front panels. Third, the front panel shows marked neighborhood effects. Large voltages in one channel will cause surrounding channels to be overwhelmed. Also, the manual states that open channels surrounding data gathering channels should be shorted. Spikes of the magnitude discussed in the second consideration are not difficult to generate with the bridges and amplifiers being used. The third consideration can cause loss of data, the second can cause damage to hardware. Therefore, spiking in input signals can be a serious problem.

3.5 Temperature Sensors

The second instrument system involved in this experiment is a high resolution thermocouple temperature system. The specifications for this system were developed by the author and Dr. D. E. Anderson. The custom design and manufacture of the system was performed by Science Engineering Associates of Willington, CT.

Thermocouple temperature systems operate on the basic assumption that if two junctions of dissimilar metals exist in the same circuit at different temperatures (ΔT) then an electric current will be generated proportional to ΔT . The electromotive force producing this current is known as the Seebeck emf (named after the scientist who first observed the effect in 1821). The current generated per $^{\circ}\text{K}$ of ΔT is a property of the two metals forming the junctions.

Thermocouple thermometry is a widely used, extensively documented method so it is not necessary to discuss it in detail here. Certain basic properties of thermocouples are discussed to provide the background necessary to understand the system used in this experiment. Following Fitch (1962), the three laws of thermocouple thermometry are

1) The Law of the Homogenous Circuit states that a current cannot be maintained in a circuit of homogenous metal by the application of heat without any other current source.

2) The Law of Intermediate Metals states that the sum of emfs in a circuit is zero if the circuit is at a uniform temperature.

3) The Law of Successive or Intermediate Temperatures states that if two dissimilar metals produce an emf of E_1 when the junctions are at T_1 and T_2 and E_2 when the junctions are at T_2 and T_3 , the emf when the junctions are at T_1 and T_3 will be $E_1 + E_2$.

The thermocouples used in this study are 2 ml, copper-constantan. This type of thermocouple produces a voltage of approximately $42\mu\text{V}$ per $^{\circ}\text{K}$. The emf is actually a non-linear function of temperature in the ambient range so a polynomial is used to relate ΔT and voltage. Signals on the order of $10\mu\text{V}$ can be difficult to measure, especially when transmission of the signal is required over long distances because of noise induction in the cables. Also, there is the problem of matching thermocouple outputs to the A \rightarrow D which has a minimum resolution of 5 mV, or 100x the thermocouple output at $\Delta T = 1$. For this type of high frequency data

collection, it is desirable to be able to resolve $O(.01^\circ\text{K})$. This requires resolving the thermocouple output to $O(.1\mu\text{V})$.

It became apparent at the outset of the design deliberations that it would be desirable to restrict the range of ΔT . This would limit the maximum thermocouple output voltage and would allow increased amplification that otherwise would produce voltages that would exceed the maximum range of the $A \rightarrow D$. For example, in a data collection run of one hour the average temperature may drift 2°C from 20° to 22° . Superimposed on this mean signal are turbulent fluctuations which are a maximum of 2° in magnitude. This leaves an 'active' range of $18^\circ - 24^\circ\text{C}$ during the run. It would in this situation be desirable to have a reference junction at or near 21°C to minimize ΔT . (The emf signal changes sign as ΔT goes through zero.) Until the past decade, reference junctions were typically ice-baths or ovens. If we take the case of an ice-bath, there would always be a background signal in the run under consideration here of $756\mu\text{V}$, while the fluctuating part of the signal would cover $252\mu\text{V}$. Thus, after amplification, 75 % of the range of the $A \rightarrow D$ would contain only mean information. State of the art thermocouple systems often include a variable electronic source which imitates a reference junction. The problem with this approach in this experiment is that each sensor would require a source at the sensor to prevent induction in long leads and cables. Also, knowledge of the mean temperature would be necessary to set the reference voltage. This is an expensive proposition since microvolt sources are typically unstable and temperature sensitive, precision instrumentation is required.

Incorporating these considerations, a design was developed which uses a sensing junction and a potted, floating reference junction located in the pre-amp housing. The housing is wrapped in white tape to decrease the effect of incident solar radi-

ation. Using this method, the mean value is differenced and the fluctuating value remains.

The author has examined a worst case scenario for box temperature drift. At high values of solar radiation (600 W m^{-2} which is well above typical values of solar radiation at the latitude and the season being examined) the drift could be as high as 1°K in $O(10 \text{ s})$. Drift of this magnitude was not encountered in these experiments for various reasons. The reference junction is potted in adhesive which insulates it. Also, the boxes reached equilibrium temperatures after a certain amount of heating. Finally, radiation regimes were typically mild and much of the work was done in the shade below canopy. However, this effect could be significant in runs where the boxes were exposed to intermittent sunlight such as partly cloudy days and below canopy runs when sun flecks are moving under the canopy. The latter effect is probably too high frequency to affect the reference junctions unless the sensor is moved and not allowed to equilibrate. Radiation effects must be considered when evaluating the sensing junction as well, although the absolute value of heat involved in raising junction temperature is so small that it is quickly removed by convection. Thus radiation effects at the sensing junction may be enhanced under very low velocity conditions. These effects will also be more important in the intermittent radiation conditions described above. Using this system, both junctions are located at the location of measurement. The thermocouple junctions are 25 cm apart. The thermocouple leads are mounted between two pot markers, made of wood. The 8 cm of lead before the sensing junction is extended out on a thin, rigid, white plastic strip and the final 2 cm before the junction is left unsupported in an attempt to minimize heat conduction to the sensing junction.

Since both thermocouple junctions are at the location of measurement it is still necessary to send a microvolt signal over a length of cable. In this experiment, the maximum distance temperature signals travelled was approximately 75 m. To alleviate this problem, a pre-amp is stationed at each sensor. This also provides the housing for the reference junction. Pre-amplification is necessary because some noise will always be present, even in shielded cable. If a $50\mu\text{V}$ is sent, and a $5\mu\text{V}$ background noise is inducted into the cable, the signal-to-noise ratio (S/N) is 10. If the signal is amplified 100x before transmission, the S/N ratio in the same situation is raised to 1000. Precision amplification under these circumstances is difficult because typical operational amplifiers (op-amps) are temperature sensitive. Op-amps made to military specifications were obtained which, though more expensive, show almost no temperature sensitivity in the ambient range. Another consideration is that distortion increases with gain in all amplifiers. Therefore, all the amplification necessary to match the temperature signal to the A \rightarrow D was not performed in one step. Instead, a two- stage amplification was performed with 100 gain at the sensor and 100 gain in front of the A \rightarrow D at the computer. This results in a system gain of 10000x. So the $\Delta T = 1$ voltage of $42\mu\text{V}$ is stepped up to 420 mV. This is over 80x the minimum resolution of the A \rightarrow D and would allow a minimum temperature resolution of $< .02^\circ\text{C}$ and a maximum range of $\pm 20^\circ\text{C}$. A minimum resolution of $< .02^\circ\text{C}$ may not be real due to error introduced by radiation effects and other considerations such as conduction in leads and sensor to sensor variability due to material inhomogeneity. Still, a conservative estimate of this system would yield a minimum resolution of $.04^\circ\text{C}$. Finally, as a precaution against noise induction at 60 Hz due to power cords, the signal is electronically filtered at 50 Hz before it is input to the A \rightarrow D.

3.5 Other Instrumentation

The last three sensors involved in this study are standard commercially available systems. Reference velocities were obtained with a three-dimensional Gill anemometer (Horst (1973), Gill (1975) and Bowen and Teunissen (1986)). The Gill (Gill UVW Anemometer Model 27004) consists of three orthogonal arms with 19 cm diameter, polystyrene propellers at the end of each arm. The propellers are 40 cm from the body of the Gill. In each arm is a brush generator. In the range of wind speeds encountered in these experiments (typically $< 8 \text{ ms}^{-1}$) the manufacturer specified generator output is 83 mV at 1.5 m s^{-1} . Due to the fact that the incidence angle at the vertical propeller is almost always $> 30^\circ$ the sensitivity at the vertical propeller is decreased by approximately 20%. The variation between generators was measured by the author as $< 4\%$. Therefore, the same calibration was used for each horizontal Gill signal. The threshold velocity of the Gill is $.2 \text{ ms}^{-1}$ with frequency response $O(1 \text{ Hz})$. Since the Gill was used above canopy, the threshold velocity was not usually a problem. Gill signals were sampled at the same frequency as the hot-films and filtered to 1 Hz with an averaging algorithm before statistical analysis.

The Gill shows marked cosine response at high angles of incidence. This is compensated for by a correction algorithm which compares the ratios of the outputs from the sensors and assigns appropriate correction factors (see Horst (1972)). The correction is incorporated in the software before statistical analysis is performed.

Included in the instrument array is a CA27T Sonic Anemometer which has a fine wire thermocouple mounted in it. This is a one-dimensional instrument with a

speaker and receiver mounted approximately 12 cm apart. The instrument utilizes the Doppler effect and senses shifts in acoustic wave frequency which are proportional to the velocity of the intervening fluid. The instrument is mounted so the vertical component of the wind is measured. Heat flux can be measured using the thermocouple which is mounted beside the sonic path on the body of the sensor. The output of this anemometer is $1 \text{ V} = 1 \text{ ms}^{-1}$ which makes it compatible with the A \rightarrow D. Finally, a Li-Cor (Model LI-200SB) was used to monitor solar radiation. This instrument uses a photodiode which yields an output voltage proportional to incident solar radiation. Since the output voltage is 10 mV per 1000 Wm^{-2} , amplification of 100x was used to match the signal to the A \rightarrow D. This results in a minimum resolution of approximately 4 Wm^{-2} in this system.

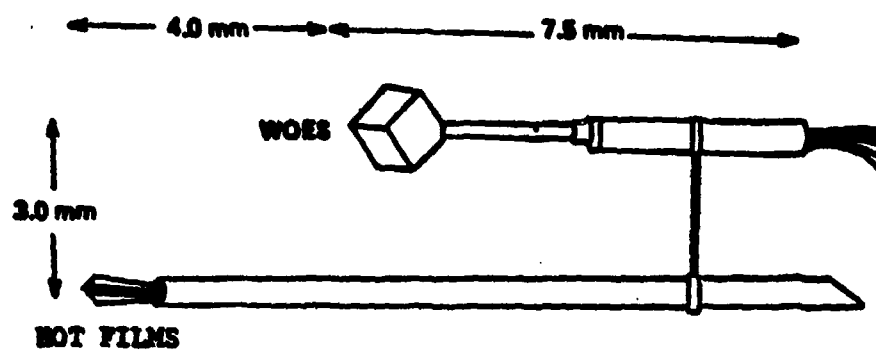


Fig. 1 Diagram of TFWOES directional anemometer from Miller, et. al. (1987).

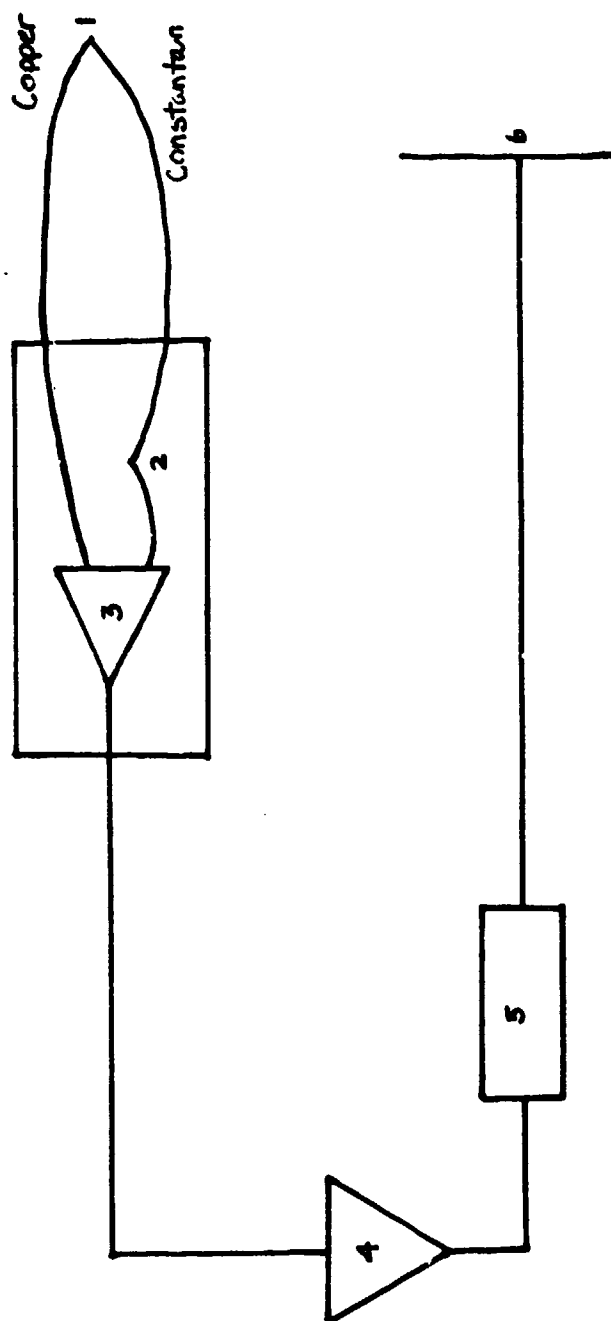


Fig. 2 Block diagram of the temperature sensing system with 1) Copper-Constantan sensing system 2) Reference function 3) Pre-amp 100x at tower 4) Amp 100x at mobile computer van 5) Low pass filter at 50 Hz 6) A → D

Chapter IV

Experimental Design

4.1 Experiment Site

The experimental site is approximately 10 km west of the University of Connecticut, Storrs campus in Coventry, Connecticut (Lat. $41^{\circ} 47' 30''$ N, Long. $72^{\circ} 29' 29''$ W). Regionally, the site is in the Eastern Highlands of Connecticut with rolling, broken glacial terrain rising to over 300 m elevation approximately 20 km NNE of the site, with the edge of the broad, flat Connecticut River Valley (elev. less than 75 m) approximately 15 km to the west. The site is on the eastern edge of the Skungamaug River Valley which is approximately .75 km in width at this point. It is at 150 m elevation with a ridge to the east and northeast of the site which rises to over 190 m within 1 km. The site is on the southeast corner of a flat cornfield approximately 250 m x 400 m. Fetch over flat terrain is greatest to the northwest of the site extending .5 km. East winds (forest fetches) pass over relatively flat terrain from the southeast while northeast winds encounter the ridge mentioned

previously (Figure 3). The physical description of the site, including canopy architecture, is well documented (Miller and Lin,(1985) , Wang (1985), Wang and Miller,(1987)).

The site transects the western edge of a relatively homogeneous stand of red maple (*Acer rubrum*). One white pine (*Pinus strobus*) and a clump of trembling aspen (*Populus trembloides*) are the only exceptions near the edge of the stand. The site is typically under water in the spring and is usually dry in the summer and autumn. Average tree height is 14 m with the tallest tree being 18 m. The stand extends to the base of a ridge as previously described, though there is a woods road and a small clearing approximately 100 m east of the site.

The foliated canopy at this site is described in detail in Wang and Miller (1987), Wang (1985) and Miller and Lin (1985). Photographs of the unfoliated canopy were taken during the spring runs. The personnel lifts were used to take LAI photographs at various heights to determine the vertical distribution of the leaves. Computation of LAI from the photographs will be discussed in Chapter 5.

Displacement height, d , was calculated from velocity profiles (Rosenberg, 1974) as approximately 11 m for the foliated and 4 m for the unfoliated canopy LAI shows a strong maximum at 11m in the foliated canopy, while stem area in the unfoliated canopy shows a weaker maximum at around 9m.

Four towers were used at the site during this experiment. Two of the towers are semi-stationary triangle towers and two are mobile personnel lifts. The primary tower is a stationary tower positioned 34 m east of the edge, into the forest. This interior stationary tower (IS) consists of nine sections of 3 m each, bolted together

and guyed every two sections. This tower served as the main profiling tower in these data sets. Another stationary tower is at the edge (ES). This tower is 20 m high and similar to the IS tower in construction. Though this tower was initially included in the edge transect arrays, none of the data that were eventually categorized 'good' and analyzed includes an anemometer at this station. This is because when one sensor was out of the array for repairs (as was almost always the case) the ES position was the one that was given up. It is believed that the flow field right at the edge might be the most difficult to interpret and therefore the least useful at this stage of the investigation. These two stationary towers establish the east-west line that was used for the edge transects.

The other two major towers used are both hydraulically operated portable personnel lifts. These portable towers are on wheels, the towers weigh 1400 pounds each and are capable of raising 500 pounds 12 m. These towers are stabilized by inserting (4) 2.5 m outriggers which run parallel to the ground extending diagonally outward at each corner of the tower. Screw down bases at the end of each outrigger lift the weight off the wheels and allow levelling. Extension supports are then set-up. These run from the body of the tower to the end of each outrigger forming a right triangle with the ground.

One of the portable towers was set-up 22 m east of the edge in the forest between the two stationary towers. The exact position of the tower is determined by a natural opening in the canopy at this point. Placed in the bucket of this tower is a collapsing extension tower raised by a cylinder of CO₂ gas. This smaller tower extends up to 8 m so the maximum height achievable at this interior portable (IP) tower is almost 20 m.

The second portable tower was set-up on the transect line two tree heights ($2H$, 28 m) west of the edge outside of the forest. In the bucket of this external portable (EP) tower was clamped a 3.5 m long, 5 cm diameter aluminum pipe. Instruments were mounted near the top of the pipe and the clamp allowed the pipe to be slid up and down for servicing. This extension allowed a maximum height of over 15 m to be achieved at the EP station. Finally a smaller tower consisting of two 3 m sections of triangle tower was set-up at the transect line, $3H$ west of the edge. This tower was used in the summer and autumn runs and served as a permanent Gill station. The height of the gill here is constant during all runs at approximately 6.25 m.

It should be noted that 10 m west of the external Gill (EG) station, the corn field begins. The corn was over 3 m high during all of the foliated data collection runs and it is likely that the corn has a strong influence on the flow fields at EG and EP. Some of this influence may be examined by comparing data during east and west winds. A cross-section of the edge and the towers is presented in Figure 4.

4.2 Data Collection

Flow data have been gathered at this site during the foliated season since 1984. Some of these data are presented by Lin and Miller (1985) and are described as preliminary. Though the instrument and software systems had not completely evolved when these data were collected, it provides a useful framework and was utilized as a basis for the experimental design used in this study. The data presented in Lin and Miller (1985) is composed primarily of 3 minute runs sampled at 10 Hz. From these data it appears that there is production in the horizontal components

within the stand at a frequency of around 1 Hz. Above canopy flows with forest fetch show a dominant frequency around 1 Hz with secondary peaks between .5 and 5 Hz. These preliminary spectra are not ensembled but similar patterns appear in many of the spectra. Flows across the edge show less regularity, probably due to the disruption of the edge compounded by directional variance between data sets. Of interest is the fact that the equilibrium subrange in the spectra of u' in these flows begins at 1-2 Hz above the canopy but shifts to higher frequencies (3-5 Hz) in the canopy. This is interpreted as indicating high frequency turbulent production by canopy elements. These preliminary spectra were not scaled, so all frequencies are natural frequencies (n_f).

Five basic instrument arrays were used in this study with minor variations. They are

- 1) Comparison Rake
- 2) Vertical Profile at IS
- 3) Edge Transect in High Position
- 4) Edge Transect in Middle Position
- 5) Edge Transect in Low Position

The rake was established close enough to the bus that the bridges could be kept in an air conditioned environment to eliminate the effects of ambient temperature fluctuation on the electronics (it was subsequently determined that the effect is negligible). The rake consisted of TFWOES 22, TFWOES 23 the Campbell vertical anemometer and a Gill anemometer. A temperature measurement was associated with each anemometer. The instruments were mounted on a cross bar on the front of one of the personnel lift buckets and raised approximately 6 m into the air (see Diagram for exact array spacing). The rake was approximately 1 H (14 m) west of the edge and the sensors were oriented into the mean wind during the runs. The

comparison rake data and results are discussed in Miller, Lin, Wang and Thistle (1987).

The second array was a profile at the IS tower. This profile consisted originally of (4) TFWOES, a Gill UVW anemometer and a sonic anemometer along with temperature sensors at each station. The profile was set-up with TFWOES stations at 3 m in the trunk space, 11 m near maximum LAI, 16.5 m at the top of the canopy and 20 m above the canopy. Due to sensor breakage, all the profile runs used in the data analysis have 3 TFWOES stations, with the 20 m station having been removed from the array. Above the TFWOES stations at 24 m were mounted the Gill anemometer and the sonic anemometer, approximately 2.5 m apart on opposite ends of a cross bar. The Gill centerpost was approximately 1.5 m and the sonic approximately 1 m. from the tower. Also in this array is a Gill at the top of the 6 m tower 3H west of the edge and a Li-cor pyrheliometer approximately 1 m off the ground, 10 m west of the edge.

The final set of arrays are the horizontal edge transects which are used for spatial and event analysis of the flow. TFWOES were mounted on towers at EP, IP and IS in the transect runs. Temperature sensors were mounted at each TFWOES station. Also in the arrays were Gill UVW anemometers, the sonic vertical anemometer and a Li-Cor pyrheliometer, all of which were positioned as described previously, and these instruments remained in these positions during all the transects. Transects were run with all of the TFWOES at IS and IP at 20 m while the TFWOES at EP was at 15 m (high position). The TFWOES at EP in the high position is lower than the other two stations in this position because the personnel lift and the extension used at EP does not reach as high as the other towers.

Mounting and levelling the TFWOES system was a tedious and difficult task in these experiments. Subsequent work, largely in response to problems encountered in these experiments, has standardized the procedure, improving it markedly. The combined length of the mounting arm and the sensor arm allowed the sensor to be extended out from the tower approximately 75 cm with a variation in this length of about ± 10 over the course of the data collection. Temperature sensors and preamps were mounted using telescoping aluminum arms and were positioned above and slightly behind (downwind of) the TFWOES. The temperature sensors were typically 15 cm from the TFWOES sensors though this distance varies ± 50 due to the difficulties encountered in mounting the two arms in close proximity.

Before data collection, each sensor was covered for a zero run with a brown paper bag, reinforced by a wire skeleton for rigidity. After all the sensors were covered, data were collected for 50 seconds at 20 Hz. These runs were used to detect problems with the sensors such as shorts, opens, spikes, etc. After troubleshooting was completed a 50 sec zero run was sampled and saved. After the zero run is completed, the sensor covers are removed and the sensors are re-levelled. Zero runs and leveling were usually performed every other run during high frequency sampling and before every low frequency data set was collected.

Sampling frequency and lengths of the runs were determined by the author using the available flow data, Nyquist theory and the storage characteristics of the computer. The Nyquist frequency defines the minimum sampling frequency required to extract information at frequency f for period P :

$$N_f = 2f = \frac{1}{2P} \quad (4.1)$$

and even this relationship assumes a prior knowledge of the function being sampled. Sampling lower than the Nyquist frequency can cause aliasing or the inference of lower frequencies than are actually present. Blocking and buffer considerations, dictated by the computer system, established the maximum length of the data blocks. Square wave tests were run to determine the length of the interblock gaps.

At the high frequency end, since preliminary data indicated information in the in-canopy spectra at 5 Hz (Miller and Lin, 1985) it was decided to sample at 20 Hz. The dissipation range in the atmosphere is $O(1 \text{ mm})$ as discussed previously. To sample this frequency fluctuation (assuming sufficient sensor sensitivity) would require sampling in the KHz range. Though these frequencies do exist in the atmosphere, spectra indicate (Anderson, et al., 1986) that the energy at these frequencies is negligible. There is an inherent trade-off in this type of experiment between sampling frequency on the one-hand and storage availability and processing costs on the other (Tan-atichat and George, 1984). Blocking limitations allowed 100 seconds of data at 20 Hz and 360 seconds at 5 Hz. Therefore, the data are composed of two types of sets, high frequency data which are 20 Hz data sampled for 100 seconds per block. The high frequency sets are composed of either 3 or 4 blocks per set. The second type of data set are low frequency data, sampled at 5Hz for 360 seconds per block. All of the low frequency data sets consist of 10 blocks each. A detailed description of data collection and processing software is given in Appendix 1, and a detailed user manual including the Fortran source codes is being prepared by the author.

Data collection was conducted in three sessions. The first was in the spring of 1986 before leafing occurred in the stand though the maples did blossom during this time period. After the spring runs, two experimental changes were made. First it

was decided that housing and heating of the bridges in the field was not necessary. Laboratory tests at a range of ambient temperatures (approximately 10°C - 30°C) demonstrated that if there were ambient temperature effects on the electronics, they were compensated for by using $E - E_0$ in the calibration polynomial. No data extensively analyzed in this study was collected at temperatures less than 7° . Bridge housing is not desirable in hot weather unless it is well ventilated because the restricted circulation around the bridges can restrict convectional cooling and internal heating of the bridges.

The second major problem in the spring runs was one of electrical noise in the sensor signals. The noise problems were of two distinct types. The first is a spiking which seemed to occur at the beginning of data blocks and which was of sufficient magnitude to obscure instrument signals. The second type was persistent periodic noise which rippled throughout the data sets. The periodic noise seemed to ride on the mean signal so that it did not have a strong effect on the mean statistics but turned up as spikes in the spectra typically between 1 to 10 Hz. This noise appeared to be in phase on all of the channels because it would substantially increase computed between channel, zero-lag correlations.

It was decided to common all shield cables at the bus and tie this into the chassis of the computer which is tied to a utility ground. In this way, all the bridges, the A \rightarrow D and all cable shields were brought to a common ground. This eliminated the periodic noise. It is worth noting that the stationary towers are grounded because they are anchored with metallic stakes. This means that there are at least two possible grounds in the system. If instrument chassis are allowed to touch the towers, a marked reduction or fallout is noticed in the bridge output signal. (See Diefenderfer, 1979 for a technical discussion of electrical noise.)

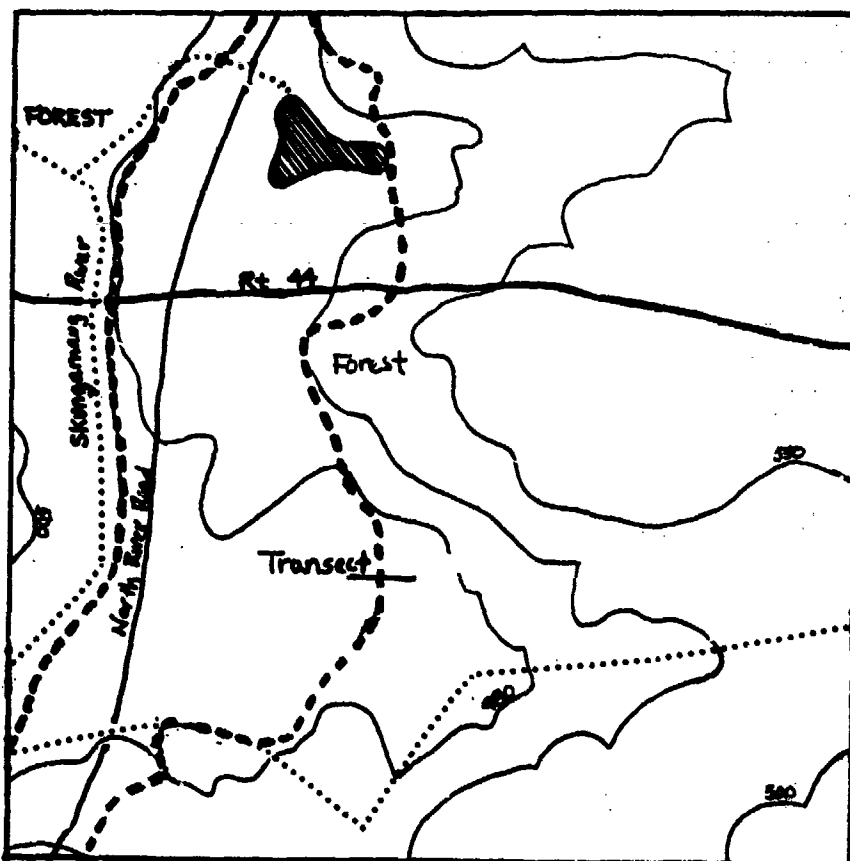
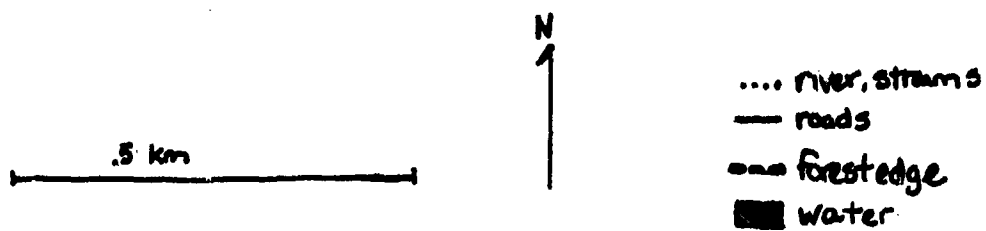


Fig. 3 Map of site situation with tower transect demarcated.



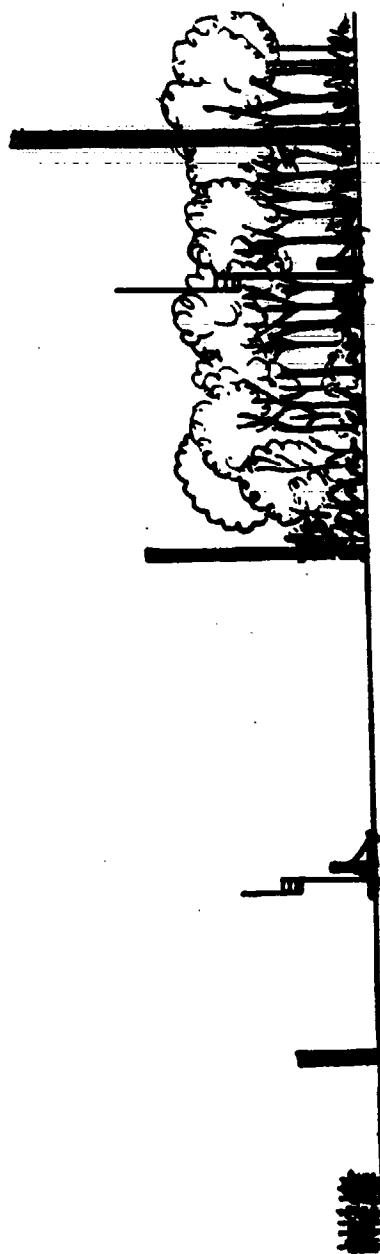


Fig. 4 Schematic cross-section of site showing position of towers (Note that the edge tower was not used in this study). See Chapter 4 for detailed description of site.

Chapter V

Statistical Methods

5.1 Introduction

Interpretation of the turbulence data that were gathered is accomplished using documented techniques such as spectral analysis (Priestly, 1981) and quadrant (hole) analysis (Shaw, 1985). Further insight is sought by the application of conditional sampling/windowing techniques which have been developed in this study. Initially, extensive 'mean' analyses are performed on the data. These allow preliminary interpretation, as well as a degree of quality control. Also, all conventions, rotations and conditional tests applied to the data which have not been explained previously will be presented here.

5.2 Mean and Variance Analysis

A conditional sampling algorithm was used during mean analysis and quadrant analysis to test for and exclude data that show a horizontal approach angle $> 75^\circ$ from the vertical centerplane of the probe coordinate system. The ratio of good to total data points in terms of approach angle (inclusion ratio), is included in the summary statistics (Tables 6.2 through 6.11). Note that of 50 data sets collected (counting each sensor individually), 37 (74%) indicate that 99% or more of the data in each of these runs is within the designated approach angle. Only 4 of the 50 (8%) show inclusion ratios less than .80. The acceptance angle used here (75°) is very conservative (Miller, et al., 1987) and could be increased to classify most of the currently discarded data as good. The conditioning technique used can be tested in a straightforward manner by running the mean and variance analyses on the data sets with the lowest inclusion ratio with all the data included in the analyses. The problem with this approach is that the data have been classed as 'bad' and excluded in the first place because they may not be physically meaningful due to instrument shadowing.

Recognizing this limitation, an inclusive mean analysis was conducted on the November 11, 1986 data (Table 6.10). The results show changes of around 20° in the mean directions. It is noted that some of the lowest inclusion ratios correspond to high values of turbulent intensity (Table 6.10) particularly in the unfoliated trunk-space data. The conditional sampling of the series with low inclusion ratios has some effect on series mean and variance but the differences between the conditioned and unconditioned series is typically less than 20% of the absolute value of the quantity.

Conditional sampling cannot be performed on series which are to be used for spectral or correlation analysis without replacement of the removed data with synthetic data in the series or truncation of the series at each excluded point. Therefore, these points are included in the series for spectral and correlation analysis and the inclusion ratio of each vector time series is given in the summary statistics.

Extensive mean and variance analysis has been performed on all of the data sets obtained between 8/25/86 and 11/23/86 which include at least three functioning TFWOES. As mentioned in Chapter 3, $\bar{w} = 0$ cannot be assumed at this site because of the edge and canopy inhomogeneities. At a level site with uniform roughness, data could be rotated to force $\bar{w} = 0$ to eliminate leveling errors. With this in mind and the physical interest in mean vertical motion at the site acknowledged, statistics have been calculated for the data with and without vertical rotation. In the vertically unrotated data, leveling error and actual vertical motion are incorporated in the calculated vertical component. In the vertically rotated data, both are removed. These two calculations, rotated and unrotated, are equivalent to calculating the fluxes ($u'w'$ and $w'T'$) perpendicular to a level ground surface and perpendicular to the streamlines (neglecting leveling error).

An initial rotation to force $\bar{v}' = 0$ was performed on all of the data. Then the mean, σ and turbulent intensity (TI) of the horizontal vector (in the u-v plane) were calculated. Also at this point, mean, σ , and TI are calculated for the w component as well as mean fluxes perpendicular to the surface.

The algorithms used in the mean and variance analyses are all based on standard formula. The mean analyses were combined with the quadrant analysis for programming convenience. All code discussed here was written by the author , as op-

posed to using packaged algorithms, which seemed less convenient for the task at hand. Variance algorithms were also written by the author. Two-dimensional rotations of the form

$$x' = x \cos \alpha + y \sin \alpha \quad (5.1a)$$

$$y' = -x \sin \alpha + y \cos \alpha \quad (5.1b)$$

were employed, where α is the angle of the mean vector with the vertical centerplane of the probe.

The mean horizontal angle (α) and angular σ can be calculated using the raw velocity component data as follows. If the system

$$\overline{\sin \theta} = \sum_{i=1}^N \frac{\sin \theta_i}{N} \quad (5.2a)$$

$$\overline{\cos \theta} = \sum_{i=1}^N \frac{\cos \theta_i}{N} \quad (5.2b)$$

is used, where θ is the instantaneous angle,

$$\theta = \tan^{-1} \left(\frac{v}{u} \right) \quad (5.3)$$

an average angle is obtained. If this angle is used in the coordinate rotation (Eqn. 5.1 a,b) as α , the desired rotation forcing \bar{y} to zero is not accomplished. The desired angle α is the angle of the resultant vector and is obtained using

$$\tan^{-1} \frac{\bar{v}}{\bar{u}} = \theta \quad (5.4)$$

then $\theta = \alpha$.

After the second rotation which rotates into the mean streamline in three dimensions, all the statistics are calculated again with the exception of the w statistics.

All of these data are presented in tabular form for each data set. Included in this summary are data from the Gills (the inclusion ratio for the Gill is always 1.). Data from the sonic anemometer mounted near the Gill is also presented, though it is limited to \bar{w} and vertical heat flux (H). Finally, an average screen height temperature for the run is included. This temperature was obtained from the second order station approximately 300m NW of the site.

The Gill data underwent special handling due to instrument specific cosine and frequency response. The cosine response algorithm is included as a subroutine in the statistical processing program. The algorithm used comes directly from Horst (1973). Gill frequency response is approximately 1 Hz. Since data were collected at either 5 or 20 Hz, an averaging routine was used to reduce the data to 1 Hz.

The data are presented and discussed relative to a coordinate system with origin $x,y=0,0$ on the ground surface 10m east (further into the forest) of the stationary tower where all vertical profiles were collected. The coordinate system is diagrammed with every sensor station used in this experiment shown with its coordinates in Figure 5. Coordinates are in meters from the origin.

5.3 Spectral Analysis

As pointed out previously, the autocorrelation and the spectra of a given series are mathematical transforms and as such contain similar information. In this study spectral analysis (analysis in the frequency domain) will be emphasized, though correlation analysis is used where it is required by convention or offers insight. Though spectral analysis is a fundamental tool in fluid dynamics, interpretation of this analysis can be difficult. Therefore, this technique is developed here analytically, leading to its statistical usage and interpretation. Also discussed are scaling and conditioning techniques used in this analysis.

Generally speaking, spectral analysis is used to decompose stationary, random series into sine and cosine functions. The amplitude of these functions represents series variance at the period of the function. Following Priestly (1981), any periodic function may be represented as a Fourier series

$$f(x) = \sum_{r=0}^{\infty} (a_r \cos(\frac{2\pi r x}{p}) + b_r \sin(\frac{2\pi r x}{p})) \quad (5.5)$$

Where x is displacement and p is the period of the function. This can also be expressed in terms of angular frequency (ω),

$$\omega = \frac{2\pi}{p} \quad (5.6)$$

To extend this idea to non-periodic functions, i.e. stochastic time series, it is necessary to regard non-periodic functions as periodic functions of infinite period. This allows Equation 5.5 to be written as

$$f(x) = \int_0^{\infty} g(\omega) \cos \omega x + k(\omega) \sin \omega x \, d\omega \quad (5.7)$$

This procedure is meaningless if

$$\int_{-\infty}^{\infty} |f(x)| \, dx = \infty \quad (5.8)$$

so Eqn. 5.8 is a limiting factor.

Otherwise, by introducing $p(\omega)$ as

$$p(\omega) = \begin{cases} 1/2\{g(\omega) - ik(\omega)\} & \omega > 0 \\ g(\omega) & \omega = 0 \\ 1/2\{g(|\omega|) + ik(|\omega|)\} & \omega < 0 \end{cases} \quad (5.9)$$

Eqn. 5.7 can be written as

$$f(x) = \int_{-\infty}^{\infty} p(\omega) e^{i\omega x} \, d\omega \quad (5.10)$$

utilizing an identity of the complex exponential. $p(\omega)$ is said to be the Fourier transform of $f(x)$.

Thus, the difference between periodic and non-periodic functions is that periodic functions can be expressed as a discrete set of frequencies while the description of non-periodic functions requires all frequencies. To generalize Eqn. 5.10 for these two cases, a function $P(\omega)$ is introduced so that

$$f(x) = \int_{-\infty}^{\infty} e^{i\omega x} dP(\omega) \quad (5.11)$$

In the non-periodic case

$$\frac{dP(\omega)}{d\omega} = p(\omega) \quad (5.12)$$

yielding Eqn. 5.10. In the periodic case

$$dP(\omega) = \begin{cases} A_r & \omega = \omega_r, r = 0, \pm 1, \pm 2, \dots \\ 0 & \text{otherwise} \end{cases} \quad (5.13)$$

leaving $f(x)$ non-zero at the discrete frequencies described by A_r . The introduction of $P(\omega)$ is known as a Fourier- Stieltjes transform. Based on the work of Wiener (cited in Priestly, 1981) this theory can be extended to non-deterministic, stochastic processes, such as a time series realization of a non-harmonic process, using

$$X(t) = \int_{-\infty}^{\infty} e^{it\omega} dZ(\omega) \quad (5.14)$$

here $Z(\omega)$ is a function of the same form as $P(\omega)$, but is not differentiable at every point. Thus, Eqn. 5.14 provides a formal analytical basis for the decomposition of a time series into sin and cosine functions. The amplitude of a given function,

$g(\omega)$ and $h(\omega)$ in Eqn. 5.7, is interpreted as the amount of variance at frequency ω .

Following Panofsky and Dutton (1984), the variance spectra of turbulence is computed using the autocorrelation function $R(\tau)$ (see Eqn. 1.8 and discussion). So

$$R(\tau) = E\{u'(t)u'(t + \tau)\} \quad (5.15)$$

if we assume or create a stationary series, then the Schwarz inequality

$$R(\tau) \leq \{E\{(u'(t))^2\}E\{(u'(t + \tau))^2\}\}^{1/2} = \sigma_u'^2 \quad (5.16)$$

relates $R(\tau)$ to $\sigma_u'^2$. Since $1/2 \sigma_u'^2$ is defined as the TKE of the flow, $R(\tau)$ is formally related to the energy of the flow. By a Fourier transform (see Eqn. 5.10)

$$\Phi(\omega) = \frac{1}{\pi} \int_{-\infty}^{\infty} R(\tau) e^{i\omega\tau} d\tau \quad (5.17)$$

with $\Phi(\omega)$ representing the distribution of TKE with ω . Utilizing the inverse Fourier transform

$$R(\tau) = 1/2 \int_{-\infty}^{\infty} \Phi(\omega) e^{-i\omega\tau} d\omega \quad (5.18)$$

and

$$R(0) = 1/2 \int_{-\infty}^{\infty} \Phi(\omega) d\omega \quad (5.19)$$

If $\tau = 0$ is tested in Eqn. 5.16 it can be seen that the rhs of Eqn. 5.19 represents the TKE of the flow.

Before discussing physical interpretation and computation of these quantities, it is necessary to formally present other related analyses which are used and are derived from or related to the spectral methods described previously. The first is phasing in a univariate series. A phase angle, (ϕ) , of the form

$$\phi = \tan^{-1} - \left(\frac{b_r}{a_r} \right) \quad (5.20)$$

can be calculated using the Fourier coefficients from Eqn. 5.5 (Jenkins and Watts, 1968). This angle can be computed for each harmonic but is of little use in this study because the angle is relative to the temporal origin which is arbitrary in the series under consideration here. Therefore, univariate phase analysis was conducted but is not used extensively in the data interpretation.

The remaining spectral analyses used are bivariate analyses associated with the cross-spectra of two series. The cross-spectral analysis can be decomposed to directly yield co-spectra, quadrature spectra, inter-series phase relationships and coherence. All of these diagnostic quantities are calculated in this study. Therefore, these methods are developed here with some formality following Panofsky and Dutton (1984).

The cross-spectra is developed in a manner similar to the univariate spectra with differences arising from the fact that the auto-covariance ($R_x(\tau)$) and the cross-covariance ($R_{xy}(\tau)$) functions are different in some fundamental respects. $R_x(\tau)$ is symmetric about $\tau = 0$ and therefore is an even function. Sin is an odd function

which integrates to zero over $\tau = -\infty$ to $\tau = \infty$. Thus Eqn. 5.17 may be written as the real integral

$$\Phi_x(\omega) = \frac{2}{\pi} \int_0^{\infty} R_x(\tau) \cos \omega \tau d\tau \quad (5.21)$$

Conversely, $R_{xy}(\tau)$ is not symmetric and the Fourier transform yields the complex integral

$$\Phi_{xy}(\omega) = \frac{1}{\pi} \int_{-\infty}^{\infty} R_{xy}(\tau) e^{i\omega\tau} d\tau \quad (5.22)$$

or

$$\Phi_{xy}(\omega) = C_{xy}(\omega) + iQ_{xy}(\omega) \quad (5.23)$$

where

$$C_{xy}(\omega) = \frac{1}{\pi} \int_{-\infty}^{\infty} R_{xy}(\tau) \cos \omega \tau d\tau \quad (5.24)$$

and

$$Q_{xy}(\omega) = \frac{1}{\pi} \int_{-\infty}^{\infty} R_{xy}(\tau) \sin \omega \tau d\tau \quad (5.25)$$

$C_{xy}(\omega)$ is the co-spectra and $Q_{xy}(\omega)$ the quadrature spectra of $\Phi_{xy}(\omega)$. Manipulating further, $\Theta(\omega)$ can be defined as

$$\Theta(\omega) = \tan^{-1} \frac{Q_{xy}(\omega)}{C_{xy}(\omega)} \quad (5.25)$$

and is called the bivariate phase angle.

The final quantity is the coherence, which is sometimes called the 'spectral correlation coefficient'. This statistic examines the behaviour of two series at a given ω without phase effects and is defined as

$$\Gamma_{xy}(\omega) = \frac{(C_{xy}(\omega) + Q_{xy}(\omega))^2}{\Phi_x(\omega)\Phi_y(\omega)} \quad (5.26)$$

If $x = y$, then $R_{xy}(\tau)$ is symmetric and $Q_{xy}(\omega) = 0$. This leaves

$$\Phi_x(\omega) = \Phi_y(\omega) = \sqrt{C_{xy}(\omega)} \quad (5.27)$$

so $\Gamma_{xy}(\omega) = 1$.

Still to be discussed is the computation of spectra made up of finite series of data evenly spaced in time and subsequently, the physical interpretation of the quantities described here. The former problem is one of numerical analysis. The Fast-Fourier transform (FFT) software used in these analyses was not written by the author, but is a much used FFT routine written at Pennsylvania State University in the middle 1960's and documented by Parhani (1971). The FORTRAN source code was obtained from the University of Nebraska and was loaded onto the 3090 IBM system at the University of Connecticut. Software was written to link the FFT output and system graphics packages.

The FFT was introduced in 1965 by Cooley and Tukey (as referenced in Priestly, 1981). The advantage of such an algorithm is the savings gained in computer time by reducing the number of calculations required. Following Priestly (1981) and Cooley et al., (1977), consider a series of N numbers represented by x_t , and the discrete finite Fourier transform

$$D(\omega_p) = \sum_{t=0}^{N-1} x_t e^{i\omega_p t} \quad p = 0, 1, \dots, N-1 \quad (5.28)$$

For each p , N operations are required to evaluate the sum. Therefore, to evaluate across all p , N^2 operations are required. To reduce the number of operations let

$$N = r \cdot s \quad (5.29)$$

where r and s are integers. Let

$$\begin{aligned} t &= 0, 1, \dots, N-1 \\ t &= rt_1 + t_0 \quad t_1 = 0, 1, \dots, r-1 \\ t_0 &= 0, 1, \dots, s-1 \end{aligned} \quad (5.30)$$

and

$$\begin{aligned} p &= 0, 1, \dots, N-1 \\ p &= sp_1 + p_0 \quad p_1 = 0, 1, \dots, r-1 \\ p_2 &= 0, 1, \dots, s-1 \end{aligned} \quad (5.31)$$

After some manipulation the discrete Fourier transform (Eqn. 5.28) is changed to a two stage summation. First

$$\sum_{t_1=0}^{s-1} x_{(rt_1 + t_0)} e^{2\pi i p t_1 / s} = a(p_0, t_0) \quad (5.32)$$

The reduction of this sum requires Ns operations since there are N values of $x(p_0, t_0)$ and the sum is carried out s times for each. Next,

$$D(\omega_p) = \sum_{t_0=0}^{s-1} a(p_0, t_0) e^{2\pi i p t_0 / N} \quad (5.33)$$

Eqn. 5.33 requires r operations at each N . This two step procedure therefore requires

$$Nr + Ns = N(r + s) \quad (5.34)$$

operations which is usually substantially less than r^2 operations. Further, if N can be expressed as

$$N = r_1 \cdot r_2 \cdot r_3 \dots r_p \quad (5.35)$$

where $r_1 \dots r_p$ are prime numbers, the number of operations lessens to $N(r_1 + r_2 + \dots + r_p)$ (Thomas et al., 1963 as cited in Cooley, et. al. 1977). The FFT algorithm used in these analyses requires that

$$N = 2^p \quad (5.36)$$

thus extending the idea of Eqn. 5.35 to its maximum and lowering the number of required operations to $O(N \log N)$.

Certain specific statistical manipulations were used on the data analyzed here. The first was the appending of zeroes to each realization of the data so that each realization fulfills the requirements of Eqn. 5.36. Appending zeroes to the data will not affect the numerical values of the spectral density estimates but it will affect the frequencies at which the transforms are evaluated (Priestly, 1981). The second conditioning technique used here is called tapering. Tapering is necessary because sharp discontinuities in a data set, such as occur at the end of a set or at the 'edge of the window' cause a rippling effect in the spectral estimates known as Gibbs effect. The classic example of this effect occurs when a square wave is constructed using sine and cosine functions. The solution to this type of bias is to taper a realization at its ends. The tapering used here is one quarter period of a cosine function which acts on 5% of the data set at each end of the series. The taper is simply a factor which varies from zero to 1. Data point N is multiplied by zero and the taper factor increases as a cosine function to data point $19N/20$ which is multiplied by one. The same tapering also occurs at the start of the realization (data points 1 to $N/20$). The final conditioning is performed on the spectral estimates themselves to convert them to spectral density. This is accomplished by dividing each of the estimates by the total variance yielding a normalized spectra, the integral of the area under the normalized spectra equals one. The spectra presented here are either three or four realization ensembles for the 20 Hz runs and nine realization ensembles for the 5 Hz runs. The 20 Hz realizations consist of 1999 data points each so 49 zero points are appended to yield 2048 (2^{11}) points for the FFT algorithm. The 5 Hz realizations consist of 1799 data points each so 249 zero points are appended to these series.

Spectra of turbulence were discussed at some length in Chapter 2 and the interpretation of this statistic should be clear. The cross spectral analysis can be sum-

marized as follows. The cross spectra is divided into real and complex parts corresponding to the co-spectra and quadrature spectra respectively. The co-spectra yields the 'in-phase' covariance between the coefficients of the two series. The quadrature spectra (as its name suggests) yields covariance between 'out-of-phase' coefficients. The shift is due to the 90° shift between the cosine and sine functions which define the quantities (Eqns. 5.24 and 5.25). The bivariate phase angle describes the phase angle between given harmonics of the two series. Phase spectra can then be drawn which describe the phase relationships at all frequencies. The coherence (Eqn. 5.26) acts as a correlation coefficient between series, but since it is calculated at a given ω , all phase information is lost. Thus, this statistic is removed from the relative time differences between series and correlates coefficients of given harmonics.

Scaling of the spectra of velocity components and temperature was performed using Eqn. 1.32 to obtain a length scale (L). Dimensionless frequency, f , is then

$$f = nL/\bar{u} \quad (5.37)$$

Four other methods were tested on the in-canopy and near-canopy spectra of u' from the profile data. The first was to substitute u_x for \bar{u} in Eqn. 5.37. The second was to multiply Eqn. 5.37 by the non-dimensional Eulerian to LaGrangian conversion factor , $.5/(\sigma_w/\bar{u})$ (Pasquill (1974) in Hanna et al., (1984)). Finally, a time determined from the autocorrelation of w (Baldocchi, personal communication, 1987) where

$$\tau_w = \tau \quad \text{when} \quad \rho(\tau) = 0 \quad (5.38)$$

where τ_w is the number of lags at which the autocorrelation of the w series ($\rho(\tau)$) is zero. The success or failure of these schemes is presented graphically and discussed in Chapter 6.

5.4 Quadrant Analysis

The next analysis to be discussed here is a quadrant analysis of Reynolds stress with a conditional magnitude filter. This filter which eliminates values in a series below a certain magnitude creates a hole on a quadrant plot of $u'w'$ and hence the name hole analysis. As described in Chapter 2, it is expected that anomalously large values of horizontal velocity ($+u'$) are associated with downdrafts ($-w$) and low values ($-u'$) are associated with updrafts ($+w$). An obvious way to verify this is to check if $-u'$ and $+w$ are associated at a given point in time. Since much of the series consists of small values of $u'w'$ which may be interpreted as 'noise' and are of little interest, a threshold value of $u'w'$ is chosen. Points with values below the threshold value are not considered. Points with values above the threshold are assigned a quadrant based on the signs of u' and w' in the $u'w'$ term. The quadrants are numbered by convention with quadrant 1 corresponding to $++$ and the quadrant numbers increasing counterclockwise around the graph of u' versus w' . The analysis is typically performed at different threshold values or hole sizes to see if the percentage of points in a given quadrant changes with hole size.

This procedure can be formalized following Shaw (1985). First the threshold value or 'hole' can be described as

$$H = u'w' / \overline{u'w'} \quad (5.39)$$

In the software written for these analyses, H is incremented by integer values. For instance, the series is first filtered at $H = 1$ or $u'w = \overline{u'w}$, then at $H = 2$, then 3, etc. typically up to $H = 40$. What is effectively created by this procedure is an intermittency function for large momentum events. Shaw defines a stress fraction $S_{i,H}$

$$S_{i,H} = \overline{u'w}^{-1} \lim_{T \rightarrow \infty} \frac{1}{T} \int_0^T u'w'(t) I_{i,H}(t) dt \quad (5.40)$$

and a time fraction $T_{i,H}$

$$T_{i,H} = \lim_{T \rightarrow \infty} \frac{1}{T} \int_0^T I_{i,H} t dt \quad (5.41)$$

so that $S_{i,H}$ describes the contribution to the stress from a given quadrant at a particular hole size and $T_{i,H}$ is the percentage of time the series met the specified hole and quadrant criteria. The intermittency function, $I_{i,H}$ has the form of a typical intermittency function

$$I_{i,H} = \begin{cases} 1, & \text{if } (u'w) \in Q_i \text{ and } |u'w| \geq H |\overline{u'w}| \\ 0, & \text{otherwise} \end{cases} \quad (5.42)$$

Notice that this method bypasses substantial information in the time domain. Though the fraction of time the series remains in a given quadrant after filtering is considered, the length and spacing of an individual 'strong' event is not considered. Also, all phase information is lost so that if two spatially separated series were compared, the relative time of occurrence of strong events in time is not apparent.

The obvious approach to this problem is to return to the original series in question. Events can be examined and filtering performed without losing the relative time information. This forms the basis for the next set of analyses which are being termed structure analyses.

5.5 Structure Analysis

The structure analysis techniques developed for this study were conceptualized based on empirical observations reported by Thompson (1979), Shaw et al., (1979) and others. The actual method is developed from work done by Chen and Blackwelder (1978) and Scholls (1985) (see Chapter 2). The purpose of this analysis is to isolate extreme events in the flow. Since such events may occur randomly, harmonic and correlation analysis will not describe them adequately. Once these events are defined and located, it is of interest to determine how important they are in transporting kinetic energy and scalar quantities in the flow. Also, the propagation of these structures in time and space and the interaction of these structures with the canopy can be investigated.

Initial attempts at isolating coherent structures or events were based on reports of ramp structures in time series of temperature (Thompson, 1979). The ramp structures consist of a slow rise in temperature followed by a sharp decline and may be associated with the transport of cold fluid by boundary layer scale eddies (see Chapter 2). A windowing technique to search for such structures in a time series is called variable interval time averaging (VITA). This technique was developed by Chen and Blackwelder (1978) for use in wind tunnels and used by Scholls (1985) in the PBL. The VITA of quantity $Q(t)$ is defined as:

$$Q(t) = \frac{1}{T_V} \int_{t-.5T_V}^{t+.5T_V} Q(t) dt \quad (5.43)$$

The localized VITA variance of Q is:

$$(\text{var}(t)) = (Q^2) - (Q)^2 \quad (5.44)$$

A detection function may be stated as:

$$D(t) = \begin{cases} 1 & \text{if } (\text{var}(t)) > K_V Q'^2, \quad \frac{(dQ)}{dt} < 0 \\ 0 & \text{otherwise} \end{cases} \quad (5.45)$$

where K_V is a threshold value which is used to calibrate the technique and Q' is defined as:

$$Q' = \left(\lim_{T \rightarrow \infty} (\text{var}(t)) \right)^{\frac{1}{2}} \quad (5.46)$$

$Q(t)$ is a moving average, if $Q(t)$ changes abruptly as indicated by $\text{var}(t)$, then the digital detection function $D(t)$ is set to one. Using this method, long time series can be scanned to detect rapid changes in the series mean. The requirement of change in a specified direction can be adjusted, using K_V , based on physical requirements. After an event meeting the threshold criteria is found, it can be compared to a simultaneous series of a different quantity. For example, an 'injection' of momentum into the canopy should be accompanied by a decrease in temperature.

A modified version of these ideas was applied to the temperature series. The technique used a change in temperature (ΔT), if ΔT exceeded a specified threshold value (K_V) within a specified time, t , T would be flagged. The program then printed

the flagged value of T (T_f) along with a specified length of the series around T_f and the corresponding velocity series. These two pieces of the realization are then inspected to see if, indeed, sharp temperature drops are accompanied by velocity increases. This technique did not yield the expected results. Strong ΔT s were not always accompanied by structures in the velocity series. In the limited usage given this technique, the two series near T_f never showed the clear relationship expected. This initial approach lacked generality. The VITA technique was originally developed in a wind tunnel where the thermal structure of the boundary layer is created. In the PBL, where a large range of Richardson numbers can be experienced (including local stability variations within the canopy) the usefulness of this approach is limited. In near neutral conditions, dT/dz is small ($d\theta/dz \approx 0$) so fluid transported a long vertical distance will not show a large ΔT in the series.

Based on the results of this first attempt, a more direct approach to finding large or coherent momentum transfer events was chosen. Momentum information is available in the quadrant analysis. Each point is sorted by quadrant and by size. Therefore, it was decided that since this information was already being compiled, it was a straightforward task to retain the relative time information. Thus, series of $u'w'$ were produced where, if H is 'hole size' and Q is a specified quadrant

$$x(t) = \begin{cases} u'w' & \text{if } (|u'w(t)| > H \text{ and } Q(t) = Q) \\ 0 & \text{otherwise} \end{cases} \quad (5.47)$$

where t is the position in the original series and $Q(t)$ is the quadrant (given by the signs of u' and w , at that position). This equation basically combines Eqns. 5.39 and 5.40 to create a series of large momentum events separated by zeros. By varying H , it was hoped the 'correct' filter size could be determined. This value would leave discrete blocks of large $u'w'$ and eliminate intervening noise. Another approach was

to go back to Eqn. 5.40 and plot the intermittency function ($I_{i,H}$) with respect to time. This technique was varied so that $I(t)$ was given three states

$$I(t) = \begin{cases} 1 & \text{if } |u'w(t)| > H \text{ and } Q(t) = Q_4 \\ -1 & \text{if } |u'w(t)| > H \text{ and } Q(t) = Q_2 \\ 0 & \text{otherwise} \end{cases} \quad (5.48)$$

thus creating a time series showing three states of momentum transfer. At each position t , $I(t)$ can be 1 representing a large injection of momentum, -1 representing a large ejection or 0 representing the interactive quadrants and time when the threshold value of H was not exceeded.

The purpose of reducing the series of momentum to three states was to yield a clear graphical representation of strong momentum transfer events in the series. The representation yielded by Eqn. 5.42, however, did not reduce the series to blocks of large momentum transfer with intervening zeros as hoped. Instead, the series remained dominated by short bursts in Q_4 or Q_2 interspersed with zeros so the overall effect was a noisy series, even though it was apparent that during given intervals Q_4 was more important, followed by intervals where Q_2 was more important.

The final step in this process is to smooth or filter the series so regions where a given quadrant is obviously dominant become discrete, coherent sections of the series. It was hoped this could be done simply by varying H but this approach did not yield a clearer representation of momentum events. An intricate neighborhood algorithm was written that arbitrarily decides the beginning and end of these events based on the surrounding series. This algorithm was unwieldy and was eventually simplified so that only events that remain in a given quadrant and meet the hole size

criteria for a continuous specified length of time are included. The parameters that give the best graphic representation are 5 seconds and $H = 1$.

5.6 Determination of Stability

Stability is estimated for each of the long runs using $w'T'$ and $u'w'$ at the 24m Gill and T from the Stevenson screen. The algorithm used is from Panofsky and Dutton (1984) where L is defined as

$$L = - \frac{u_*^3 c_p \rho T}{k_a g H (1 + .07/B)} \quad (5.49)$$

here this is reduced to

$$L = - \frac{u'w'^{3/2} T}{k_a g w'T' (1 + .07/B)} \quad (5.50)$$

where B is the Bowen ratio (the ratio of sensible to latent heat flux). Since LE (latent heat flux) is not available in this study, a range of values, based on other researchers (Anderson, et. al. 1986, Denmead and Bradley, 1985) is tested. Over the foliated canopy B is set at .25 and 1. Over the unfoliated canopy 1. and 2. are used. The ratio $-(z-d)/L$ is then calculated with d initially set at the level of maximum LAI. This method over estimated d in the unfoliated canopy, so a profile estimation (Rosenberg, 1979) was performed to estimate d . The two methods yield similar results in the foliated canopy ($d = 11$). The lower value of d calculated by the profile method ($d = 4$) is used for the unfoliated canopy. Dolman (1986) found similar values for d/h in a shorter, foliated canopy, though his unfoliated values of d/h fall between the two values calculated here. Two values of $-z/L$ are presented for each

long run (based on two values of B). Though the values of $-z/L$ can vary up to 20% across the specified range of B , the calculated stabilities agree qualitatively with observations made in the run log.

5.7 Correlation Analysis

Correlation analysis is performed to investigate spatial relationships and to obtain specific integral scales used in scaling spectra. Standard correlation algorithms are used in this analysis (Haan, 1977) for both auto and cross-correlations. The correlation statistics were run block by block to avoid problems with inter-block gaps. Multiple blocks are examined for a given data set to ascertain the variance in the results. Spatial cross-correlations were performed on vector velocities between sensors. Since the sensor spacing precludes high frequency correlation due to the small spatial scales which cause high frequency fluctuations, the cross-correlations are run on smoothed series. Based on an average wind speed of 5 ms^{-1} and a maximum sensor spacing of 21 m, a 4 or 6 second block average is performed on the series before the cross-correlation analysis is performed. Auto-correlations are run on 1 Hz data at all sensors, since this is the frequency response of the Gill.

5.8 Determination of Drag Coefficients

Profiles of local drag coefficients were calculated using the formulation of Shaw (1987). Based on the formulation of shear stress as

$$\tau = \rho C_D \bar{u}^2 \quad (5.51)$$

a local drag coefficient can then be formulated as

$$C_D = \left(\frac{u_*}{u} \right)^2 \quad (5.52)$$

which is easily calculated from the available data. It should be noted that the quantity described in Eq 5.52 might be more appropriately termed a surface friction coefficient, especially in-canopy.

5.9 Dispersion Statistics

Since an immediate application of this research is in transport and dispersion of gasses and particulates in the canopy, dispersion statistics are calculated for the low frequency data sets. The statistics used are from Hanna (1984). As an indicator of vertical dispersion

$$D_V = \frac{\sigma_w}{u_*} \quad (5.53)$$

is calculated. As an indicator of longitudinal dispersion

$$D_L = \frac{\sigma_u}{u_*} \quad (5.54)$$

is used. To compare between data sets the values of D_V and D_L presented are normalized by the values of these variables at the Gill.

5.10 Determination of Canopy Density

Finally, the last method that requires discussion is the determination of canopy density at the site. The sampling technique used and the algorithm employed to yield LAI are described in Wang and Miller (1987). This is a photographic method using hemispherical photographs at different heights to determine LAI above a given height. This allows a profile of LAI to be constructed. The lens utilized (Nikkon 16mm f2.8 150°) produces an equiangular projection which is overlain by a grid with intergrid area a constant proportion of projected area across the grid. The photographs were quantified based on the percentage of grid nodes covered by dark (foliage) or light (sky) in the photograph. These percentages are then entered into an algorithm which has been calibrated with respect to leaf inclination and azimuth angle at this site using the data of Miller and Lin (1985). This algorithm yields LAI for a foliated canopy.

Due to photographic problems, LAI for the foliated canopy was taken directly from Miller and Lin (1985) and is based on a point drop approach. The photographic method was used in the unfoliated canopy but the azimuthal density function ($g(\theta)$) was changed. Since canopy stems and branches are not expected to show strong heliotropism as sun leaves do, $g(\theta)$ was changed from an empirically determined distribution to an uniform distribution with respect to height.

Photographs were taken at 1 or 2 m intervals between $y=0$ and $y=h$ at $x=21$ and were also taken at $x,y = 43,0$ and $10,0$. Due to the low value of stem area in the unfoliated canopy (typically $.7 \leq SAI \leq 1.4$ above $z=0$) there is a large percentage variation in SAI between profiles measured on different days but profile shape is relatively constant. An average profile has been calculated for use in this discussion.

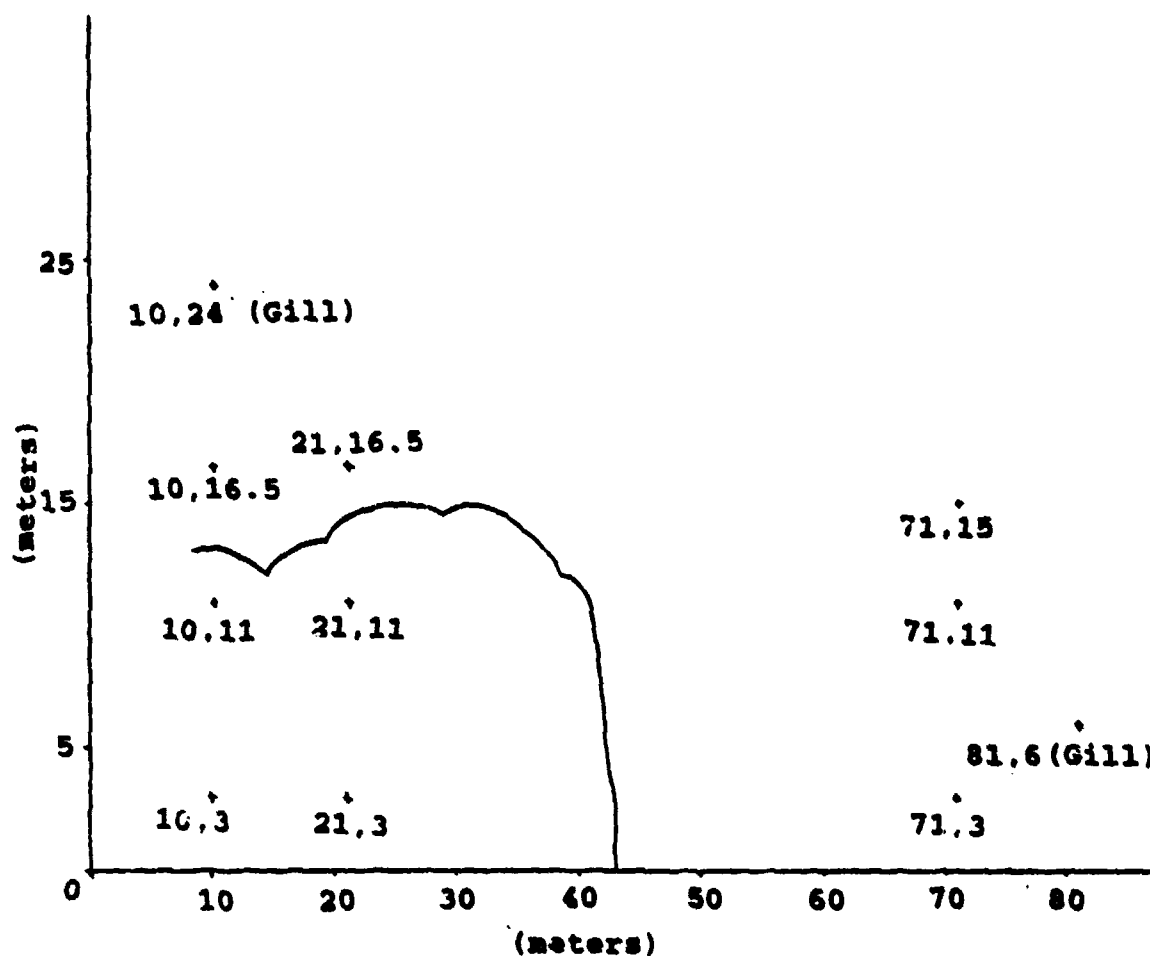


Fig. 5 The coordinate system used in the data discussion has origin 0,0 10m east of the stationary tower where the vertical profiles were collected. Sensor positions are shown with x,y coordinates. Points not designated otherwise are TFWORS stations. The solid line is an outline of the canopy cross-section.

Chapter VI

Results and Discussion

The focus of the results chapter is on the comparison of the edge canopy flows in the foliated and the unfoliated states. First, velocity profiles in the canopy in foliated and unfoliated conditions with forest and edge fetch flows will be compared, with discussion focused on mean profiles. Subsequently, the horizontal transects will be used to construct two dimensional contour plots of the mean edge flow. Quadrant analysis, spectral analysis and structure analysis is then used to gain information on length scales and flow structure in the canopy.

The most difficult part of this analysis is the formulation of composite results. The flow statistics will in some respect be influenced by \bar{u} , σ_u , TI, $-z/L$, wind direction and LAI. To isolate the effects of changes in LAI and the edge is, therefore, difficult due to inhomogeneities in the foliage, terrain complexities and the vagaries of the synoptic scale flow, all of which combine to make each run a unique situation. However, certain conclusions can be made and others can be speculated upon.

6.2 Stability

Stabilities calculated from the low frequency runs are presented in Table 6.1. Of the 10 low frequency runs examined, seven are near neutral, one is classed as neutral, one is classed as near neutral but is stable and one is strongly unstable (see classification scheme of Anderson, et. al., 1986). The relative homogeneity of stabilities over the course of these experiments aids inter-run comparison of the data.

6.3 Mean Statistics in Vertical Profiles

The mean statistics and the quadrant analyses for one hour runs are presented in tabular form (Tables 6.2 - 6.11). The first page of each table (Table A) contains primarily mean information for the specified run. Columns 1,2 and 3 are average vertical velocity (\bar{w}), average horizontal velocity (\bar{u}_H) and average total velocity (\bar{u}_{To}) respectively. Columns 4 and 5 are horizontally rotated $\bar{u}\bar{w}_H$ and $\bar{u}\bar{w}_I$ after a three dimensional rotation. Columns 6 and 7 are $\bar{w}\bar{T}$ after a two dimensional rotation and after a three dimensional rotation $\bar{w}\bar{T}_I$ respectively. Column 8 is the inclusion ratio (see Chapter 5). The second page of each table is composed of variance statistics for each run. Columns 1 and 2 are mean direction \angle and standard deviation σ°_\angle of direction respectively. Directions are given as the \angle from due north. Column 3 is standard deviation of temperature (σ_T). Columns 4 and 5 are standard deviation (σ_w) and turbulent intensity (TI_w) of the vertical component of velocity. Columns 6 and 7 are standard deviation (σ_{uH}) and turbulent intensity (TI_{uH}) of the horizontal (into the mean wind) velocity component and Columns 8 and 9 are standard deviation ($\sigma_{u_{TOT}}$) and turbulent intensity $TI_{u_{TOT}}$ of the total vec-

tor. The third page of each table is a rough summary of the quadrant analyses. Two representative hole sizes were chosen for each run (usually $H = 1$ and either $H = 10$ or $H = 20$ as designated on the table itself). The first four columns are labeled by quadrant and the fraction of the total remaining that falls in that quadrant is listed. The fifth column contains the total points remaining at the specified hole size. The second five columns contain the same information for the larger hole size. Note that due to the instrument frequency response, the total points remaining for the Gill anemometers will typically be less than those remaining for the wires because they begin with fewer points.

The mean profiles from foliated and unfoliated edge fetch flows show some striking differences. The comparison of normalized \bar{u}_{TOT} in the foliated and unfoliated canopies exhibits differences caused by changes in canopy density and changes in the relative distribution of canopy elements (Figure 6). The normalized gradient is $|\Delta \bar{u}_N / \Delta z|$ (this differential will subsequently be designated as S_1) where $\bar{u}_N = \bar{u}_{TOT}$ normalized by \bar{u}_{TOT} at 24m. S_1 is much larger above $z/h = 1$ in the normalized foliated profile (Figure 7) than in the normalized unfoliated profile. S_1 becomes much smaller between 1.1 and .7 h in the normalized profile but remains constant from .7 to 1.7 h in the normalized unfoliated profile. These differences are due to increased LAI in the foliated profile. The increase in leaf area (A in Eq 2.22) increases drag in the foliated canopy. Also, Figure 6 shows very low stem area index (SAI) above 11m ($\approx .8h$) in the unfoliated profile. The unfoliated \bar{u}_{TOT} profile reflects this as S_1 shows no change at the $h = 1.1$ level.

Below h , both profiles show secondary maxima in \bar{u}_{TOT} . Thus, the profiles have similar shape beneath h , though normalized values of \bar{u}_{TOT} are larger in the unfoliated profile. Since this profile is $< 3h$ from the forest edge, the secondary maxima

in these profiles is a result of blowthrough (longitudinal transport of momentum from the edge through the relatively low density trunk space). These profiles demonstrate the influence of the canopy on the flow and are intuitively quite reasonable.

Local canopy drag coefficients (Figure 8) agree with those measured by Shaw (1987) at an unfoliated canopy top at similar stabilities (Table 6.1). Shaw reports values between .07 and .14 for C_D . It is interesting to compare figures 6.1 and 6.3. Though C_D shows little change between the foliated and unfoliated edge fetch profiles, in both cases the shape of the profile of C_D appears to be controlled by the shape of the profile of LAI indicating some dependence on LAI. Grant (1984) indicates that C_D is not strongly dependent on the density of individual elements but does increase abruptly as the mean flow increases above 1.5 ms^{-1} . Thus, C_D is not responding to increased LAI but to increased \bar{u}_{tot} . It should be noted that Grant studied individual spruce shoots, but these ideas may partly explain the shape of these C_D profiles.

Comparison of foliated and unfoliated edge fetch profiles of TI (Figure 9) are higher in the foliated data above the canopy, but values of $TI_{\bar{u}_{\text{TOT}}}$ are much higher below h in the unfoliated canopy (Table 6.10B). In the unfoliated canopy, the $TI_{\bar{u}_{\text{TOT}}}$ maximum occurs around .7h. In the foliated canopy, the $TI_{\bar{u}_{\text{TOT}}}$ maximum occurs around 1.1h. The $TI_{\bar{u}_{\text{TOT}}}$ minimum occurs above canopy in both cases.

Seginer et al. (1981) presents profiles of $TI_{\bar{u}_{\text{TOT}}}$ for a model canopy in a wind tunnel. His values of $TI_{\bar{u}}$ are near .5 in the 'canopy'. These values are lower than most of those measured in this study but the shape of the profile of $TI_{\bar{u}}$ given by Seginer roughly corresponds to the shape of the unfoliated profile in Fig. 9 in the

canopy. Baldocchi et al. (1987) presents in-canopy values of $TI_{\bar{u}}$ in an almond orchard with $h=8\text{m}$ and LAI near 1.3. In this canopy, the absolute values of $TI_{\bar{u}}$ agree within 5% with those measured in the unfoliated canopy at Coventry (Table 6.10B). Baldocchi measured $TI_{\bar{u}}$ at $.14h$ and $.51h$ which are slightly different than the normalized measurement heights used in Coventry. However, the general trend of slightly increasing $TI_{\bar{u}}$ from the trunk space upward toward the level of maximum LAI is demonstrated by the data of Baldocchi and the unfoliated data collected by this author (Fig. 9). It is interesting that these measurements in very different low density canopies agree so well. This is an indication that the sensors perform quite well in flows of high turbulent intensity.

Forest fetch profiles of velocity are used, by comparison, to edge fetch profiles to determine the role of the edge in these flows. In the foliated forest fetch profile of \bar{u}_{TOT} there is no evident secondary maximum in the velocity profile, indicating edge influence in this phenomena (Figure 10). Also, normalized \bar{u}_{TOT} is smaller at every level in the forest fetch run. This again points to the role of the edge which allows longitudinal momentum transport through the low density trunk space to the in-canopy sensors in edge fetch flows.

Profiles of $TI_{\bar{u}_{TOT}}$ in foliated east versus west flows indicate that the $TI_{\bar{u}_{TOT}}$ maximum shifts from near the canopy top in the edge fetch flow to the trunk space in the forest fetch flow (Tables 6.2B and 6.3B, respectively). This indicates that the edge causes increased turbulence in the canopy roughness sublayer (Finnigan, 1985) in edge fetch flows. The profiles of C_D in foliated edge and forest fetch flows indicate that C_D in these flows is highest in the trunk space of both profiles and larger in the foliated canopy. It is apparent that generalizations regarding in-canopy C_D are difficult. The value of this coefficient changes as a function of obstacle shape

(leaf versus trunk) as well as with \bar{u}_{TOT} . The value of C_D seen in Figure 12 at the canopy top in the unfoliated profile is less than values reported by Shaw (1987) under similar circumstances.

The normalized dispersion statistics, D_w and D_L , (described in Eqns. 5.53 and 5.54) are examined in edge and forest fetch foliated and unfoliated profiles. The vertical profile of normalized D_w shows a maximum in the trunk space with edge fetch (Figure 13) in both the foliated and unfoliated profiles. In the forest fetch profiles of D_w , (Figure 14) the unfoliated profile is bimodal with maxima in the trunk space and near h . The foliated profile of D_w here shows a maximum near h . The profiles of D_L with edge fetch wind indicate that maximum D_L occurs in the unfoliated trunk space but near the level of maximum LAI in the foliated canopy (Figure 15). The forest fetch profiles of D_L (Figure 16) indicate a maximum in the unfoliated profile near h . Notice that in Figures 13 to 16, normalized values of D_L and D_w are larger in the unfoliated canopies. This is because D_L and D_w at $1.8h$ are larger in the foliated canopy, indicating that dispersive influences are displaced upwards by the foliated canopy.

The horizontal transects can be used to investigate conclusions drawn from the vertical profiles. To do this, normalized values of \bar{u}_{TOT} , $TI_{\bar{u}_{TOT}}$, D_w and D_L are taken from each run and composite contour plots are created. These plots are used to obtain a general feeling for the spatial distribution of these variables and as a rough way of examining the influence of the edge in two dimensions. The contour plots were drawn by hand and the outline of the two dimensional canopy cross-section was overlain after the contours were drawn so that the canopy outline would not effect the positioning of contours.

The contour plot of normalized \bar{u}_{TOT} across the foliated edge (Figure 17) is generally shaped as would be expected with a secondary maximum in \bar{u}_{TOT} under the canopy due to longitudinal momentum transport through the trunk space from the edge. A bulge in the horizontal variation in \bar{u}_{TOT} near h in the lee of the edge may be due to the shape of the upper canopy surface. A similar plot of normalized \bar{u}_{TOT} in the unfoliated canopy (Figure 18) indicates that the unfoliated in-canopy flow is less regular than the air flow in the foliated canopy. This is supported by the unfoliated profiles of $TI_{\bar{u}_{TOT}}$ and the dispersion statistics and is an interesting result.

The contour plot of $TI_{\bar{u}_{TOT}}$ in the foliated canopy with edge fetch (Figure 19) shows a shape similar to Figure 17 though the contours are displaced upward. This plot indicates that $TI_{\bar{u}_{TOT}}$ is largest in this plot in the trunk space and in the roughness sublayer. The unfoliated contour plot of $TI_{\bar{u}_{TOT}}$ (Figure 20) shows increasing values with increasing distance into the canopy. The normalized values are larger in the unfoliated canopy than in the foliated one because the disruption of the flow at the Gill is less over the foliated canopy.

Finally, contour plots of D_w and D_L in foliated and unfoliated canopies with edge fetch winds are examined. In the foliated canopy, D_w appears to be increasing with z in front of the edge and is high in the trunk space (Figure 21). In the unfoliated case, this plot shows a strong maximum near h over $2h$ east of the edge (Figure 22). These plots are difficult to interpret though they may indicate strong eddying in front of the foliated canopy and above the unfoliated. The contour plot of D_L in the foliated canopy (Figure 23) shows D_L increasing with z west of the edge and increasing with distance into the canopy. D_L in the unfoliated canopy shows only slight variation across the array (Figure 24).

Certain conclusions can be drawn from the analysis to this point. Increased LAI does cause increased momentum loss through increased drag. This result is expected and it is clearly demonstrated by the mean velocity data. The second conclusion that can be drawn from the mean velocity data is also intuitively appealing. This is the measurement of strong secondary maxima in the velocity profiles in the trunk space. This secondary maximum is evidence of longitudinal transport of horizontal momentum from the edge and may be enhanced by constriction of the flow due to the canopy. This strong secondary maximum is seen in the unfoliated edge fetch profile but is not apparent in the forest fetch profile indicating the edge is the major contributing factor to this phenomena. Turbulent intensity ($TI_{\bar{u}_{TOT}}$) shows some definite patterns in the profiles. $TI_{\bar{u}_{TOT}}$ is always lowest at 24m in the profile at IS in both foliated and unfoliated flows. Generally, $TI_{\bar{u}_{TOT}}$ is highest in the unfoliated canopy. The indication that flow in the unfoliated canopy is more turbulent and less regular than that in the foliated canopy is quite interesting.

6.5 Quadrant Analysis of Data

Quadrant analysis was performed using Eqs 5.41 and 5.42. Comparison of the quadrant analyses for the edge fetch foliated and unfoliated profiles (Tables 6.2C and 6.10C respectively) shows a definite trend. In the foliated profile, the out of canopy stations show much stronger concentration of points in quadrants 2 and 4. In the unfoliated profile, this trend is not clear with quadrants 2 and 4 being weakly dominate everywhere. This may well be a result of the increased disruption of the flow caused by increased LAI. It was anticipated that quadrants 2 and 4 might be more dominant in canopy due to filtering of the weaker, 'diffusive' motions in quadrants 1 and 3. This does not appear to be true. The forest fetch foliated and un-

foliated profiles (Tables 6.3C and 6.11C, respectively) only weakly support the previous contention. In the foliated profile, quadrant 2 and 4 are strongly dominant at all levels except 16.5m. In the unfoliated profile, quadrants 2 and 4 are strongly dominant except at the 3m level. The discrepancy here indicates that at high LAI, the edge is a longitudinal source of momentum which confuses the in canopy hole analysis. The unexpected distribution by quadrant of $u'w'$ at 16.5m in the forest fetch foliated profile may be due to local variation in the 'surface' formed by the canopy top (variation in h). At 3m in the unfoliated profile, $TI_{\bar{u}_{TOT}}$ is > 1 indicating a confused flow situation.

The horizontal transects may be used to investigate conclusions made using profile data. The foliated horizontal transect at 16.5m (Table 6.3C) shows quadrants 2 and 4 dominant everywhere. This is expected since all sensors are out of canopy in this run. The unfoliated horizontal transect at 16.5m (Table 6.8C) shows strong dominance by quadrants 2 and 4 at $x,y = (71,16.5), (21,16.5)$, and $(10,24)$. At 10,16.5m, quadrants 2 and 4 do not dominate in these data. The foliated transect at 11m (Table 6.5C) again shows quadrants 2 and 4 dominant at all sensors including the two in canopy. This does not fit with previous conclusions but is attributable to the very low values of \bar{u}_{TOT} during this run. In cases of low \bar{u}_{TOT} there is little longitudinal energy penetrating the edge, therefore the only source of momentum is above the canopy and this is demonstrated by the quadrant analysis. The unfoliated transect at 11m (Table 6.9C) shows quadrant 2 and 4 dominant everywhere. The unfoliated transect at 3m (Table 6.6C) shows quadrants 2 and 4 strongly dominant everywhere except at 10,3 which agrees with previous observations. This anomalous quadrant distribution at 10,3 again corresponds to high $TI_{\bar{u}_{TOT}}$ at this station. Baldocchi et al. (1986) reports that the time fractions are similar between quadrants, even at large hole sizes in the almond orchard data.

However, he indicates that 64% of the total stress occurs at $H > 30$ at .14h but he does not divide this stress fraction by quadrant. Baldocchi attributes the lack of difference between quadrants in his in-canopy data to 'sloshing' of air near the canopy floor or wake eddies behind trees.

Certain general conclusions can be drawn from the quadrant analyses. First, it is quite clear that vertical momentum transport is the source of large variations in \bar{u} outside the canopy, in the upper unfoliated canopy and sometimes in the foliated canopy. Secondly, the role of injection/ejection is less dominating in the unfoliated trunk space during flows of high $TI_{\bar{u}_{TOT}}$. Thirdly, the role of injection/ ejection at 1.1h is occasionally confused in both foliated and unfoliated flows, which may be due to local variations in h. Finally, the role of injection/ejection near the edge may be a function of \bar{u}_{TOT} since at high velocities, especially under foliated conditions, momentum may be transported longitudinally through the trunk space. Thus, horizontal advection of momentum through the trunk space becomes important, + u' becomes less dependent on $-w'$, and quadrants other than 2 and 4 become important. The same reasoning may explain the anomalous quadrant analyses seen in the unfoliated trunk space since maximum LAI is lowered to 9m in the unfoliated canopy. However, it is surprising that this effect is so strong with such low LAI and the effect is also observed in a forest fetch run.

6.6 Correlation Analysis

Cross-correlation analysis was performed on series of longitudinal velocity between sensors on foliated and unfoliated, forest and edge fetch profiles as well as

some horizontal transects. Spatial correlations along the horizontal transect generally decrease with distance. It is expected that

$$\tau_\rho = \cos \theta L_s \quad [6.1]$$

where τ_ρ is the lag at which maximum $\rho(\tau)$ occurs, θ is the horizontal angle between the transect axis and the mean wind vector and L_s is sensor separation. This expectation is not fulfilled in most cases. Also, though some indication is given that spatial $\rho(\tau)$ decreases less rapidly in the unfoliated canopy, conclusions are difficult to draw due to the extreme variability of $\rho(\tau)$ between blocks in a given data set and the low absolute values of $\rho(\tau)$ exhibited by many of these data. This confirms the suggestions of Panofsky and Dutton (1985, Chap. 5) that spectral analysis is more useful than correlation analysis in the atmosphere. Spatial correlations along the profiles gave similar results with low values of $\rho(\tau)$ and lengths that do not systematically correspond to L_s (note that θ in Eqn. 6.1 becomes a vertical angle in the case of vertical profiles, thus τ_ρ would be expected to be relatively small in these cases).

Auto-correlations were performed on series of w' because it is thought that the integral scale (Chap. 2) of w' would shorten closer to the surface, thus this quantity could be used to scale spectra at different heights. These lengths do not decrease systematically towards the surface through the canopy so this method was not used.

6.7 Scaling of Spectra

Scaling of spectra for general discussion is performed as discussed in Chapter 5, with the method chosen primarily to facilitate comparison of results with other researchers (Anderson, et. al. 1986). However, it appears from the overlays of in-

canopy spectra that scaling by Eqn. 5.37 with u_* replacing \bar{u} also collapses the in and near-canopy spectra reasonably well (Figures 25 and 26). Use of the Eulerian-Lagrangian conversion was not particularly successful in collapsing the in and near-canopy spectra of u' , but this might be anticipated since the instruments are in a fixed array which is a Eulerian system with respect to the flow. Finally, scaling by τ_w (Eqn. 5.38) was not successful due to the unusual behaviour of this statistic at different levels in the canopy as discussed.

6.8 Comparison of Foliated and Unfoliated Spectra

Spectra of u' are compared to ascertain the effect of the foliage and of the edge. Spectra of v', w' and T' from the vertical profiles are also examined to detect the effects of foliage density on these spectra. Multiple length scales are present at this site due to the effects of the edge, foliage, topography and the PBL. An attempt is made to associate regions of production in the spectra with these length scales. This is done using the relationship between vortice length and \bar{u}_{TOT} (the Strouhal number describes this relationship, see Hinze, 1975) and examining individual features in unscaled spectra.

Comparison of spectra of u' from the foliated profile (Figure 29) and the unfoliated profile (Figure 30) yields interesting results. \bar{u}_{TOT} at the various levels are relatively close between the two sets. The foliated spectra of u' at 16.5m shows increased $S(f)$ around .04 Hz (unscaled) which corresponds to a length of 40m at this \bar{u}_{TOT} . This feature is not seen in the unfoliated spectra at this level. Above this frequency unfoliated and foliated data show inertial subranges and the high frequency runs indicate production at high frequencies in the canopy (Figures 31 and

32). In the foliated spectra at this level, the inertial subrange continues to where $|b|$ becomes less steep indicating high frequency production beginning at length scales of .85m. In the unfoliated spectra, the inertial subrange ends at a frequency corresponding to a length of .48m.

The differences at the high frequency end of these data are probably due to the fact that leaves and foliated branches shed longer vortices than twigs and that the LAI maximum is lower in the unfoliated data. The production with length scales around 40m in the foliated data is probably caused by the edge shedding vortices when it is foliated that are not present when it is less dense or 'memory' in the flow of terrain induced eddies.

The foliated in canopy (11m) spectra show maxima corresponding to length scales of 25.5m and 7.8m in the spectra of u' , the high frequency spectra of u' at this level show regions of constant $S(f)$ which represent length scales around .4 and .18 m. The u' spectra at 11m in the unfoliated canopy shows production corresponding to a length scale of 19m. The high frequency u' spectra at this level shows production corresponding to length scales of .28 and .16m respectively. The longer length scales in both runs may be due to 'memory' of topographic influence but it is interesting that the middle range length is not present in the unfoliated data. This length (7.8m) is probably due to the edge and clumps of foliage. At high frequencies, the indicated lengths are remarkably similar but the nature of the spectra are different. The lengths indicated by the foliated u' spectra at high frequency represent broad areas of production, possibly representing the dynamic projection area of, and confused vortical shedding by, foliated branches. In the high frequency unfoliated spectra, these lengths maybe manifested as discrete spikes representing eddy shedding from cylindrical branches.

The trunk space spectra (3m) of u' in the foliated canopy show large amounts of energy at high frequencies corresponding to lengths around 7.6m. The high frequency u' spectra at this level show $|b| > 5/3$ at high frequencies agreeing with the low frequency spectra and extending the production lengths to .2m. The trunk space u' spectra shows increased production corresponding to a length scale of 18m. The high frequency spectra here shows production at lengths shorter than .4m. This comparison indicates that there is high frequency production at many scales in the foliated trunk space. The unfoliated trunk space shows fewer lengths, with production at lengths shorter than .4m, probably representing the unfoliated canopy elements (trunks, etc.).

Initial conclusions are:

- 1) In canopy spectra show high frequency production due to eddy shedding by canopy elements.
- 2) Foliated spectra show a broader range of length scales compared to unfoliated spectra which tend to show production in narrower frequency bands.
- 3) These in canopy spectra show production at intermediate lengths that may be due to terrain or edge vortices.

The horizontal transects are used to attempt to verify some of these conclusions. In Figure 33 ,the u' spectra at 10,24 shows production at lengths of about 44m surrounded by regions of $b = -5/3$ slope. At 10,16.5m in this run, the spectra of u' shows a long inertial subrange. The high frequency run shows some production at high frequencies at this level which corresponds to a length scale of .42m. High frequency spectra from the foliated run at 71,15 show no high frequency production, as expected. Comparison of spectra at 71,15 and 10,16.5 in Figure 34 indicates the

role of the foliage at high frequency, note that the difference in \bar{u}_{TOT} at the two stations is $< .2 \text{ ms}^{-1}$.

The foliated transect at 11m shows a u' spectra at 10,24 which shows slight production around 185m (Figure 35). The spectra of u' at 10,11 in this data set shows some production around .48m which may be caused by folding of frequencies caused by tower sway. The high frequency spectra (Figure 36) at this level shows marked production at a length around .09m. The spectra from the 11m unfoliated transect (Figures 37 and 38) are remarkably similar, especially at high frequencies, indicating that high frequency turbulent production by the canopy is above the highest calculated frequency here.

The horizontal transect at 3m in the unfoliated canopy (Figure 6.34) is examined. The spectra of u' at 10,24 shows minor production corresponding to a length scale of 96m. The spectra of u' in the trunk space (10,3) during this run shows a short inertial subrange interrupted by production corresponding to a length scale of 21m, production also occurs around 11.4 and 4.9m. The high frequency spectra here (Figure 6.35) shows production at 1.5 and .75m and some production at higher frequencies. The shape of these spectra attests to the confused nature of the flow at this level.

These in canopy spectra exhibit extensive inertial subranges in many cases. It is true that due to varying wind speed and direction, production ranges are 'smeared' and the region of $-5/3$ slope may be disrupted by ensembling but it is not correct to say that this subrange is not present in this canopy. Table 6.12 and Table 6.13 summarize some of the production scales indicated in the data. It is realized that the estimation of length here is crude and that indicated $S(f)$ above 0 Hz may be

enhanced due to folding or diminished due to underestimation. (These effects may extend to lower frequencies, especially in the lower frequency data, see Tanatichat and George, 1984). The spectra of w show less energy at low frequency as expected (Figures 6.36 and 6.37). These spectra indicate that the shape of the w spectra is influenced by height with more high frequency energy apparent closer to the surface. Spectra of v' in the vertical profiles also show more high frequency energy than do spectra of u' . (Figures 6.40 and 6.41). The scaling of w' and v' spectra by \bar{u} is approximate in this study. The spectra of temperature are much smoother than the spectra of the velocity components. This is probably a result of the fact that almost all of these runs were obtained under near neutral conditions in well mixed boundary layers. Thus T' does not show regions of high frequency production (Figures 6.38 and 6.39). Finally, production is indicated at length scales between 25 and 50m in many of the spectra, both in and outside the canopy. At higher frequencies, production is indicated at around .4m in the foliated (and some unfoliated) in canopy spectra. All in canopy spectra show some production at lengths shorter than .4m while the out of canopy spectra do not show this high frequency production.

The hypothesis that u' and w' should be out of phase is not demonstrated by these data. The hypothesis was tested by plotting the value of the maximum coherence between u' and w' versus the phase angle (not distinguishing between + and - angles) at the frequency where the coherence maximum occurs. Most of the data sets show maximum coherence at the lowest calculated frequency, which indicates that u' and w' are better correlated at low frequencies. Since phase information is lost in calculating coherence (Chapter 5), the plot of coherence maximum vs. phase angle would demonstrate systematic phasing between these two variables if any existed. It seems reasonable that as the value of the coherence maximum increased, the phase angle would approach 180° . This was not seen in these data

and informal results of Baldocchi (personal communication, 1987) also fail to show this relationship.

Comparison of spectral data with previous research is difficult due to experimental differences, canopy variation and the unique nature of the research. Anderson et. al. (1986) made measurements over a foliated deciduous forest, scaling frequency with $(z-d)/\bar{u}$. The results of this study show the inertial subrange of the spectra centered around $f = .4$ Hz. In Anderson's experiments, the sensor was at 1.3h. Studies over more homogenous surfaces, such as water (Miyake, et. al., 1970) and grain (Kaimal, et. al., 1972) show inertial subranges in the u' spectra centered near $f = 1$. Panofsky et. al. (1982) presents longitudinal spectra in neutral conditions both downwind of water and on a hilltop. These spectra agree more closely with those of Anderson. Only Anderson corrected z with d .

The absence of λ_{\max} in the results presented here makes comparison with the aforementioned studies difficult. However, though the position of the inertial subrange in this study varies, it appears that it is generally shifted to slightly lower frequencies than those previously mentioned. Much of the variation among spectra in this study may be a result of the scaling used. The meaning of, and therefore the specification of d in a canopy with an important horizontal momentum source is not clear.

6.9 Structure Analysis

The structure analysis demonstrates the complex nature of momentum transfer events and the disorderly propagation of these events in time and space. As described in Chap. 5, partitioning the series of $u'w'$ into different quadrants, filtering

by hole size and reducing the remaining series to 0, -1, 1 (Eqn. 5.42) leaves simplified, but still noisy and complicated time series. Since varying hole size did not substantially simplify the series, the hole size filter was held constant at $H = 1$ and a further condition was added to the algorithm. The final filter leaves only groups of points that remain in the same quadrant at $H \geq 1$ for a specified length of time termed the 'gap'. After examination of many series, the most effective gap length appears to be 5 seconds (Fig 47). This filtering procedure then leaves discrete events to focus upon when comparing series of $u'w'$ at different locations. This method may be limited in this study by the length of sampling blocks, since a given block may not show a major momentum event and the investigation of the spatial and temporal propagation of these events is impeded by the inter-block gaps. Despite these qualifications, this analysis can yield information. Figures 48 and 49 demonstrate that events can sometimes be followed through the canopy using this technique. At $z = 3$ in the trunk space in these figures, no points meet the $\text{gap} = 25$ criteria but a relatively strong region of $u'w'$ in quadrant 4 is seen in the graph with $\text{gap} = 0$. This indicates that these events are 'breaking-up' as they pass through the canopy. The figures from the foliated transect are more representative of the data with all three plots showing points meeting the criteria, but the temporal relationship between plots is not clear (Figure 50). This problem was anticipated by the low inter-sensor correlations in these data.

The figures from the unfoliated transect share no clear temporal relationship between the momentum events at the individual sensors (Figure 51 and 52). There appears to be agreement from the two sensors closest to the edge ($x = 21$, $x = 71$) but no corresponding event at $x = 10$.

Table 6.1.A Description of Foliated Data Sets

Date	Fetch	Array	-z/L	Stability	Comments
8/25/86	edge	vertical profile	.01	neutral	partly cloudy
9/4/86	forest	vertical profile	-.12--.14	near neutral	cloudy damp
9/11/86	edge	horizontal transect 16.5m	-.04--.05	near neutral	cloudy
9/22/86	edge	horizontal transect 11m	.08-.10	near neutral (stable)	cloudy

Table 6.1.B Description of Unfoliated Data Sets

Date	Fetch	Array	-z/L	Stability	Comments
10/18/86	edge	horizontal transect 3m	-.13	near neutral	partly cloudy
10/20/86	edge	horizontal transect 11m	-2.49	strongly unstable	clear
10/22/86	edge	horizontal transect 16.5m	-.04	near neutral	clear
10/29/86	edge	horizontal transect 11m	-.06	near neutral	clear
11/18/86	edge	vertical profile	-.16	near neutral	cloudy
11/23/86	forest	vertical profile	-.03	near neutral	partly cloudy

Table 6.2.A Mean Statistics of One-hour, 5Hz Run 8/25/86. See text for explanation of symbols. Screen height temperature was 21°C during this run.

Sensor Position (x,y)	\bar{w}	\bar{u}_H	\bar{u}_{TOT}	$\overline{u'w'}_H$	$\overline{u'w'}_I$	$\overline{w'T'}_H$	$\overline{w'T'}_I$	Inclusion Ratio
10,24	.74	5.41	5.46	-.13	-.46	.04	.01	
10,16.5	.57	1.47	1.57	-.13	-.32	-.02	-.11	.99
10,11	-.16	1.01	1.02	.01	.02	-.01	-.01	.99
10,3	.78	1.30	1.52	.21	.05	-.06	-.02	.73
81,6	.06	3.20	3.20	-.38	-.41			
10,24 Sonic	.45					-.05		

Table 6.2.B Variance and Directional Statistics of One-hour, 5Hz Run 8/25/86.

See text for explanation of symbols.

Sensor Position (x,y)	\angle	$\sigma^\circ \angle$	σ_T	σ_w	TI_w	$\sigma_{\bar{u}_H}$	$TI_{\bar{u}_H}$	$\sigma_{\bar{u}_{TOT}}$	$TI_{\bar{u}_{TOT}}$
10,24	235.7	37.4	.36	.84	1.14	1.79	.33	1.77	.32
10,16.5	287.6	19.2	.74	.58	1.02	1.01	.69	.92	.58
10,11	268.5	14.7	.53	.34	2.19	.42	.42	.41	.41
10,3	203.2	23.0	.74	.57	.68	.69	.51	.82	.51
81,6	234.1	51.8		.65	9.89	1.44	.45	1.43	.45

Table 6.2.C Quadrant Analysis of One-hour, 5Hz Run 8/25/86. Columns are labeled with quadrant numbers.

Sensor Position (x,y)	H = 1					H = 10				
	Q1	Q2	Q3	Q4	Total Points	Q1	Q2	Q3	Q4	Total Points
10,24	.17	.33	.16	.33	1861	.10	.53	.02	.36	114
10,16.5	.09	.41	.05	.45	6218	.06	.00	.01	.92	417
10,11	.30	.19	.34	.17	12662	.62	.05	.00	.33	1380
10,3	.31	.23	.30	.17	8135	.40	.01	.39	.19	764
81,6	.13	.38	.09	.40	1400	.02	.22	.00	.76	63

Table 6.3.A Mean Statistics of One-hour, 5Hz Run 9/4/86. See text for explanation of symbols. Screen height temperature was 18°C during this run.

Sensor Position (x,y)	\bar{w}	\bar{u}_H	\bar{u}_{TOT}	$\overline{u'w'_H}$	$\overline{u'w'_I}$	$\overline{w'T'_H}$	$\overline{w'T'_I}$	Inclusion Ratio
10,24	.04	3.56	3.56	-.10	-.10	-.02	-.02	
10,16.5	.11	.77	.77	-.08	-.04	.05	.06	.99
10,11	.00	.47	.47	.00	.00	.00	.00	1.00
10,3	.07	.40	.41	-.02	-.02	-.01	-.01	1.00
81,6	-.06	.89	.90	-.13	-.11			
10,24	-.08					-.01		
Sonic								

Table 6.3.B Variance and Directional Statistics of One-hour, 5Hz Run 9/4/86. See text for explanation of symbols.

Sensor Position (x,y)	\angle	σ°_L	σ_T	σ_w	TI_w	$\sigma_{\bar{u}_H}$	$TI_{\bar{u}_H}$	$\sigma_{\bar{u}_{TOT}}$	$TI_{\bar{u}_{TOT}}$
10,24	141.2	2.3	.21	.50	13.9	.70	.20	.70	.20
10,16.5	109.0	27.0	.46	.49	4.53	.21	.28	.16	.21
10,11	108.3	17.6	.31	.14	85.82	.13	.27	.13	.27
10,3	97.5	14.8	.28	.19	2.85	.19	.47	.17	.41
81,6	53.7	60.9		.47	7.60	.66	.74	.67	.75

Table 6.3.C Quadrant Analysis of One-hour, 5Hz Run 9/4/86. Columns are labeled with quadrant numbers.

Sensor Position (x,y)	H = 1					H = 10				
	Q1	Q2	Q3	Q4	Total Points	Q1	Q2	Q3	Q4	Total Points
10,24	.18	.36	.12	.33	1969	.20	.16	.03	.60	123
10,16.5	.04	.55	.01	.40	7822	.38	.31	.19	.12	26
10,11	.13	.34	.15	.38	10223	.15	.00	.00	.85	557
10,3	.02	.49	.03	.46	7393	.08	.00	.00	.92	12
81,6	.17	.32	.13	.38	1594	.03	.05	.01	.90	73

Table 6.4.A Mean Statistics of One-hour, 5Hz Run 9/11/86. See text for explanation of symbols. Screen height temperature was 25°C during this run.

Sensor Position (x,y)	\bar{w}	\bar{u}_H	\bar{u}_{TOT}	$\overline{u'w'}_H$	$\overline{u'w'}_l$	$\overline{w'T'}_H$	$\overline{w'T'}_l$	Inclusion Ratio
10,24	.26	3.62	3.63	-.53	-.73	-.14	-.15	
71,15	-2.08	3.99	4.50	-.88	-.16	-.07	.01	1.00
21,16.5	.21	1.60	1.61	-.28	-.32	-.02	-.02	1.00
10,16.5	-1.27	2.80	3.08	-1.32	-.53	-.21	-.06	.99
81,6	.16	3.40	3.40	-.25	-.32			
10,24 Sonic	.19					-.10		

Table 6.4.B Variance and Directional Statistics of One-hour, 5Hz Run 9/11/86.

See text for explanation of symbols.

Sensor Position (x,y)	\angle	σ_{\angle}	σ_T	σ_w	TI_w	$\sigma_{\bar{u}_H}$	$TI_{\bar{u}_H}$	$\sigma_{\bar{u}_{TOT}}$	$TI_{\bar{u}_{TOT}}$
10,24	330.2	22.6	.81	1.02	3.89	1.96	.54	1.94	.53
71,15	291.5	16.6	.46	1.10	.53	1.43	.36	1.61	.36
21,16.5	295.9	21.0	.83	.74	3.60	.96	.60	.92	.57
10,16.5	288.5	21.9	.73	1.26	1.00	1.59	.57	1.84	.60
81,6	352.7	15.3		.67	4.07	1.44	.42	1.42	.42

Table 6.4.C Quadrant Analysis of One-hour, 5Hz Run 9/11/86. Columns are labeled with quadrant numbers.

Sensor Position (x,y)	H = 1					H = 10				
	Q1	Q2	Q3	Q4	Total Points	Q1	Q2	Q3	Q4	Total Points
10,24	.17	.36	.12	.36	1869	.04	.04	.00	.92	53
71,15	.14	.19	.31	.35	14080	.30	.31	.03	.36	2474
21,16.5	.09	.42	.14	.36	7706	.06	.00	.00	.94	372
10,16.5	.14	.33	.11	.41	9833	.29	.05	.00	.66	285
81,6	.15	.40	.13	.33	1593	.05	.21	.06	.68	101

Table 6.5.A Mean Statistics of One-hour, 5Hz Run 9/22/86. See text for explanation of symbols. Screen height temperature was 15.5°C during this run. Station designated by 't' shows inconsistent data possibly indicating instrument malfunction.

Sensor Position (x,y)	\bar{w}	\bar{u}_H	\bar{u}_{TOT}	$\overline{u'w'_H}$	$\overline{u'w'_I}$	$\overline{w'T'_H}$	$\overline{w'T'_I}$	Inclusion Ratio
10,24	.03	1.85	1.85	-.19	-.20	.05	.04	
71,11t	-1.10	1.89	2.19	-.46	-.10	-.26	-.01	.93
21,11	.14	.48	.50	-.08	-.08	-.01	-.02	1.00
10,11	-.21	.44	.48	-.02	-.02	-.01	.00	.92
81,6	.13	1.69	1.69	-.06	-.10			
10,24 Sonic	-.02					.01		

Table 6.5.B Variance and Directional Statistics of One-hour, 5Hz Run 9/22/86.

See text for explanation of symbols.

Sensor Position (x,y)	\angle	$\sigma^\circ \angle$	σ_T	σ_w	TI_w	$\sigma_{\bar{u}_H}$	$TI_{\bar{u}_H}$	$\sigma_{\bar{u}_{TOT}}$	$TI_{\bar{u}_{TOT}}$
10,24	347.0	21.3	.80	.59	19.56	1.11	.60	1.10	.60
71,11	284.3	20.4	.99	.70	.69	.96	.55	1.14	.56
21,11	278.1	19.0	.51	.29	2.12	.36	.76	.30	.60
10,11	294.9	24.9	.45	.24	1.17	.24	.59	.28	.61
81,6	351.4	11.0		.36	2.70	.84	.50	.84	.49

Table 6.5.C Quadrant Analysis of One-hour, 5Hz Run 9/22/86. Columns are labeled with quadrant numbers.

Sensor Position (x,y)	H = 1					H = 10				
	Q1	Q2	Q3	Q4	Total Points	Q1	Q2	Q3	Q4	Total Points
10,24	.16	.35	.13	.37	1898	.22	.24	.01	.54	102
71,11	.10	.32	.16	.43	8570	.35	.46	.00	.20	468
21,11	.07	.00	.00	.93	2428	.00	.00	.00	1.00	385
10,11	.12	.38	.18	.32	10021	.27	.00	.00	.73	431
81,6	.13	.45	.11	.31	1336	.05	.09	.06	.80	107

Table 6.6.A Mean Statistics of One-hour, 5Hz Run 10/18/86. See text for explanation of symbols. Screen height temperature was 11.0°C during this run. Station marked with 't' shows inconsistent data and may be influenced by instrument malfunction.

Sensor Position (x,y)	\bar{w}	\bar{u}_H	\bar{u}_{TOT}	$\overline{u'w'_H}$	$\overline{u'w'_I}$	$\overline{w'T'_H}$	$\overline{w'T'_I}$	Inclusion Ratio
10,24	.33	3.82	3.84	-.10	-.28	-.10	-.07	
71,3t	-1.75	3.74	4.12	-.63	-.35	-.15	-.13	1.00
21,3	.26	1.25	1.28	.00	-.03	-.04	-.04	1.00
10,3	-.12	1.70	1.71	.06	.10	-.08	-.08	.87
81,6	.30	3.46	3.48	.02	-.11			
10,24 Sonic	.14							

Table 6.6.B Variance and Directional Statistics of One-hour, 5Hz Run 10/18/86.

See text for explanation of symbols.

Sensor Position (x,y)	\angle	σ_{\angle}	σ_T	σ_w	TI_w	$\sigma_{\bar{u}_H}$	$TI_{\bar{u}_H}$	$\sigma_{\bar{u}_{TOT}}$	$TI_{\bar{u}_{TOT}}$
10,24	217.1	25.0	.88	.82	2.49	1.65	.43	1.64	.43
71,3	261.6	14.1	.76	1.12	.64	1.18	.32	1.37	.33
21,3	295.3	17.3	1.18	.22	.82	.44	.36	.44	.34
10,3	317.9	26.2	.71	.36	3.12	.81	.50	.92	.62
81,6	208.1	20.7		.47	1.54	1.29	.37	1.28	.37

Table 6.6.C Quadrant Analysis of One-hour, 5Hz Run 10/18/86. Columns are labeled with quadrant numbers.

Sensor Position (x,y)	H = 1					H = 10				
	Q1	Q2	Q3	Q4	Total Points	Q1	Q2	Q3	Q4	Total Points
10,24	.22	.32	.17	.30	2229	.08	.46	.17	.29	217
71,3	.17	.28	.23	.33	11770	.13	.15	.00	.72	540
21,3	.11	.46	.13	.30	8267	.03	.00	.17	.80	431
10,3	.31	.18	.38	.13	8332	.32	.00	.38	.29	217
81,6	.20	.34	.16	.30	2043	.14	.35	.22	.29	281

Table 6.7.A Mean Statistics of One-hour, 5Hz Run 10/20/86. See text for explanation of symbols. Screen height temperature was 18.0°C during this run.

Sensor Position (x,y)	\bar{w}	\bar{u}_H	\bar{u}_{TOT}	$\overline{u'w'}_H$	$\overline{u'w'}_I$	$\overline{w'T'}_H$	$\overline{w'T'}_I$	Inclusion Ratio
10,24	.21	2.47	2.48	-.01	-.04	-.06	-.07	.99
71,11	-.91	2.65	2.80	-.27	-.20	-.05	-.04	
21,11	.35	.90	.96	-.01	-.02	.00	-.02	
10,11	-.47	1.15	1.24	-.07	-.06	-.08	-.05	
81,6	.24	2.11	2.12	.01	-.04			
10,24 Sonic	.00							.86

Table 6.7.B Variance and Directional Statistics of One-hour, 5Hz Run 10/20/86.

See text for explanation of symbols.

Sensor Position (x,y)	\angle	σ°_{\angle}	σ_T	σ_w	TI_w	$\sigma_{\bar{u}_H}$	$TI_{\bar{u}_H}$	$\sigma_{\bar{u}_{TOT}}$	$TI_{\bar{u}_{TOT}}$
10,24	292.9	52.1	.37	.45	2.09	.73	.30	.73	.30
71,11	289.7	15.2	.43	.75	.84	.80	.31	.91	.33
21,11	291.4	19.7	.55	.11	.32	.24	.27	.22	.22
10,11	294.3	28.6	1.02	.46	1.22	.44	.41	.60	.56
81,6	300.5	48.1		.29	1.20	.74	.35	.74	.35

Table 6.7.C Quadrant Analysis of One-hour, 5Hz Run 10/20/86. Columns are labeled with quadrant numbers.

Sensor Position (x,y)	H = 1					H = 10				
	Q1	Q2	Q3	Q4	Total Points	Q1	Q2	Q3	Q4	Total Points
10,24	.24	.29	.23	.25	2806	.15	.37	.23	.26	647
71,11	.16	.34	.14	.36	9099	.01	.13	.00	.86	319
21,11	.00	.44	.04	.51	4500	.00	.00	.02	.98	324
10,11	.13	.31	.20	.37	7160	.08	.49	.00	.43	286
81,6	.20	.35	.09	.37	1716	.13	.26	.20	.41	206

Table 6.8.A Mean Statistics of One-hour, 5Hz Run 10/22/86. See text for explanation of symbols. Screen height temperature was 19.0°C during this run.

Sensor Position (x,y)	\bar{w}	\bar{u}_H	\bar{u}_{TOT}	$\overline{u'w'_H}$	$\overline{u'w'_I}$	$\overline{w'T'_H}$	$\overline{w'T'_I}$	Inclusion Ratio
10,24	.42	3.54	3.56	.04	-.68	-.13	-.08	.86
71,15	-.45	2.70	2.74	-.54	-.42	-.07	-.07	
21,16.5	.21	2.00	2.01	-.09	-.14	-.10	-.11	
10,16.5	-.07	2.55	2.55	-.10	-.09	-.22	-.22	
81,6	.00	2.13	2.13	.08	.08			
10,24 Sonic	.09							.78

Table 6.8.B Variance and Directional Statistics of One-hour, 5Hz Run 10/22/86.

See text for explanation of symbols.

Sensor Position (x,y)	\angle	σ_{\angle}°	σ_T	σ_w	TI_w	$\sigma_{\bar{u}_H}$	$TI_{\bar{u}_H}$	$\sigma_{\bar{u}_{TOT}}$	$TI_{\bar{u}_{TOT}}$
10,24	237.5	78.1	.71	.64	1.51	2.55	.72	2.53	.71
71,15	270.1	35.2	1.31	1.01	3.28	1.42	.60	1.47	.62
21,16.5	305.2	9.3	.52	.46	2.17	.84	.42	.83	.41
10,16.5	314.8	29.9	1.23	1.03	19.10	1.36	.61	1.49	.75
81,6	281.7	76.1		.43		1.26	.59	1.26	.59

Table 6.8.C Quadrant Analysis of One-hour, 5Hz Run 10/22/86. Columns are labeled with quadrant numbers.

H = 1						H = 10				
Sensor Position (x,y)	Q1	Q2	Q3	Q4	Total Points	Q1	Q2	Q3	Q4	Total Points
10,24	.11	.37	.20	.32	1758	.00	.01	.00	.99	74
71,15	.16	.41	.10	.34	6835	.06	.78	.00	.16	273
21,16.5	.25	.42	.02	.32	8518	.25	.00	.00	.75	610
10,16.5	.26	.29	.22	.23	12164	.31	.15	.17	.38	4310
81,6	.26	.21	.31	.22	2617	.38	.17	.23	.22	444

Table 6.9.A Mean Statistics of One-hour, 5Hz Run 10/29/86. See text for explanation of symbols. Screen height temperature was 20.0°C during this run. The station marked with 't' shows inconsistent data and may be influenced by instrument malfunction.

Sensor Position (x,y)	\bar{w}	\bar{u}_H	\bar{u}_{TOT}	$\overline{u'w'}_H$	$\overline{u'w'}_I$	$\overline{w'T'}_H$	$\overline{w'T'}_I$	Inclusion Ratio
10,24	.32	4.74	4.75	-.65	-.80	-.16	-.18	
71,11t	-2.36	4.47	5.05	-1.08	-.28	-.21	-.05	1.00
21,11	-.55	2.48	2.54	-.86	-.61	-.04	-.01	1.00
10,11	-.87	1.90	2.09	-.37	-.11	-.12	-.12	1.00
81,6	.36	4.26	4.27	-.11	-.26			
10,24	.28							
Sonic								

Table 6.9.B Variance and Directional Statistics of One-hour, 5Hz Run 10/29/86.

See text for explanation of symbols.

Sensor Position (x,y)	\angle	$\sigma^\circ \angle$	σ_T	σ_w	TI_w	$\sigma_{\bar{u}_H}$	$TI_{\bar{u}_H}$	$\sigma_{\bar{u}_{TOT}}$	$TI_{\bar{u}_{TOT}}$
10,24	319.6	19.8	.42	1.15	3.60	1.92	.41	1.90	.40
71,11	291.2	16.2	.35	1.22	.52	1.52	.34	1.75	.35
21,11	313.8	15.1	.54	.84	1.53	1.23	.50	1.35	.53
10,11	292.5	18.6	.46	.72	.83	.93	.49	1.04	.50
81,6	327.6	12.4		.67	1.86	1.50	.35	1.49	.35

Table 6.9.C Quadrant Analysis of One-hour, 511z Run 10/29/86. Columns are labeled with quadrant numbers.

Sensor Position (x,y)	H = 1					H = 10				
	Q1	Q2	Q3	Q4	Total Points	Q1	Q2	Q3	Q4	Total Points
10,24	.16	.35	.14	.36	1871	.09	.42	.00	.49	45
71,11	.14	.23	.26	.37	12886	.32	.40	.01	.27	1359
21,11	.04	.42	.01	.54	10860	.02	.00	.00	.98	90
10,11	.12	.26	.30	.33	12623	.31	.21	.01	.47	1060
81,6	.18	.35	.15	.31	1973	.11	.37	.06	.46	134

Table 6.10.A Mean Statistics of One-hour, 5Hz Run 11/18/86. See text for explanation of symbols. Screen height temperature was 9.0°C during this run.

Sensor Position (x,y)	\bar{w}	\bar{u}_H	\bar{u}_{TOT}	$\overline{u'w'_H}$	$\overline{u'w'_I}$	$\overline{w'T'_H}$	$\overline{w'T'_I}$	Inclusion Ratio
10,24	.58	3.93	3.97	.11	-.07	.04	-.01	
10,16.5	-.43	2.32	2.36	-.73	-.68	.09	.10	.80
10,11	-.41	1.25	1.32	-.12	-.14	.08	.13	.57
10,3	1.07	1.44	1.80	.35	-.01	.14	-.04	.38
81,6	-.02	3.41	3.41	-.01	.00			
10,24 Sonic	.26					-.02		

Table 6.10.B Variance and Directional Statistics of One-hour, 5Hz Run 11/18/86.

See text for explanation of symbols.

Sensor Position (x,y)	\angle	$\sigma^\circ \angle$	σ_T	σ_w	TI_w	$\sigma_{\bar{u}_H}$	$TI_{\bar{u}_H}$	$\sigma_{\bar{u}_{TOT}}$	$TI_{\bar{u}_{TOT}}$
10,24	230.5	16.0	.42	1.15	3.60	1.92	.41	1.90	.40
10,16.5	247.9	35.7	.97	1.15	8.30	1.11	.55	1.16	.57
10,11	294.5	38.1	1.91	.59	3.80	.63	.76	.71	1.00
10,3	338.2	37.1	.94	.71	.88	.86	.90	1.08	.86
81,6	231.6	28.0		.41	25.10	1.17	.34	1.17	.34

Table 6.10.C Quadrant Analysis of One-hour, 5Hz Run 11/18/86. Columns are labeled with quadrant numbers.

H = 1						H = 10				
Sensor Position (x,y)	Q1	Q2	Q3	Q4	Total Points	Q1	Q2	Q3	Q4	Total Points
10,24	.25	.25	.25	.25	2813	.24	.31	.22	.22	978
10,16.5	.04	.48	.01	.47	5129	.00	.04	.00	.96	27
10,11	.16	.42	.03	.39	4569	.29	.18	.00	.54	28
10,5	.26	.27	.23	.24	6194	.25	.22	.25	.28	3367
81,6	.21	.26	.26	.27	3418	.22	.25	.26	.27	2568

Table 6.11.A. Mean Statistics of One-hour, 5Hz Run 11/23/86. See text for explanation of symbols. Screen height temperature was 10.0 °C during this run.

Sensor Position (x,y)	\bar{w}	\bar{u}_H	\bar{u}_{TOT}	$\overline{u'w'_H}$	$\overline{u'w'_I}$	$\overline{w'T'_H}$	$\overline{w'T'_I}$	Inclusion Ratio
10,24	.26	9.82	9.83	-.74	-1.04	-.10	-.11	
10,16.5	.27	2.55	2.56	.07	-.10	-.06	-.05	.80
10,11	-.29	1.36	1.39	-.11	-.12	.01	.03	.87
10,3	.61	2.06	2.14	-1.00	-.31	.26	.28	.88
81,6	-1.25	2.42	2.72	-.45	-.40			
10,24 Sonic	.02					-.06		

Table 6.11.B Variance and Directional Statistics of One-hour, 5Hz Run 11/23/86.

See text for explanation of symbols.

Sensor Position (x,y)	\angle	σ°_{\angle}	σ_T	σ_w	TI_w	$\sigma_{\bar{u}_H}$	$TI_{\bar{u}_H}$	$\sigma_{\bar{u}_{TOT}}$	$TI_{\bar{u}_{TOT}}$
10,24	105.7	56.9	.94	.96	3.65	3.54	.36	3.53	.36
10,16.5	72.1	39.6	1.23	1.23	4.16	1.91	.95	1.90	.94
10,11	79.2	29.2	1.32	.63	2.64	.68	.57	.75	.62
10,3	110.8	37.7	.71	2.36	4.22	2.06	1.14	1.98	1.05
81,6	163.8	30.7		1.43	1.14	1.29	.54	1.45	.53

Table 6.11.C Quadrant Analysis of One-hour, 5Hz Run 11/23/86. Columns are labeled with quadrant numbers.

Sensor Position (x,y)	H = 1					H = 10				
	Q1	Q2	Q3	Q4	Total Points	Q1	Q2	Q3	Q4	Total Points
10,24	.20	.33	.14	.33	2003	.02	.17	.01	.80	129
10,16.5	.32	.20	.29	.19	12254	.11	.37	.00	.52	827
10,11	.19	.32	.20	.28	9102	.03	.00	.00	.97	39
10,3	.24	.28	.20	.28	10699	.53	.00	.00	.47	3367
81,6	.24	.33	.16	.27	2097	.18	.03	.07	.73	228

Table 6.12 Production Lengths Indicated by Longitudinal Velocity Spectra In Edge Fetch Winds

Sensor Position (x,y)	Foliated	Length Scales (m)	-z/L	Stability
10,16.5	y	40, .85	.01	neutral
10, 16.5	n	.48	-.12	near neutral
10,11	y	25.5, 7.8, .4, .18	.01	neutral
10,11	n	19, .28, .16	-.12	near neutral
10,3	y	> .2, 7.6	.01	neutral
10,3	n	18, .4	-.12	near neutral
10,24	y	44	-.04	near neutral
10,16.5	y	.4	-.04	near neutral
10,24	y	185	.09	near neutral (stable)
10,11	y	.48, .09	.09	near neutral (stable)
71,11	y	27	.09	near neutral (stable)
10,24	n	96	-.10	near neutral
10,3	n	21, 11.4, 4.9, 1.5, .75	-.10	near neutral

Table 6.13 Speculated Sources of Production Shown in Table 6.12

Sensor Position (x,y)	Foliated	PBL (m)	Terrain (m)	Edge (m)	Inter- Tree (m)	Foliage (m)
10,16.5	y	185	40			.85
10, 16.5	n					.48
10,11	y			25.5	7.8	.4,.18
10,11	n			19		.28,.16
10,3	y				7.6	.2
10,3	n			18		.4
10,24	y		44			
10,16.5	y					.4
10,24	y					.09
10,11	y					.48,.09
71,11	y			27		.09
10,24	n		96			
10,3	n			21,11.4	4.9	1.5,.75

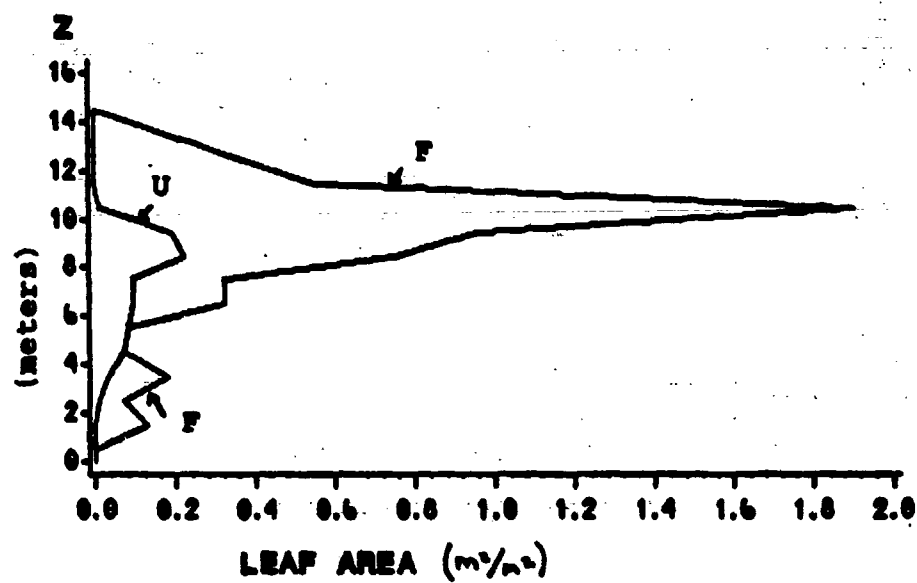


Fig. 6 The distribution of leaf area with height in the foliated (F) and unfoliated canopy (U). The profiles are at $x=21$.

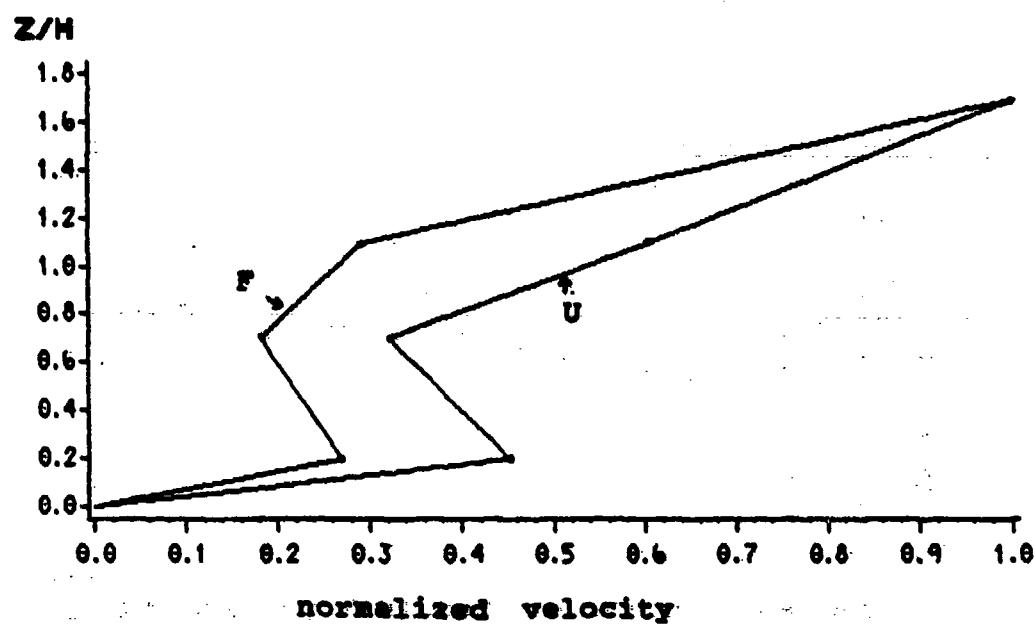


Fig. 7 Vertical profiles of velocity in the foliated (F) and unfoliated (U) canopies at $x=10$. Velocity is normalized by the velocity at 24m. Height is normalized by canopy height (H , 14m). One hour averages with edge fetch winds.

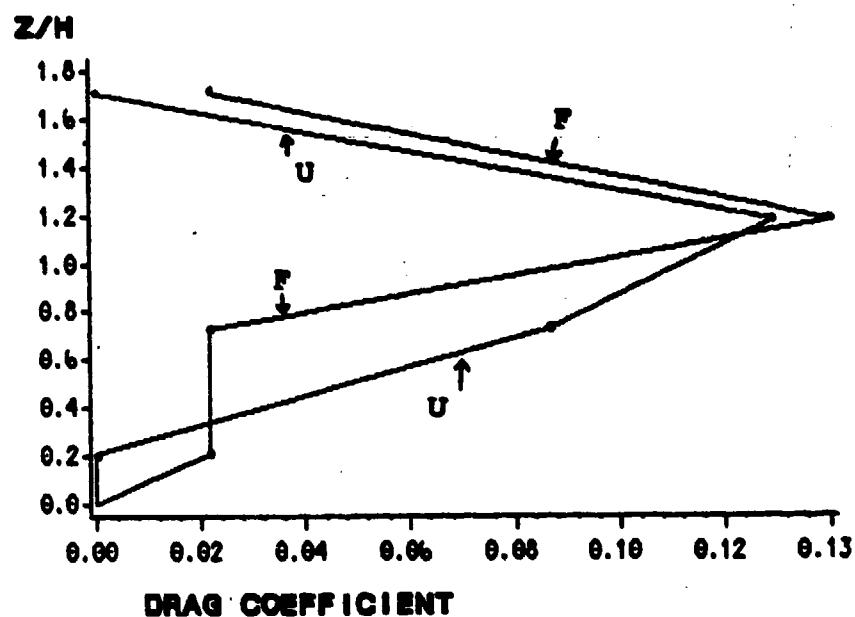


Fig. 8 Vertical profiles of drag coefficients in foliated (F) and unfoliated (U) canopies at $x=10$. One hour average with edge fetch winds. Height is normalized by canopy height (H).

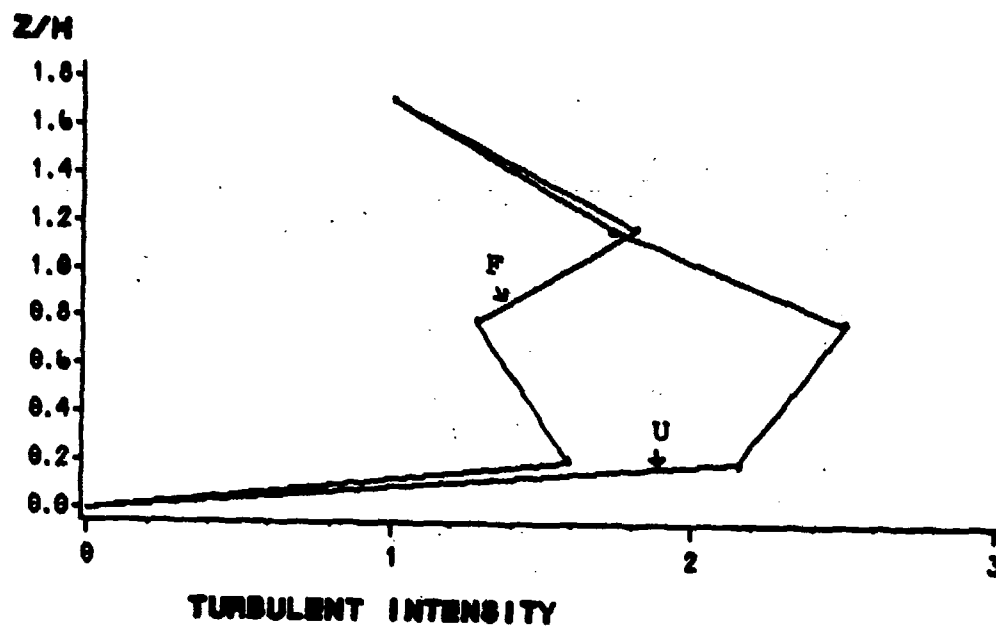


Fig. 9 Vertical profiles of turbulent intensity at $x=10$ in the foliated (F) and unfoliated (U) canopies with edge fetch winds. Turbulent intensity is normalized by turbulent intensity at 24m. Height is normalized by canopy height (H). One hour averages.

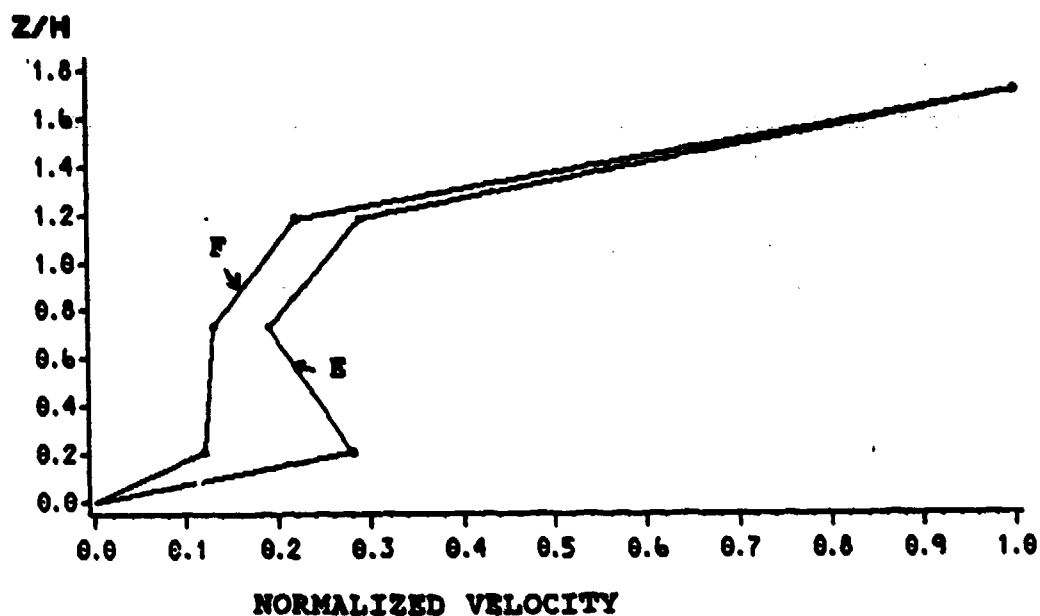


Fig. 10 Vertical profiles of velocity in edge fetch (E) and forest fetch (F) flows at $x=10$ in the foliated canopy. Axes are normalized as in Fig. 7 One hour averages.

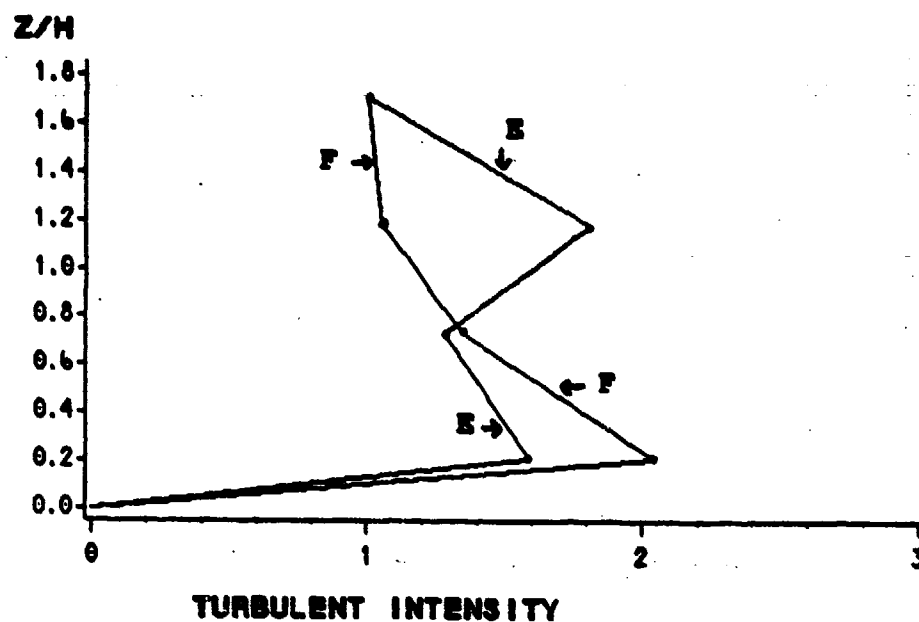


Fig. 11 Vertical profiles of turbulent intensity in edge fetch (E) and forest fetch (F) flows at $x=10$. One hour average in foliated canopy. Axes normalized as in Fig 9.

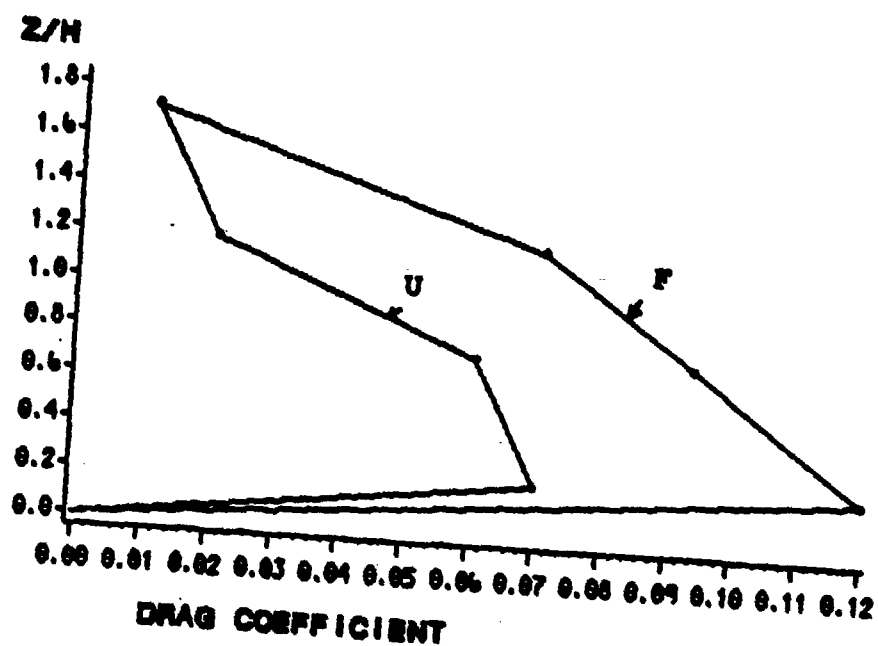


Fig. 12 Vertical profiles of drag coefficients in the foliated (F) and unfoliated (U) canopy with forest fetch winds. One hour averages with axes normalized as previously.

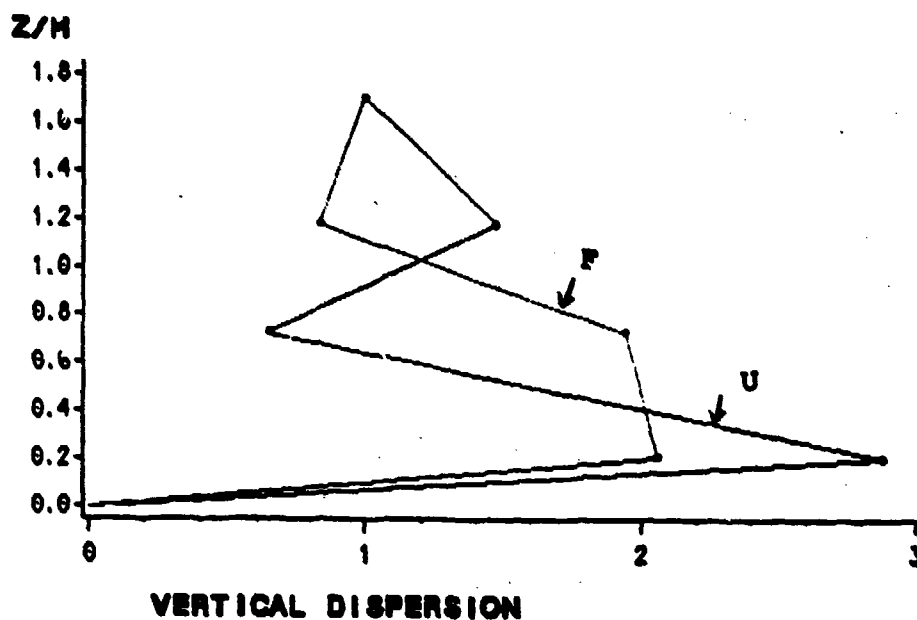


Fig. 13 Vertical profiles of vertical dispersion in the foliated (F) and unfoliated (U) canopy with edge fetch winds. Vertical axis normalized as previously. One hour averages.

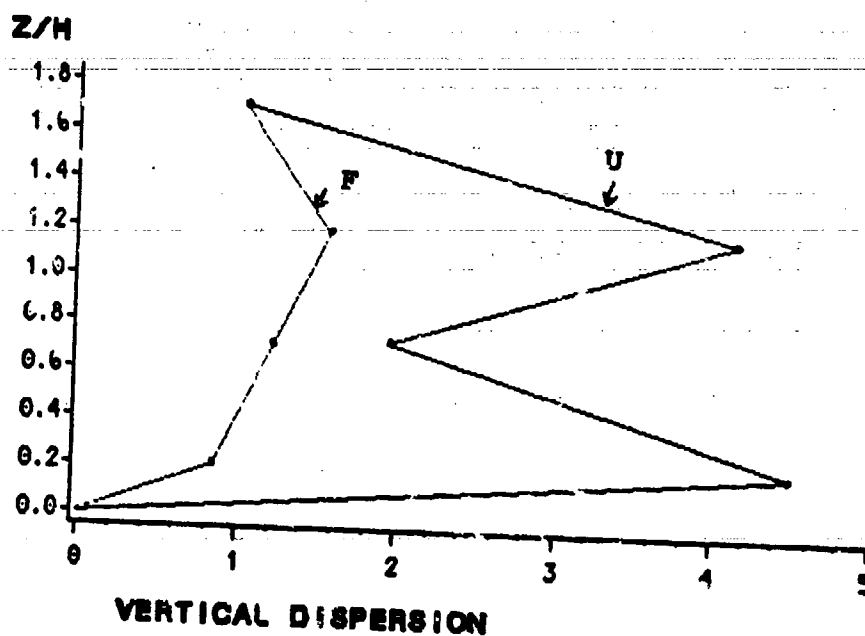


Fig. 14 Vertical profiles of vertical dispersion in the foliated (F) and unfoliated (U) canopy with forest fetch winds. Vertical axis normalized as previously. One hour averages.

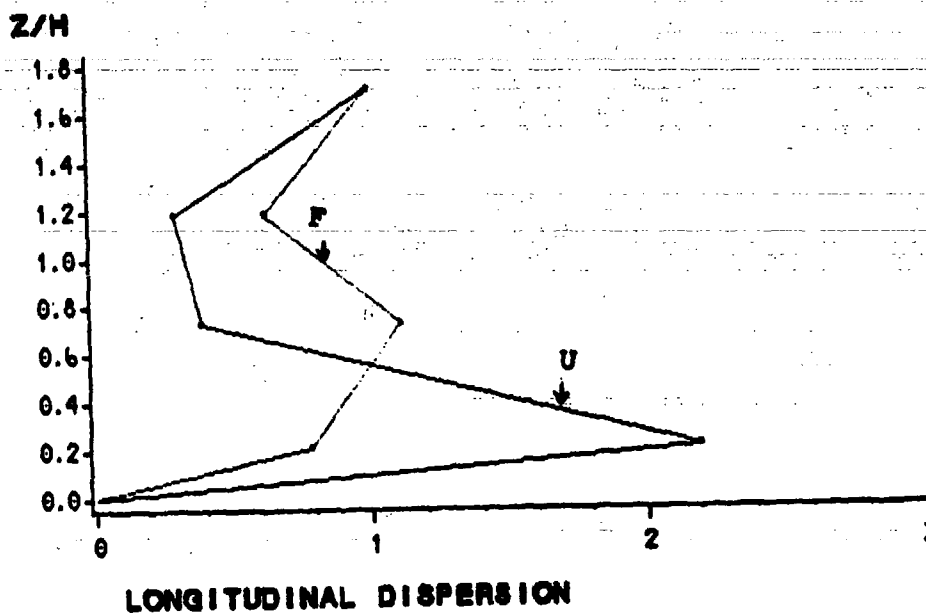


Fig. 15 Vertical profiles of longitudinal dispersion in the foliated (F) and unfoliated (U) canopies with edge fetch winds. One hour average with vertical axis scaled as previously.

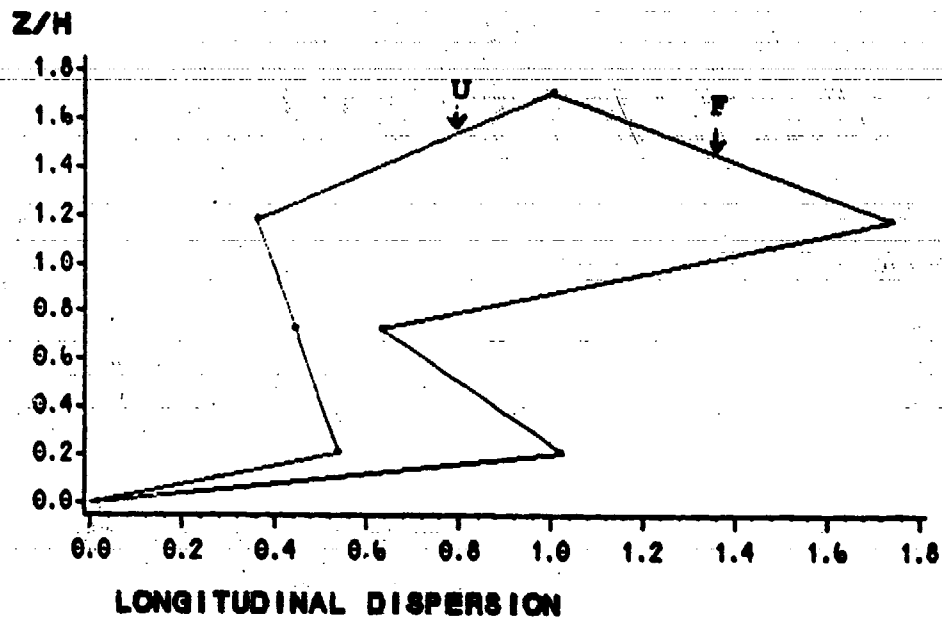


Fig. 16 Vertical profiles of longitudinal dispersion in the foliated (F) and unfoliated (U) canopies with forest fetch winds. One hour average with vertical axis scaled as previously.

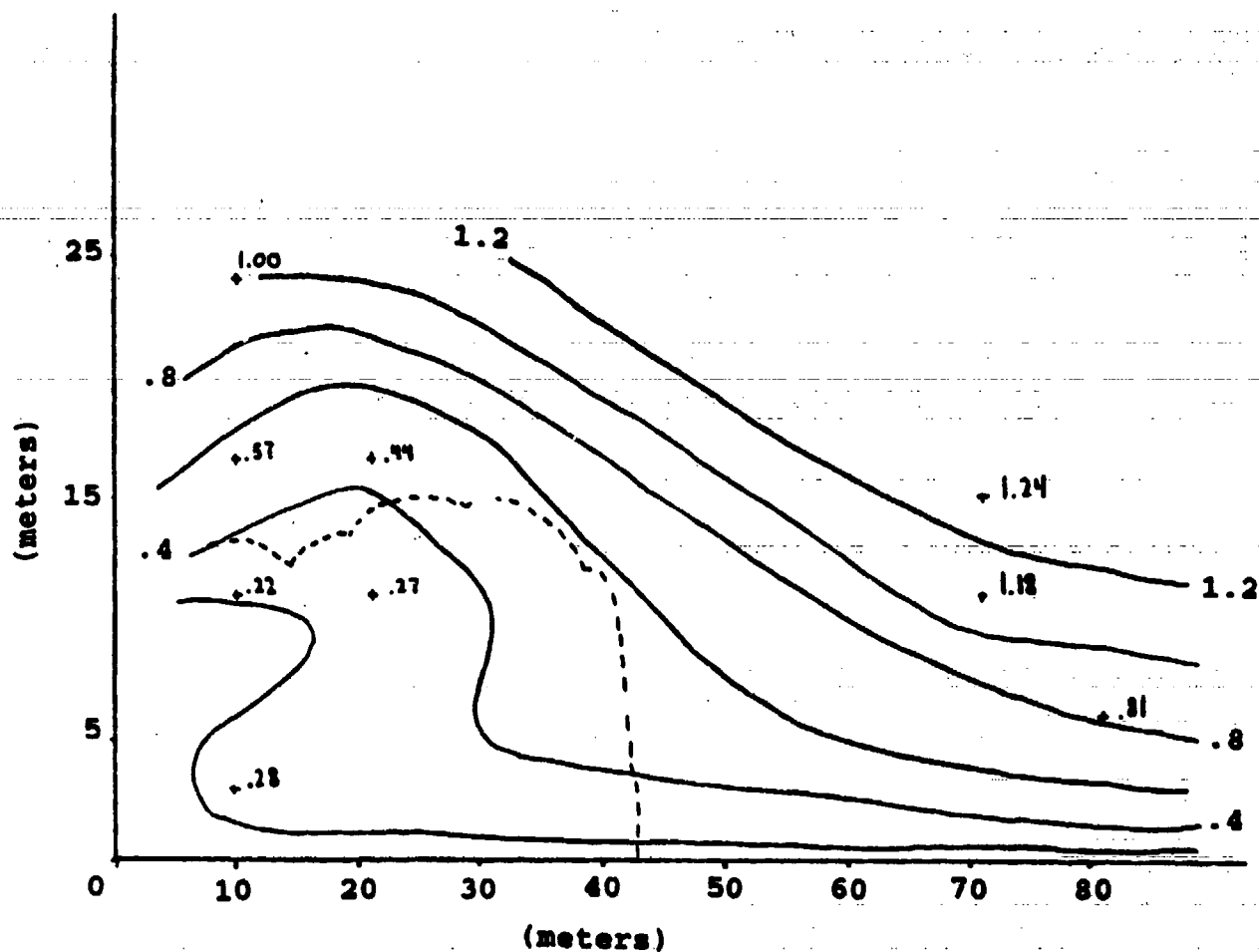


Fig. 17 Contour plot of U_{tot} / U_{w124} in and near the foliated canopy. (Canopy cross-section dashed) Actual data values are shown and are indicated by (+). The data value at coordinate point 10,24 is 1.00 by definition. This plot is a composite of one hour averages. Vertical scale equals 2X horizontal scale.

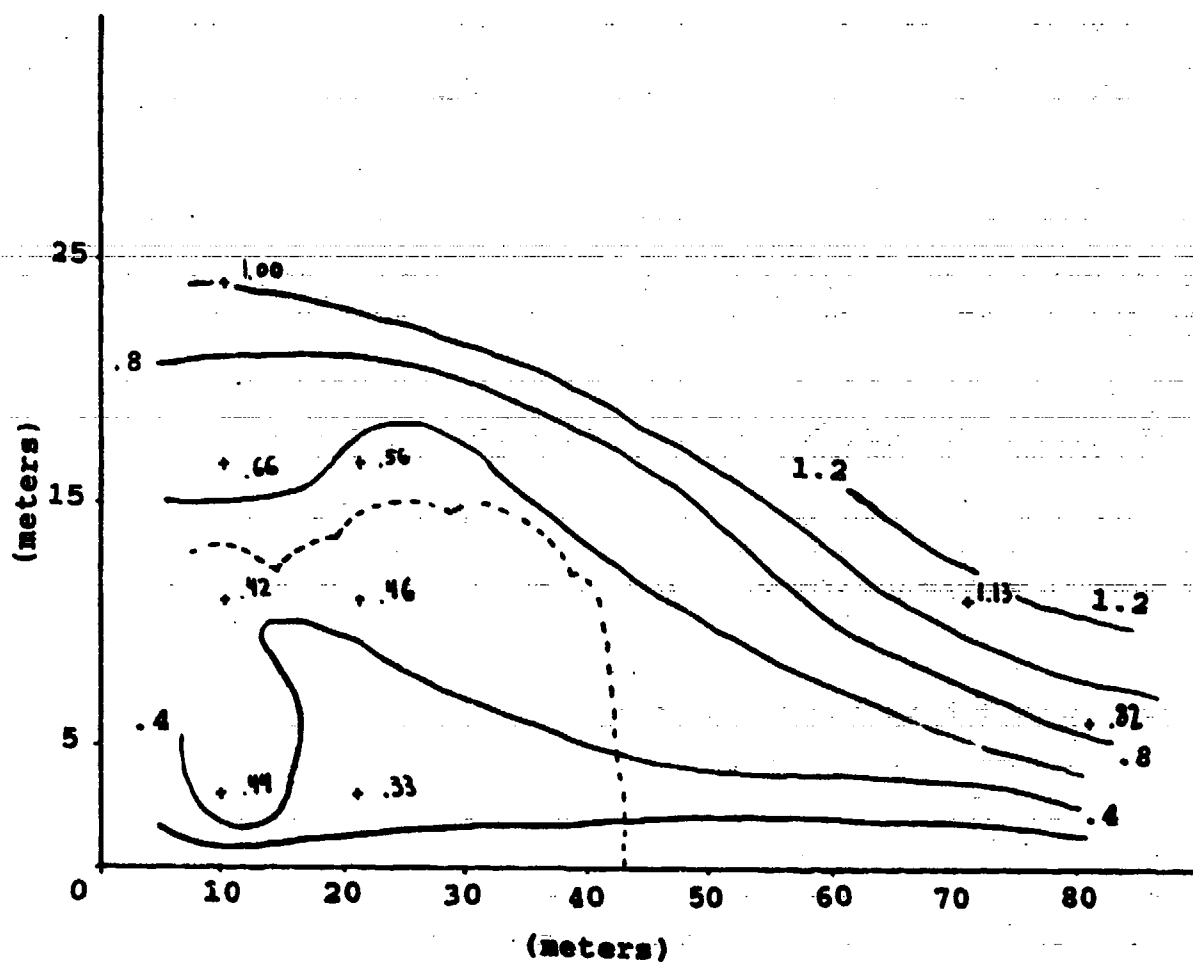


Fig. 18 Contour plot of $U_{wt}/U_{wt,24}$ in and near the unfoliated canopy. (Canopy cross-section dashed) Actual data values are shown and are indicated by (+). The data value at coordinate 10,24 is 1.00 by definition. This plot is a composite of one hour averages. Vertical scale equals 2X horizontal scale.

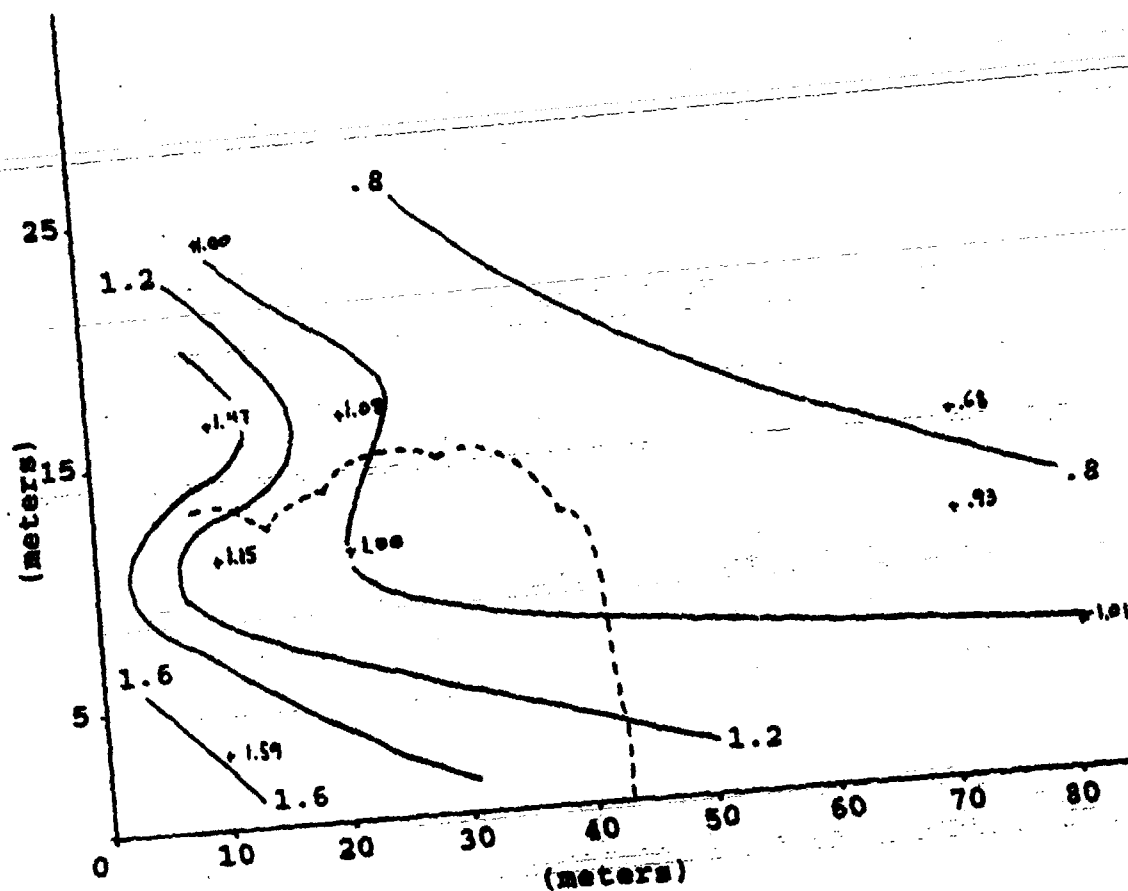


Fig. 19 Contour plot of $TI/TIAM$ in and near the foliated canopy. (Canopy cross-section dashed) Actual data values are shown and are indicated by (+). The data value at coordinate point 10,24 is 1.00 by definition. This plot is a composite of one hour averages. Vertical scale equals 2X horizontal scale.

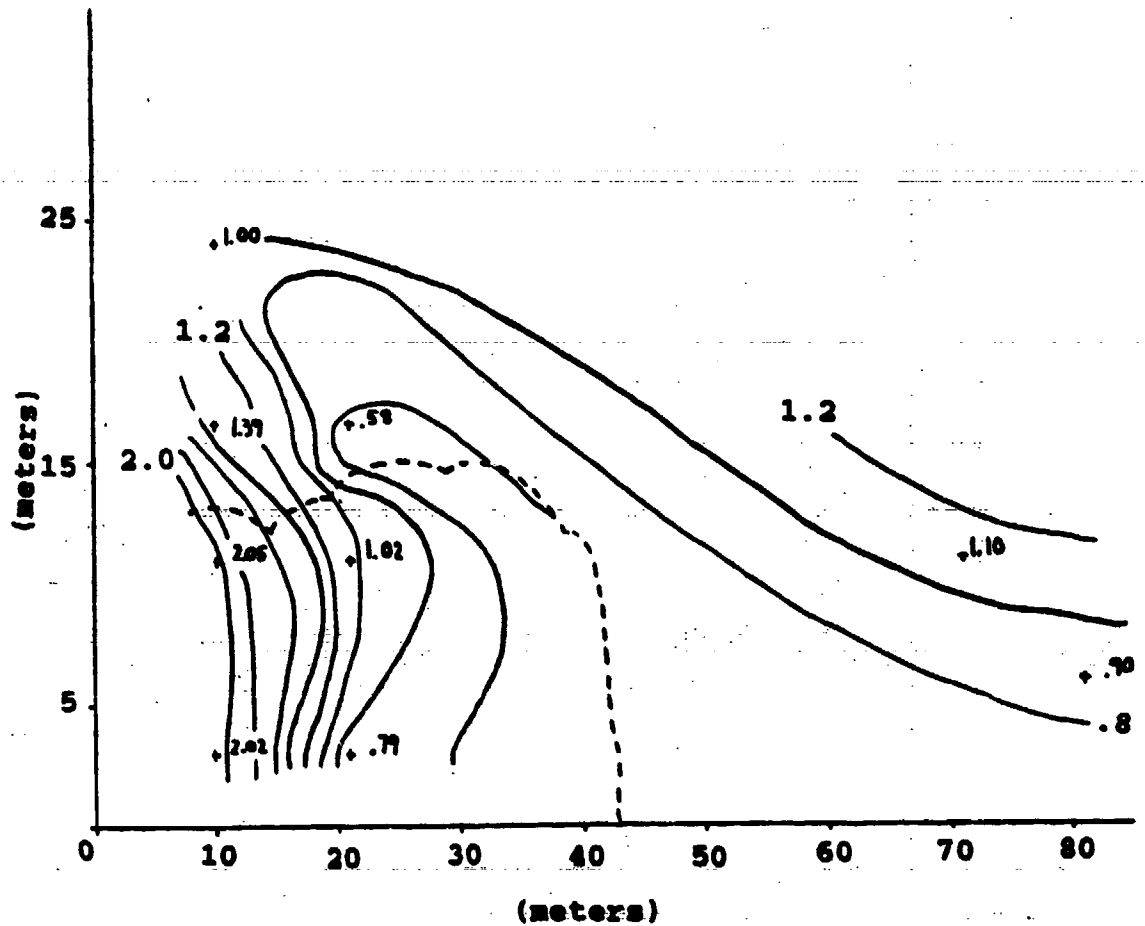


Fig. 20 Contour plot of $TI/TI_{0.24}$ in and near the unfoliated canopy. (Canopy cross-section dashed) Actual data values are shown and are indicated by (+). The data value at coordinate point 10,24 is 1.00 by definition. This plot is a composite of one hour averages. Vertical scale equals 2X horizontal scale.

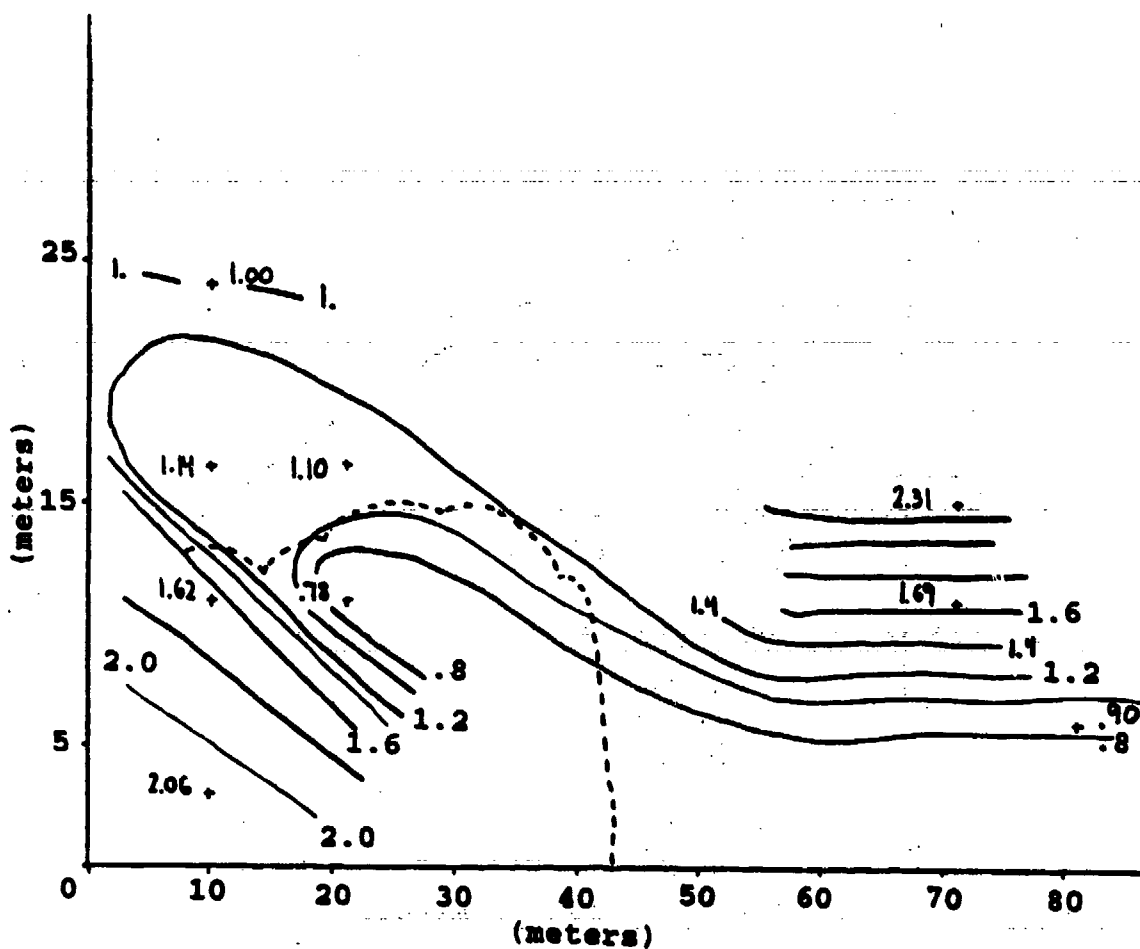


Fig 21 Contour plot of D_w in and near the foliated canopy. (Canopy cross-section dashed) This statistic is a normalized indicator of vertical dispersion. Actual data values are shown and are indicated by (+). The data value at coordinate point 10,24 is 1.00 by definition. This plot is a composite of one hour averages. Vertical scale equals 2X horizontal scale.

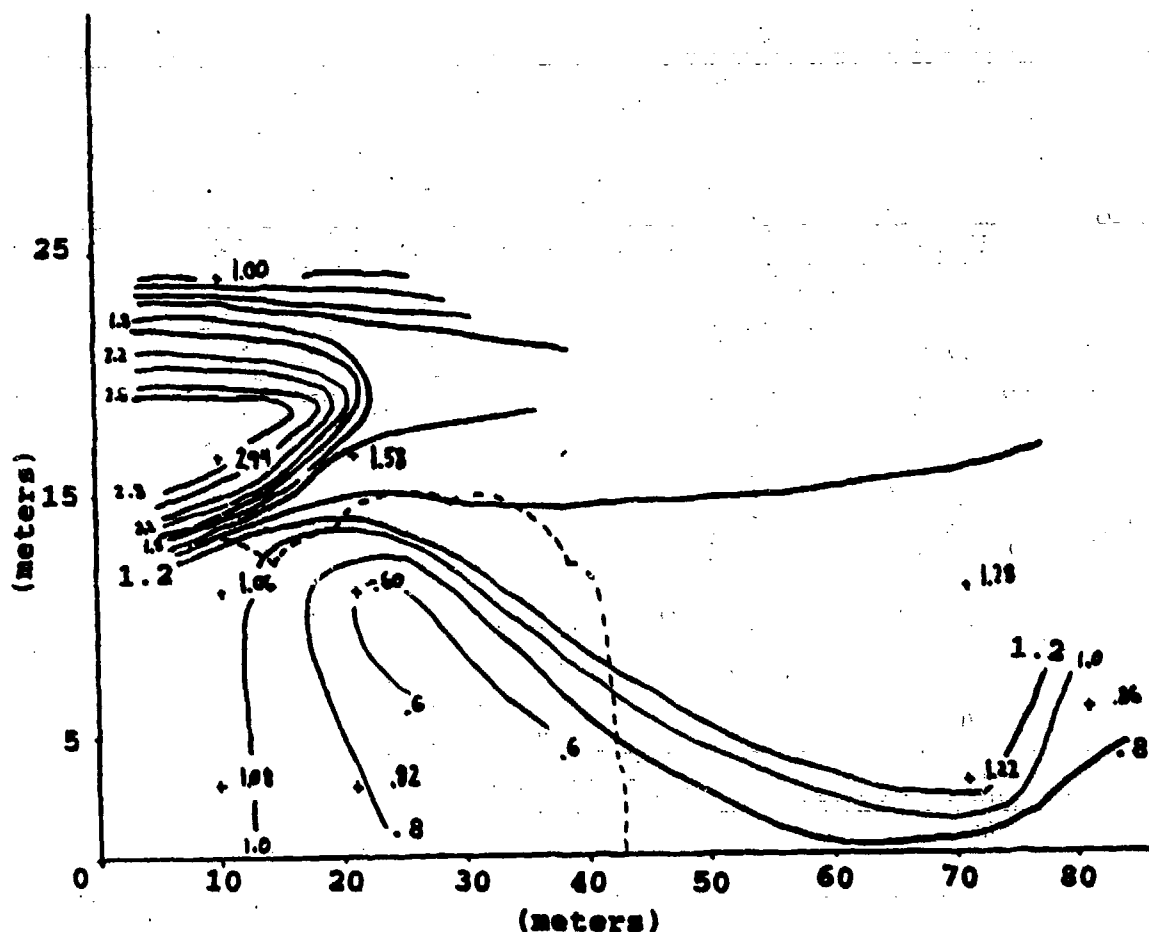


Fig. 22 Contour plot of D_w in and near the unfoliated canopy. (Canopy cross-section dashed) This statistic is a normalized indicator of vertical dispersion. Actual data values are shown and are indicated by (+). The data value at coordinate point 10,24 is 1.00 by definition. This plot is a composite of one hour averages. Vertical scale equals 2X horizontal scale.

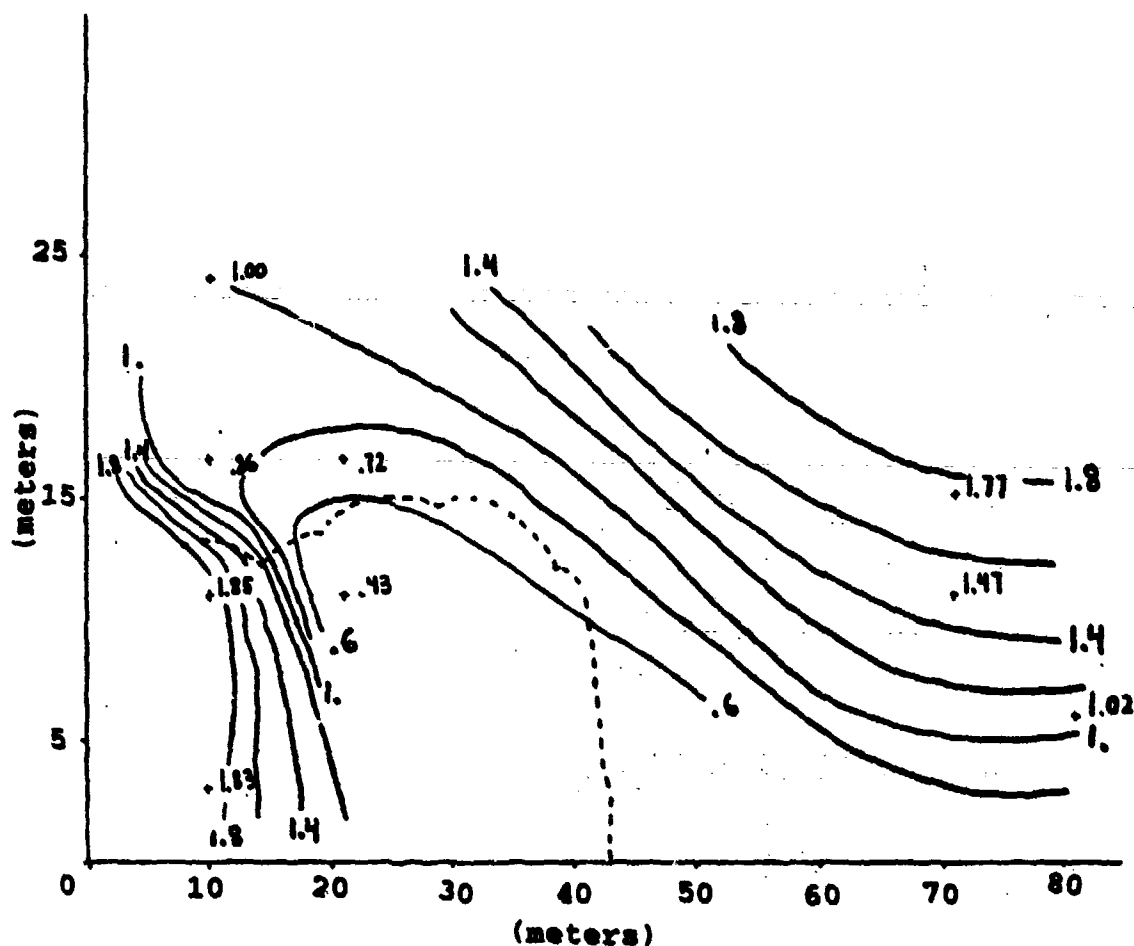


Fig. 23 Contour plot of D_1 in and near the foliated canopy. (Canopy cross-section dashed) This statistic is a normalized indicator of longitudinal dispersion. Actual data values are shown and are indicated by (+). The data value at coordinate point 10, 24 is 1.00 by definition. This plot is a composite of one hour averages. Vertical scale equals 2X horizontal scale.

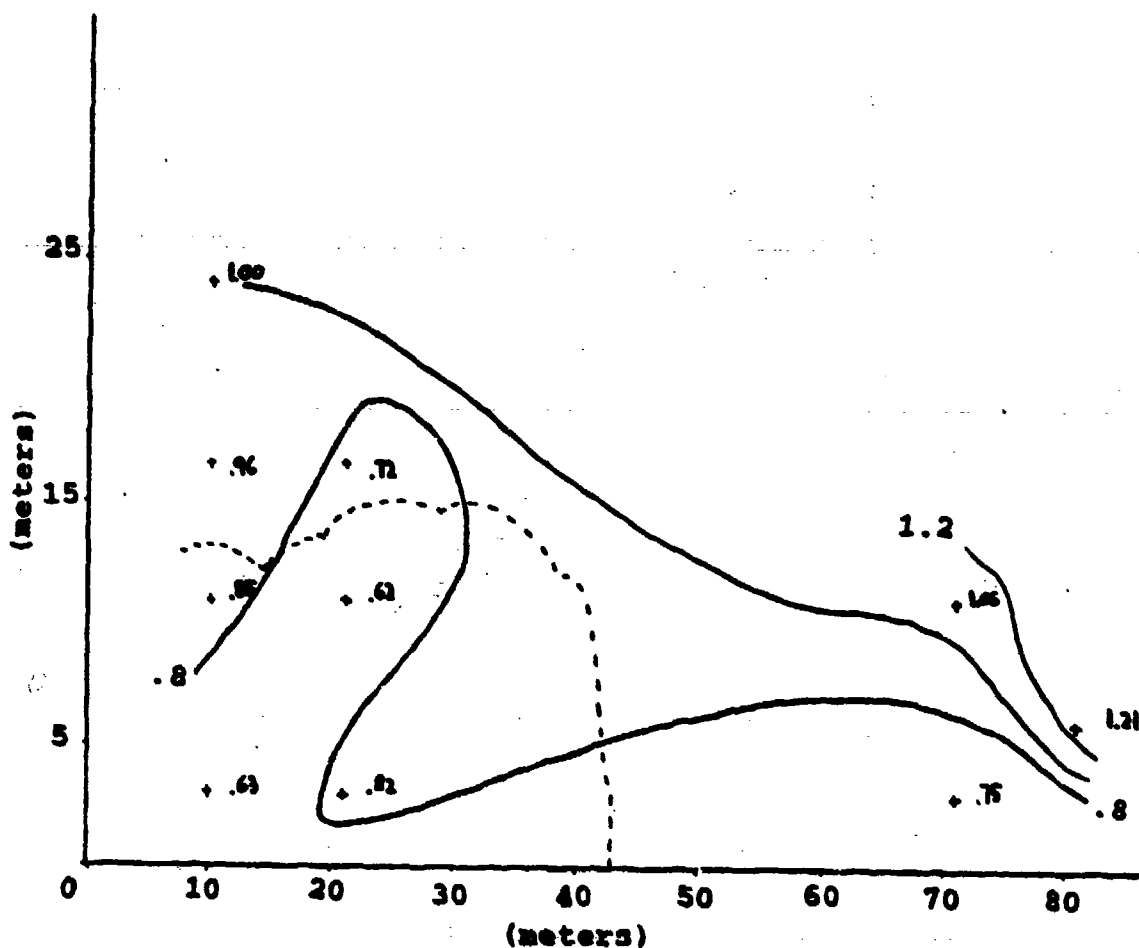


Fig 24 Contour plot of D_L in and near the unfoliated canopy. (Canopy cross-section dashed) This statistic is a normalized indicator of longitudinal dispersion. Actual data values are shown and indicated by (+). The data value at coordinate point 10,24 is 1.00 by definition. This plot is a composite of one hour averages. Vertical scale equals 2X horizontal scale.

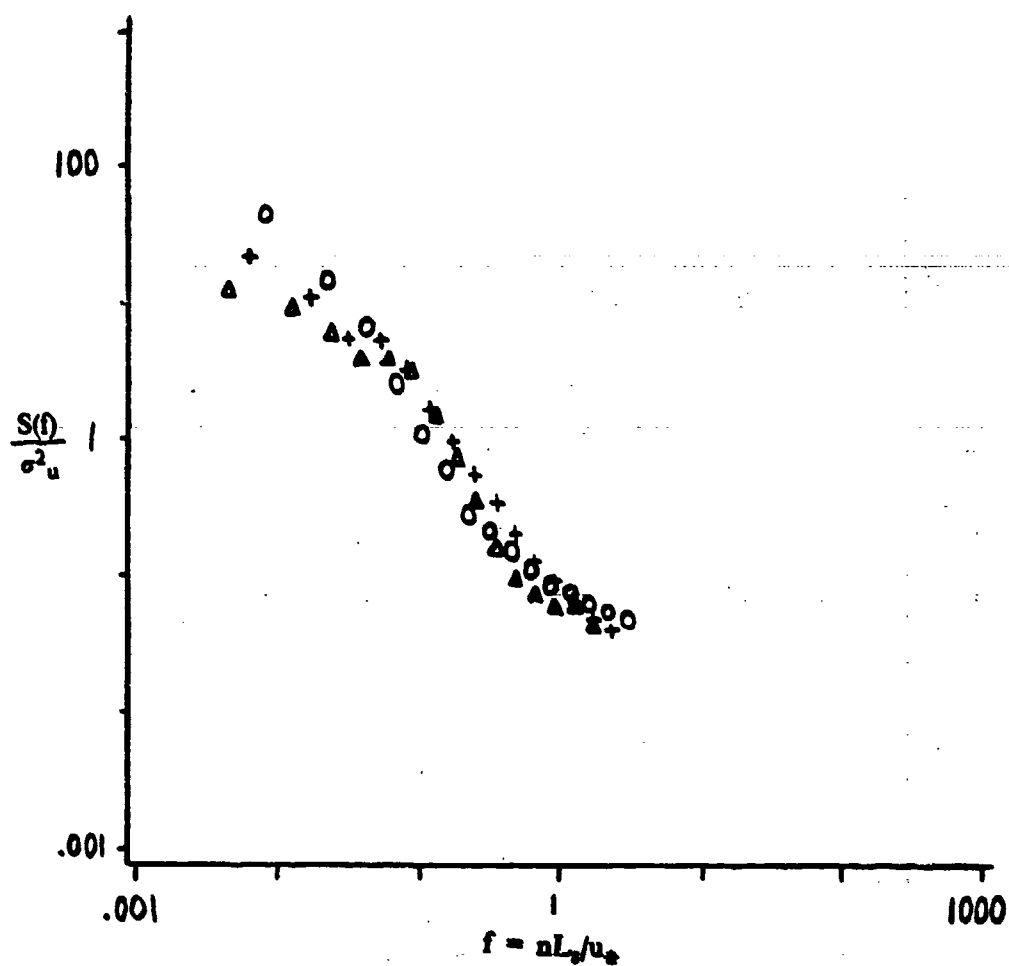


Fig. 25 In and near canopy spectra of u' scaled by u_* (as shown) with + = 16.5m, Δ = 11m and o = 3m. In the foliated canopy at $x=10$. 5 Hz ensemble averages of 10 consecutive 6 minute runs.

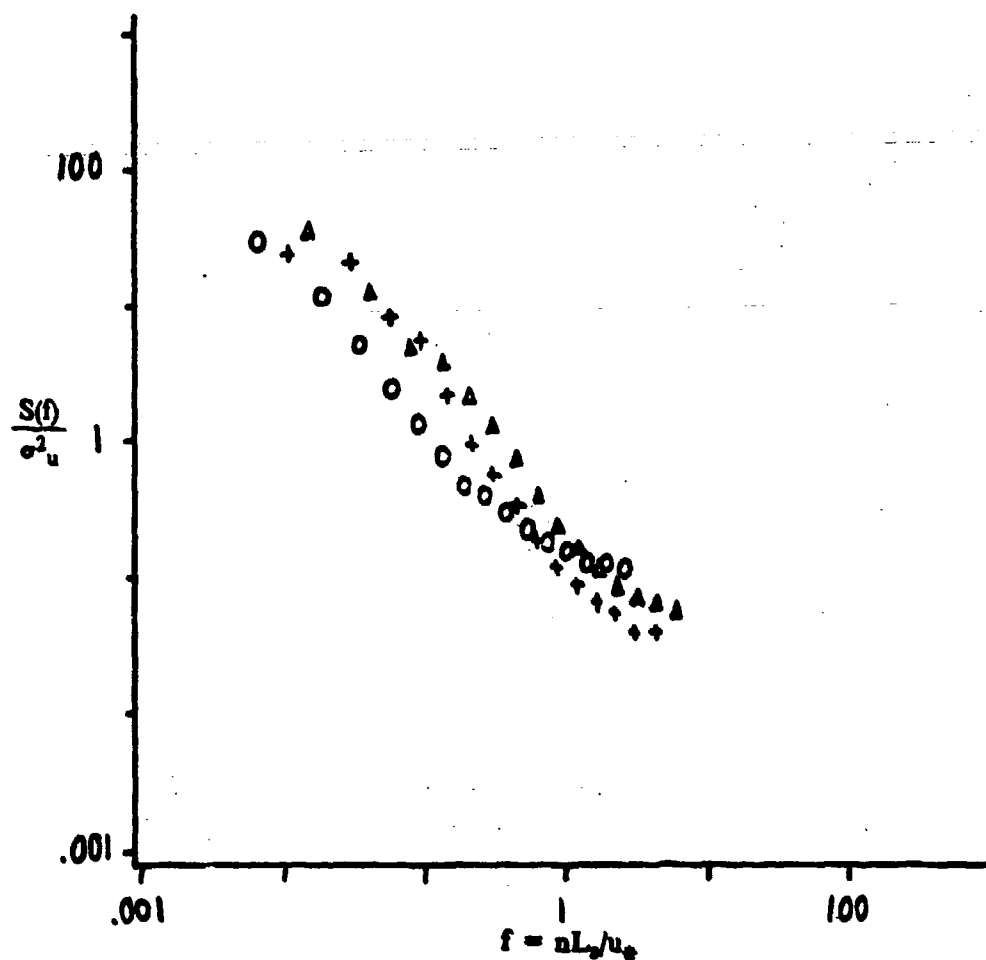


Fig. 26 In and near canopy spectra of u' scaled by u_* (as shown) with $+$ = 16.5m, Δ = 11m and o = 3m. In the unfoliated canopy at $x=10$. 5 Hz ensemble averages of 10 consecutive 6 minute runs.

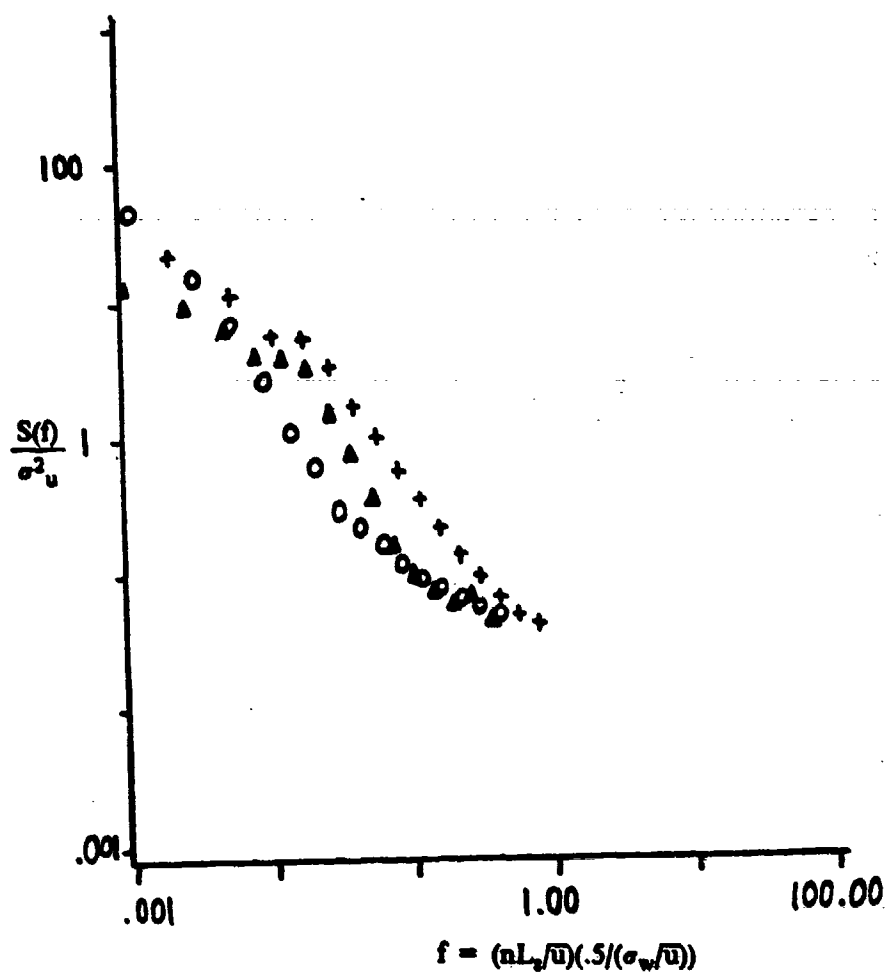


Fig. 27 In and near canopy spectra of u' scales by Lagrangian scale (as shown) with + = 16.5, Δ = 11m and o = 3 m. In foliated canopy at $x=10$. 5 Hz ensemble averages of 10 consecutive 6 minute runs.

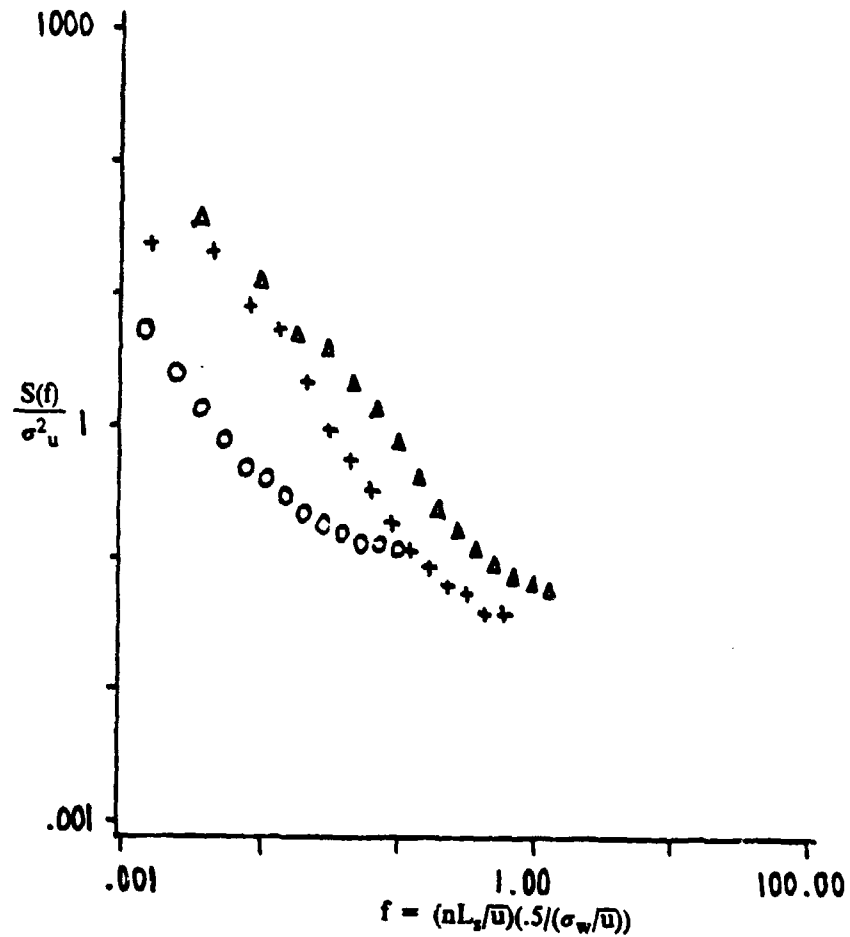


Fig. 28 In and near canopy spectra of u' scaled by Lagrangian scale (as shown) with + = 16.5m, Δ = 11m and o = 3m. In the unfoliated canopy at x^* , 5 Hz ensemble averages of 10 consecutive 6 min runs.

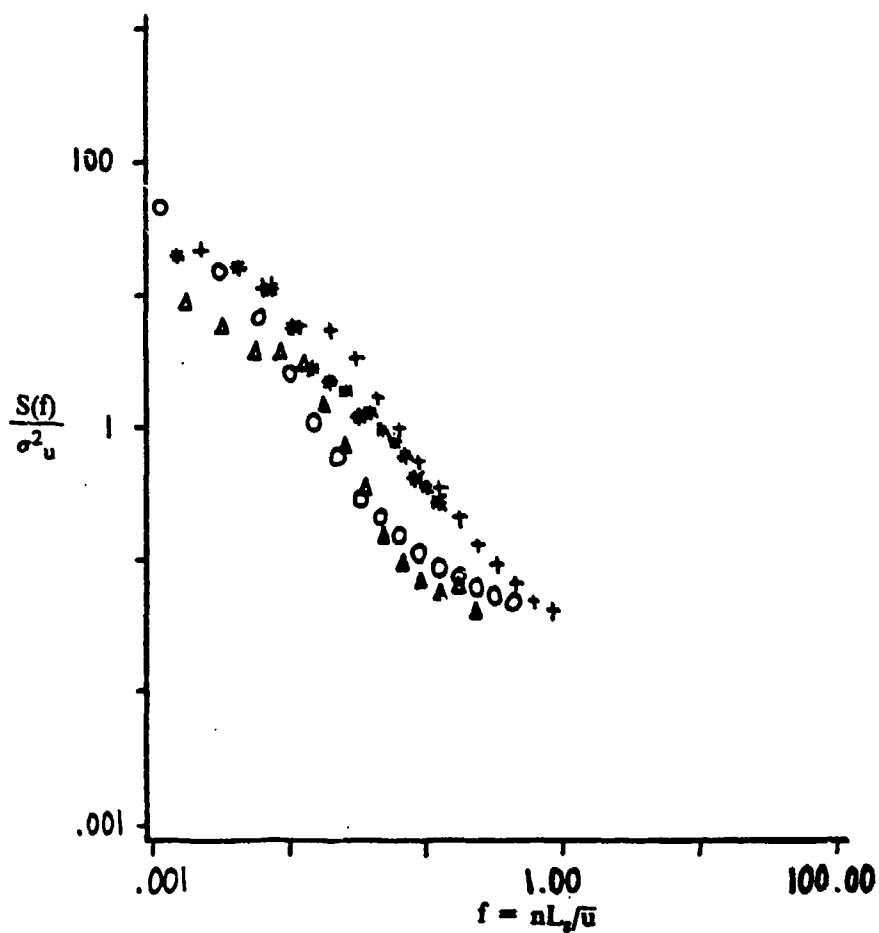


Fig. 29 Spectra of u' from the vertical profile at $x=10$ in the foliated canopy with $\Psi = 24\text{m}$, $+$ = 16.5m , Δ = 11m and \circ = 3m . Spectra are 5 Hz ensemble averages of 10 consecutive 6 minute runs. Edge fetch winds.

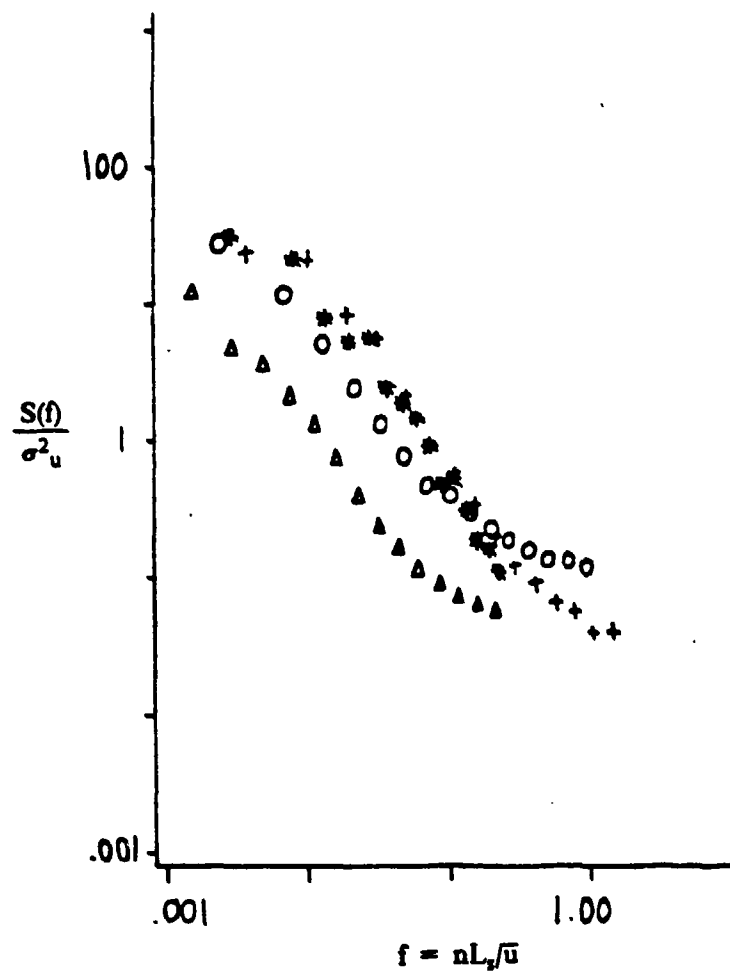


Fig. 30 Spectra of u' from the vertical profile at $x=10$ in the unfoliated canopy with $\circ = 24\text{m}$, $+ = 16.5\text{m}$, $\Delta = 11\text{m}$ and $\circ = 3\text{m}$. Spectra are 5 Hz ensemble averages of 10 consecutive 6 minute runs. Edge fetch winds.

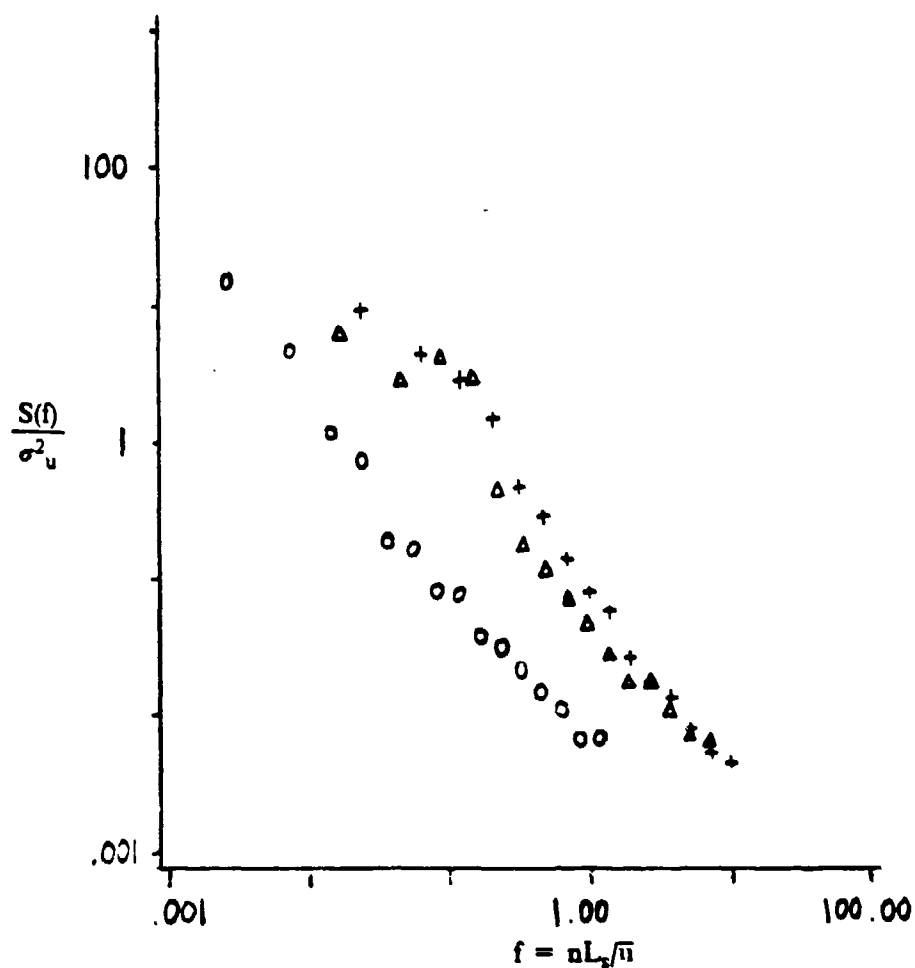


Fig. 31 Spectra of u' from the vertical profile at $x=10$ in the foliated canopy with $+$ = 16.5m, Δ = 11m and \circ = 3m. Spectra are 20 Hz ensemble averages of 3 consecutive 100 sec runs. Edge fetch wind.

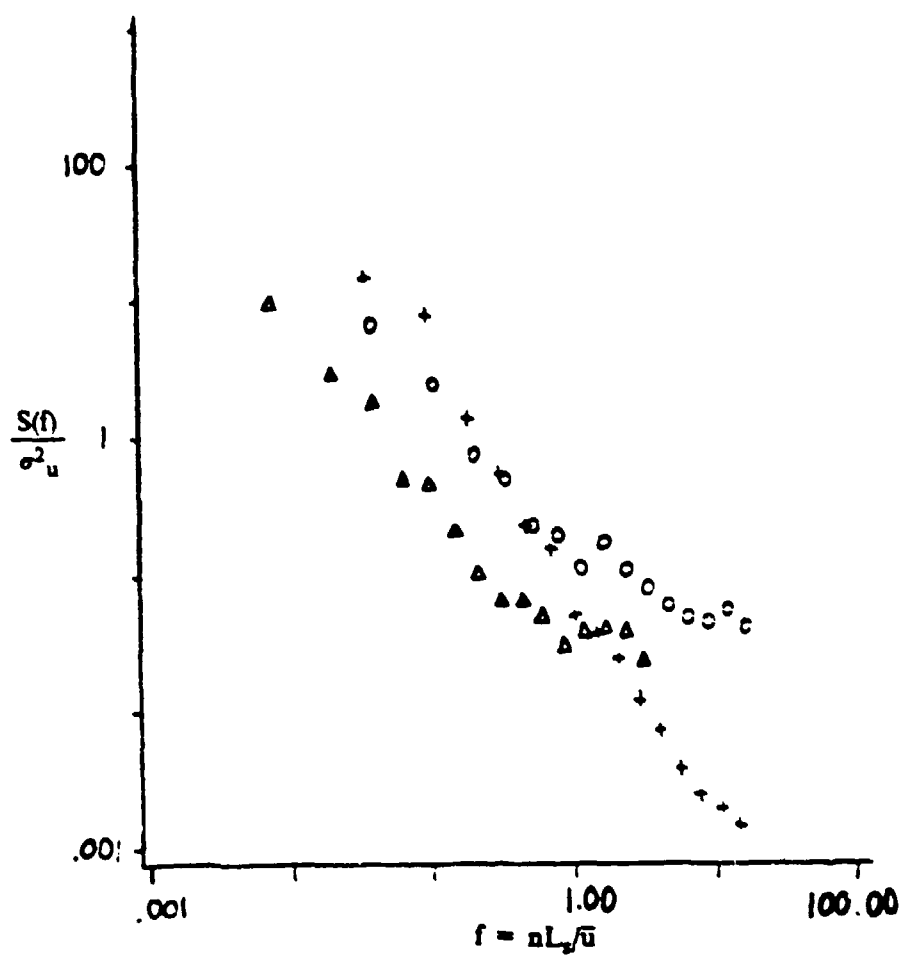


Fig. 32 Spectra of u' from the vertical profile at $x=10$ in the unfoliated canopy with $+$ = 16.5m, Δ = 11m and O = 3m. Spectra are 20 Hz ensemble averages of 3 consecutive 100 second runs. Edge fetch winds.

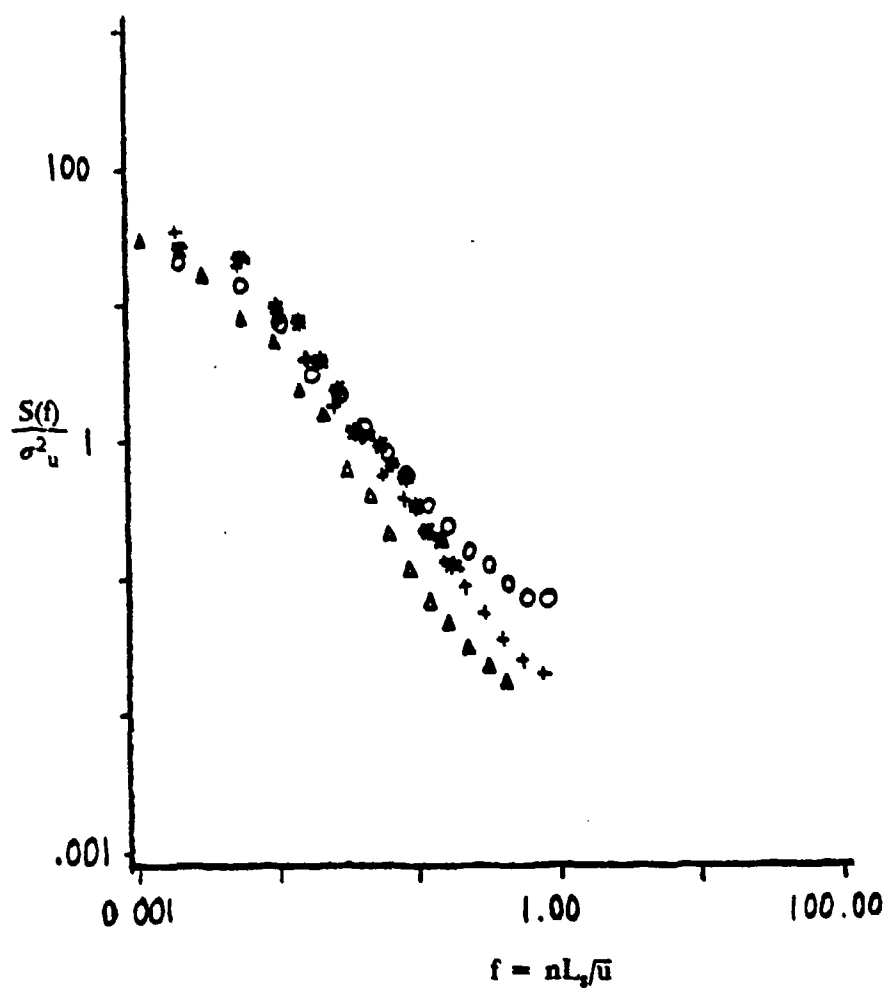


Fig. 33 Spectra of u' in horizontal transect with * at 10, 24, Δ at 10, 16.5, \circ at 21, 16.5 and + at 71, 15. Spectra of 5 Hz ensemble averages of 10 consecutive 6 minute runs. Foliated canopy and edge fetch winds.

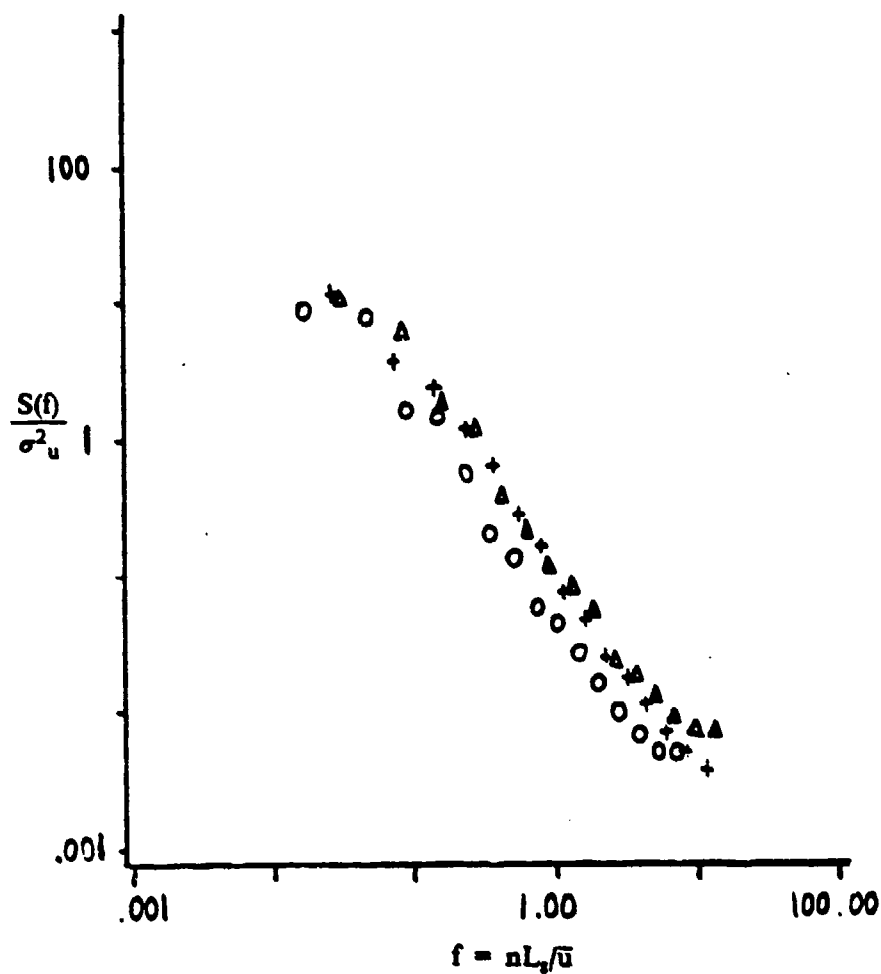


Fig. 34 Spectra of u' in horizontal transect with + at 71.15, Δ at 21, 16.5 and o at 10, 16.5. Spectra of 20 Hz ensemble averages of 3 consecutive 100 second runs. Foliated canopy and edge fetch winds.

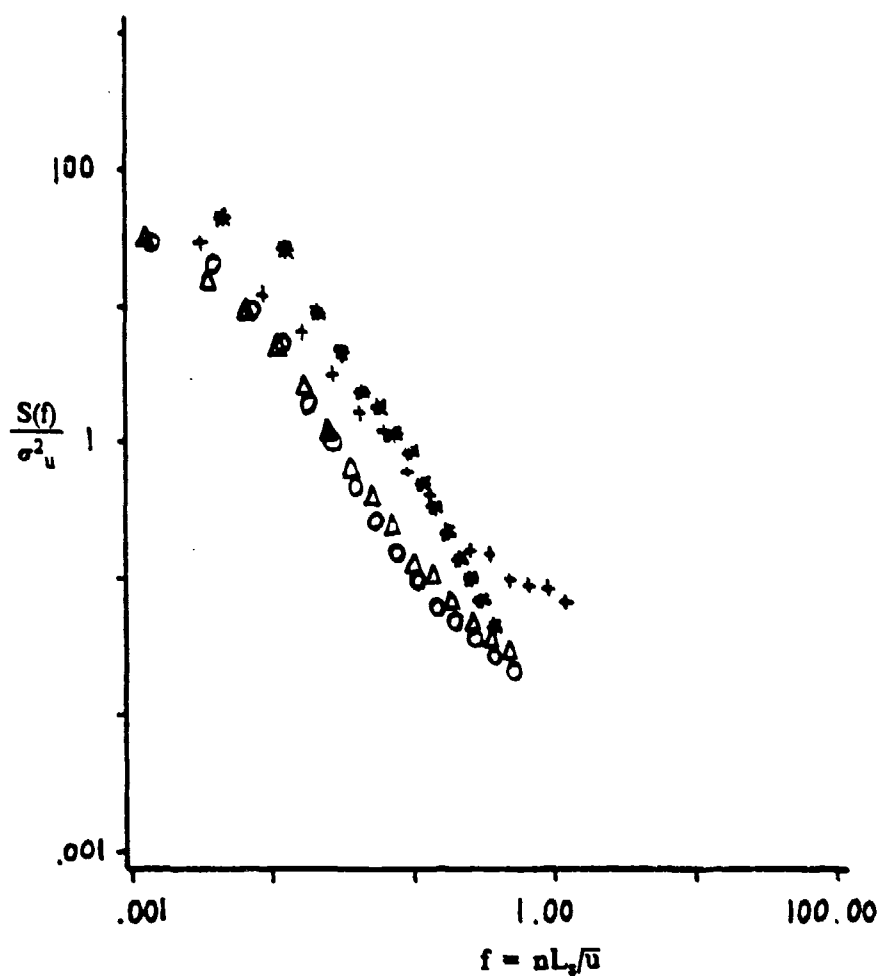


Fig. 35 Spectra of u' in horizontal transect with * at 10, 24, + at 71, 11, Δ at 21, 11 and \circ at 10, 11. Spectra of 5 Hz ensemble averages of 10 consecutive 6 minute runs. Foliated canopy and edge fetch winds.

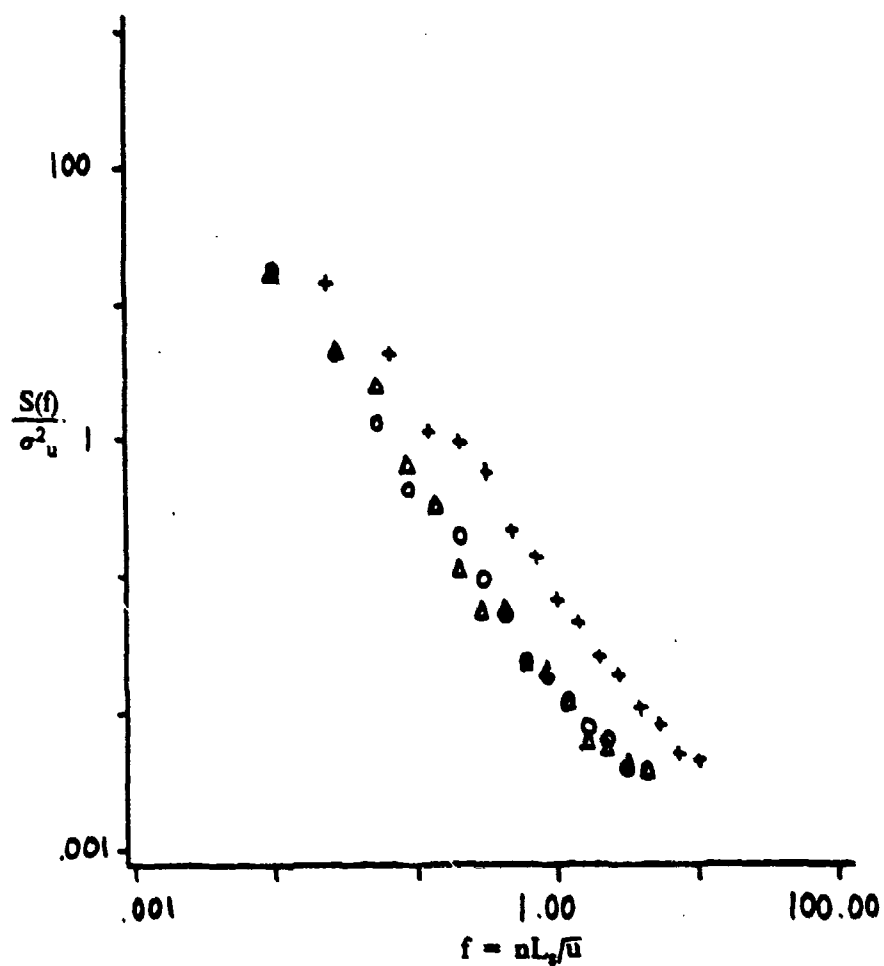


Fig. 36 Spectra of u' in horizontal transect with + at 71, Δ at 11, and o at 10.11. Spectra of 20 Hz ensemble averages of 3 consecutive 100 second runs. Foliated canopy and edge fetch winds.

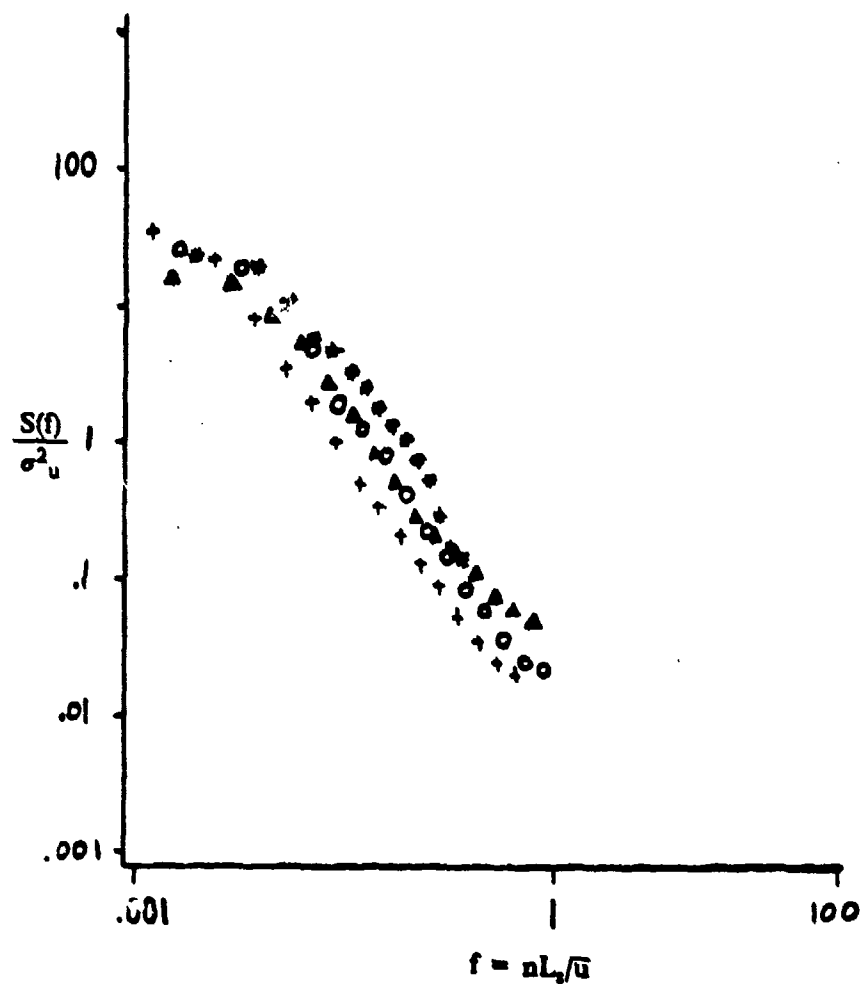


Fig. 37 Spectra of u' in horizontal transect with * at 10,24, + at 71,11, Δ at 21,11 and O at 10,11. Spectra of 5 Hz ensemble averages of 10 consecutive 6 minute runs. Unfoliated canopy and edge fetch winds.

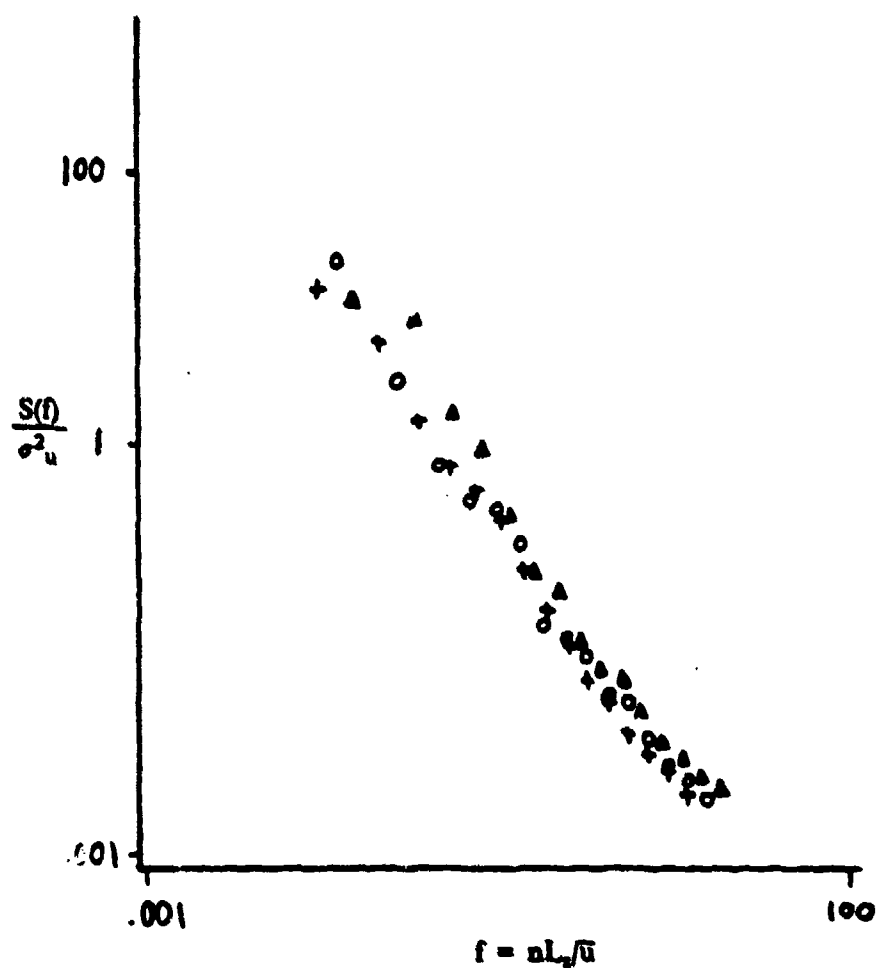


Fig. 38 Spectra of u' in horizontal transect with + at 71.11, Δ at 21.11 and o at 10.11. Spectra of 20 Hz ensemble averages of 3 consecutive 100 second runs. Unfoliated canopy and edge fetch winds.

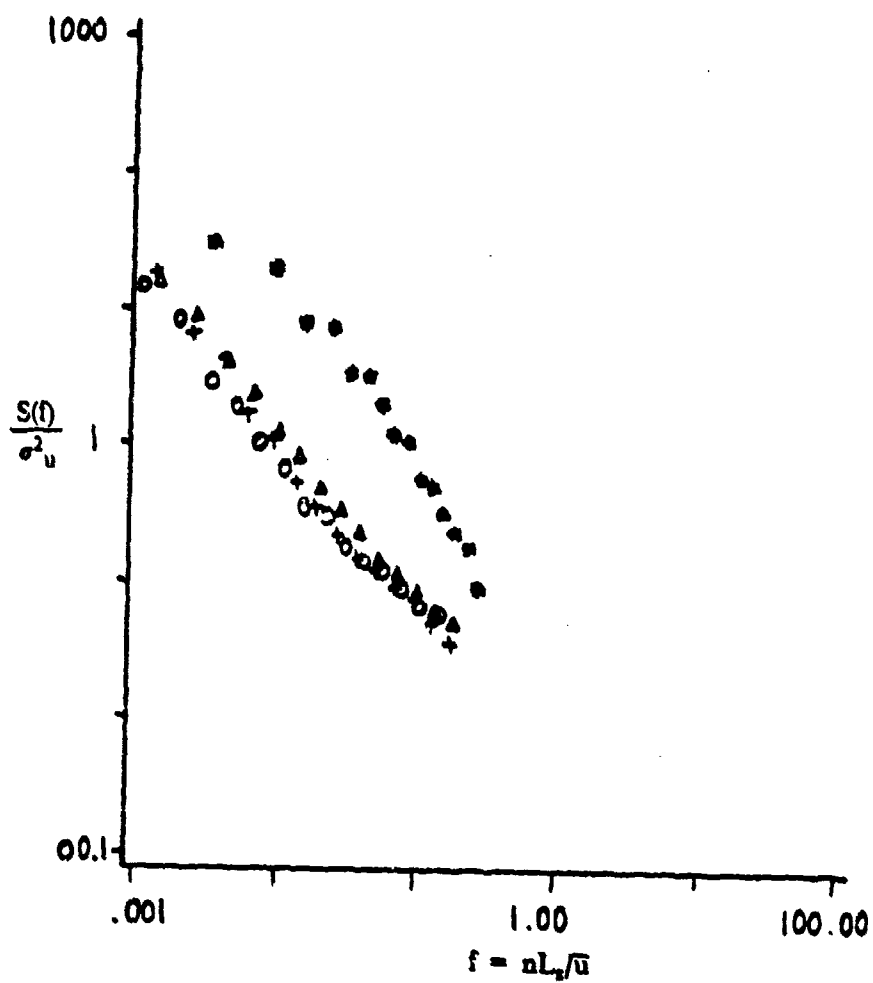


Fig. 39 Spectra of u' in horizontal transect with * at 10,24, + at 71,3, Δ at 21,3 and o at 10,3. Spectra of 5 Hz ensemble averages of 10 consecutive 6 minute runs. Unfoliated canopy and edge fetch winds.

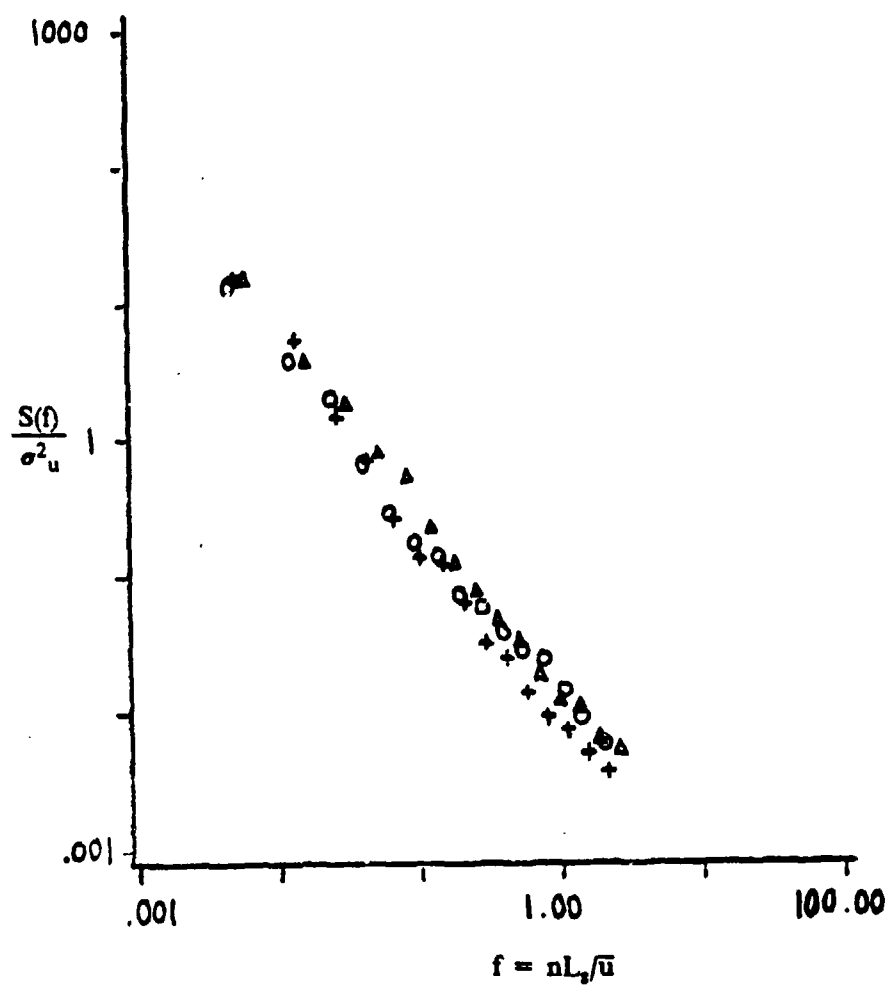


Fig. 40 Spectra of u' in horizontal transect with + at 71.3, Δ at 21.3 and \circ at 10.3. Spectra of 20 Hz ensemble averages of 3 consecutive 100 second runs. Unfoliated canopy and edge fetch winds.

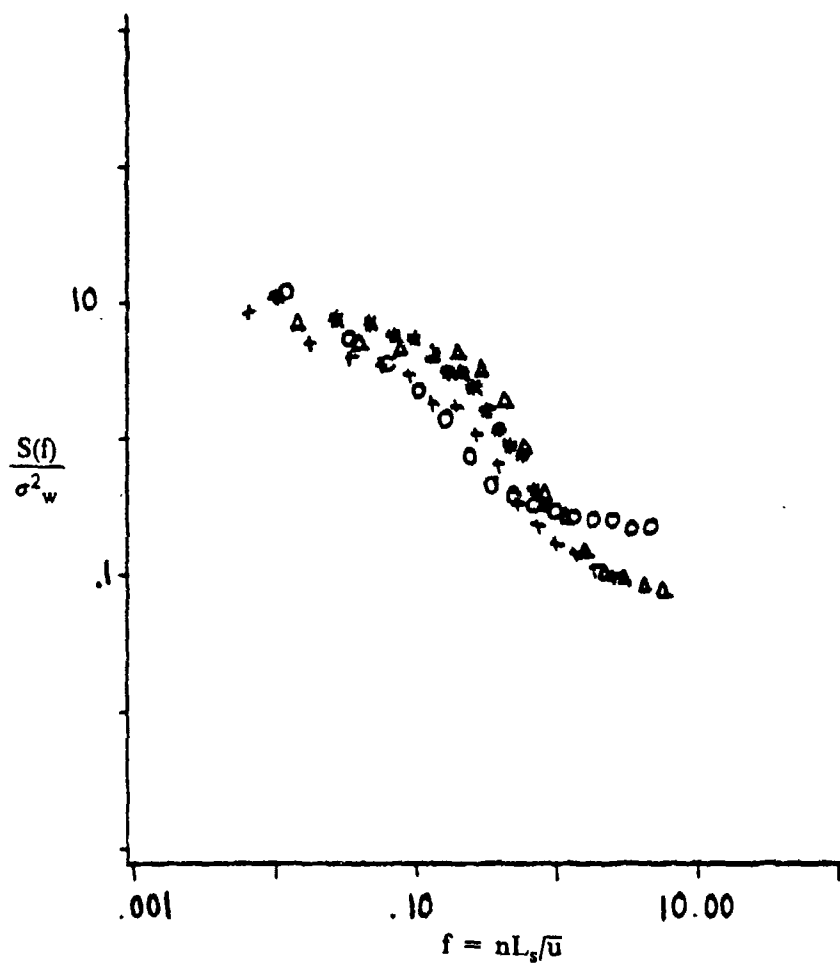


Fig. 41 Spectra of w' from the vertical profile at $x=10$ in the foliated canopy with * at 24m, + at 16.5m, Δ at 11m and \circ at 3m. These spectra are 5 Hz ensemble averages of 10 consecutive 6 minute runs with edge fetch winds.

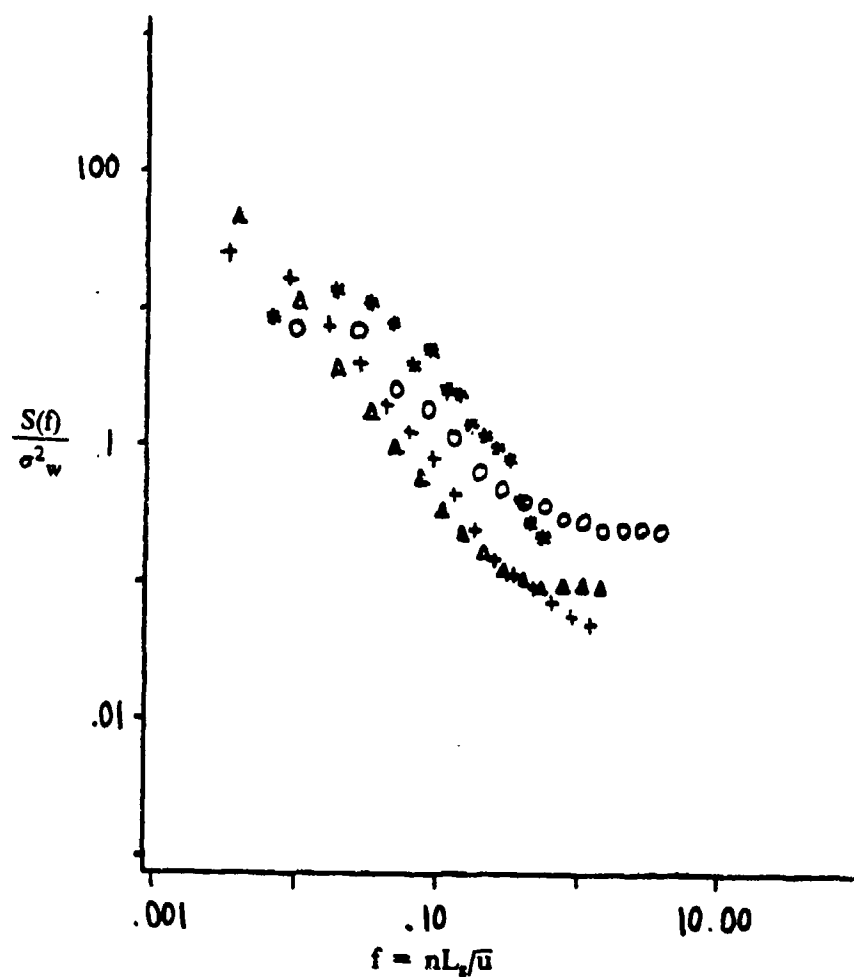


Fig. 42 Spectra of w' from the vertical profile at $x=10$ in the unfoliated canopy with * at 24m, + at 16.5m, Δ at 11m and o at 3m. These spectra are 5 Hz ensemble averages of 10 consecutive 6 minute runs with edge fetch winds.

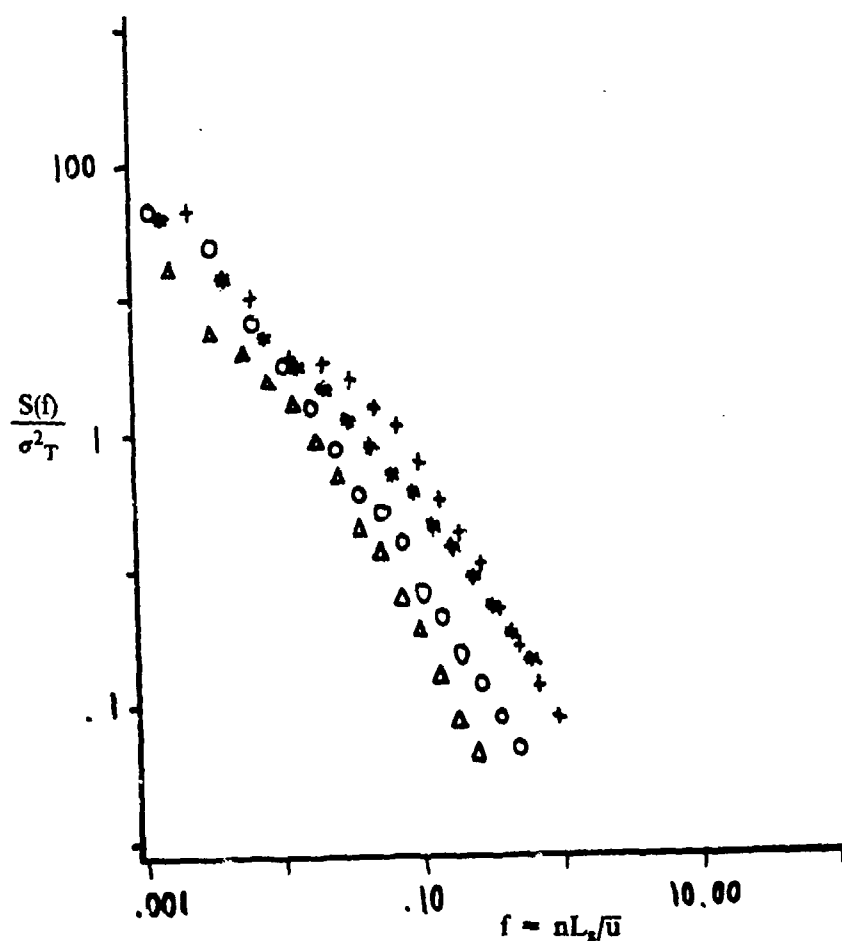


Fig 43 Spectra of temperature from the vertical profile at $x=10$ in the foliated canopy with * at 24m, + at 16.5m, Δ at 11m and \circ at 3m. Spectra are 5 Hz ensemble averages of 10 consecutive 6 minute runs with edge fetch winds.

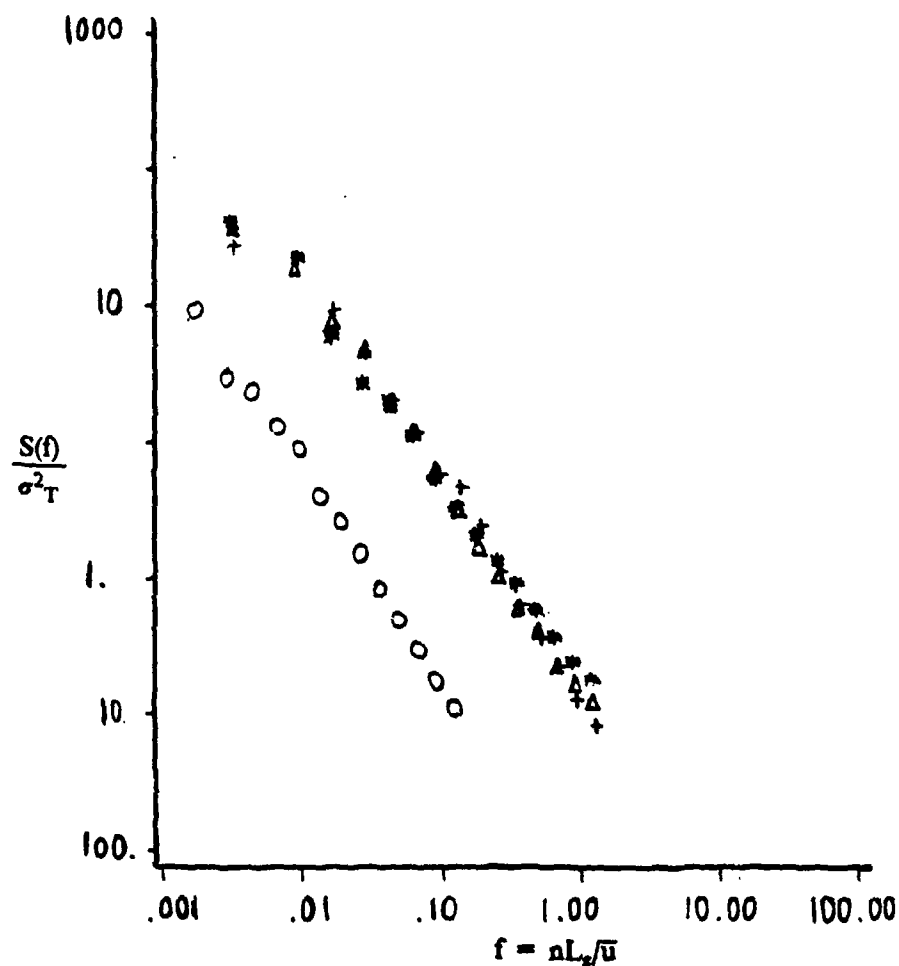


Fig. 44 Spectra of temperature from the vertical profile at $x=10$ in the unfoliated canopy with * at 24m, + at 16.5m, Δ at 11m and O at 3m. Spectra are 5 Hz ensemble averages of 10 consecutive 6 minute runs with edge fetch winds.

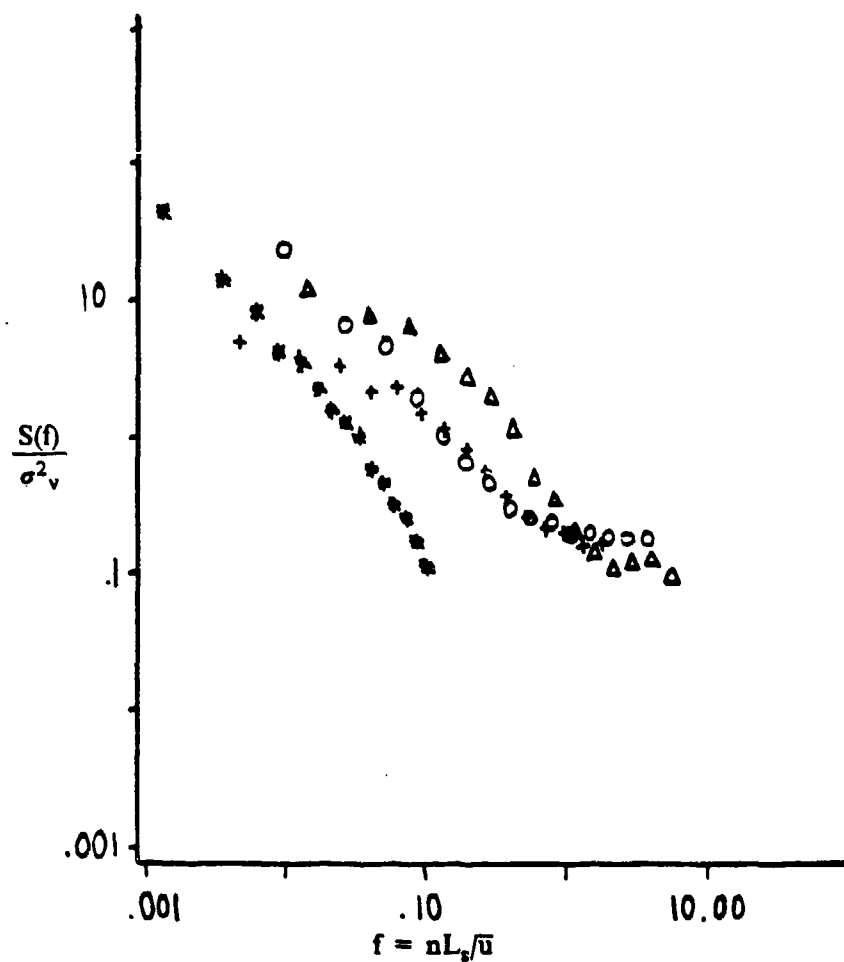


Fig. 45 Spectra of v' from the vertical profile in the foliated canopy at $x=10$ with * at 24m, + at 16.5 m, Δ at 11m and o at 3m. These spectra are 5 Hz ensemble averages of 10 consecutive 6 minute runs with edge fetch winds.

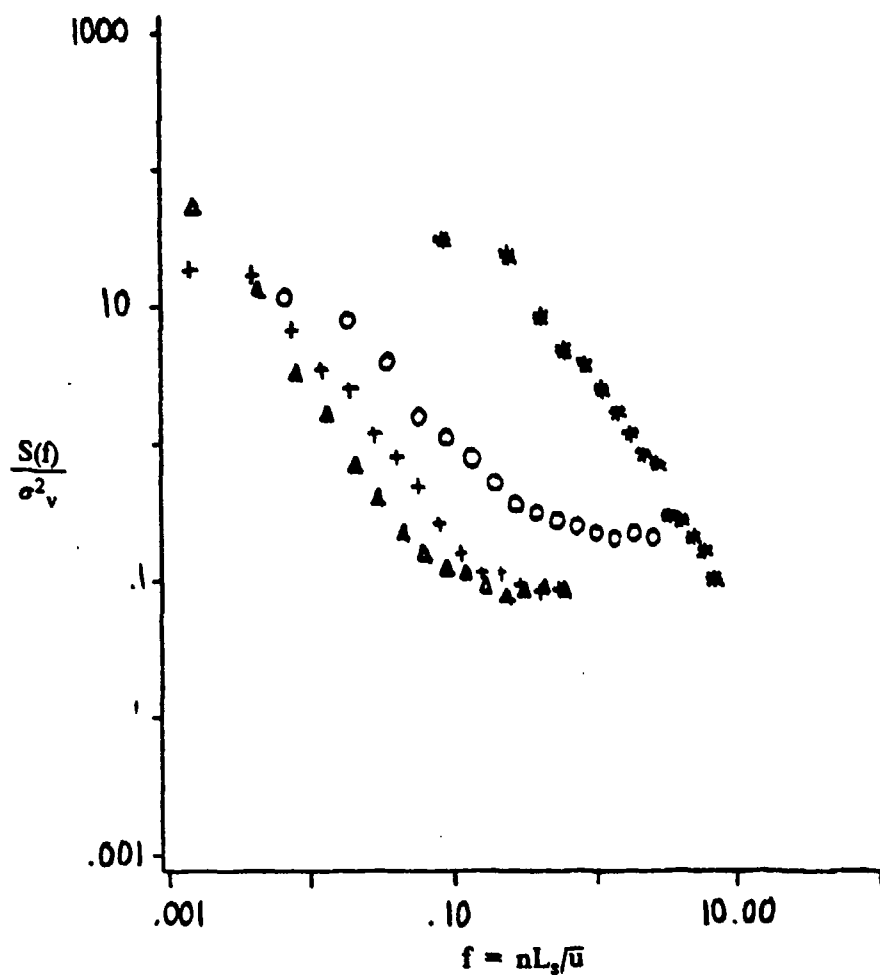


Fig. 46 Spectra of v' from vertical profile in the unfoliated canopy at $x=10$ with * at 24m, + at 16.5m, Δ at 11m and ○ at 3m. These spectra are 5 Hz ensemble averages of 10 consecutive 6 minute runs with edge fetch wins.

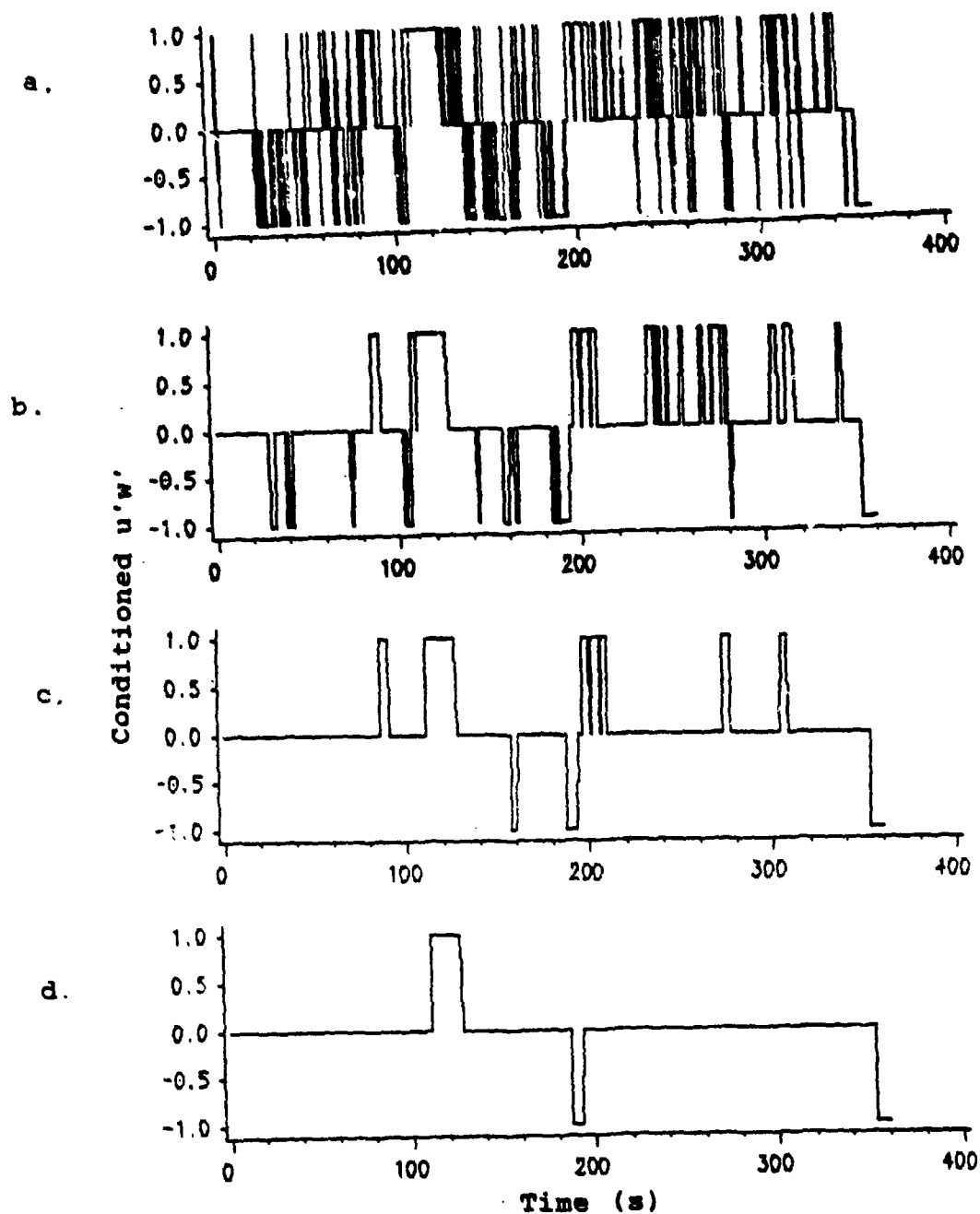


Fig. 47 This figure shows $u'w'$ conditioned by Eqn. 5.42. The four plots show the same series at coordinates 71,15 with hole size ≈ 1 and a gap of a) 0 b) 5 c) 15 and d) 25. This data was collected on 10/22/86.

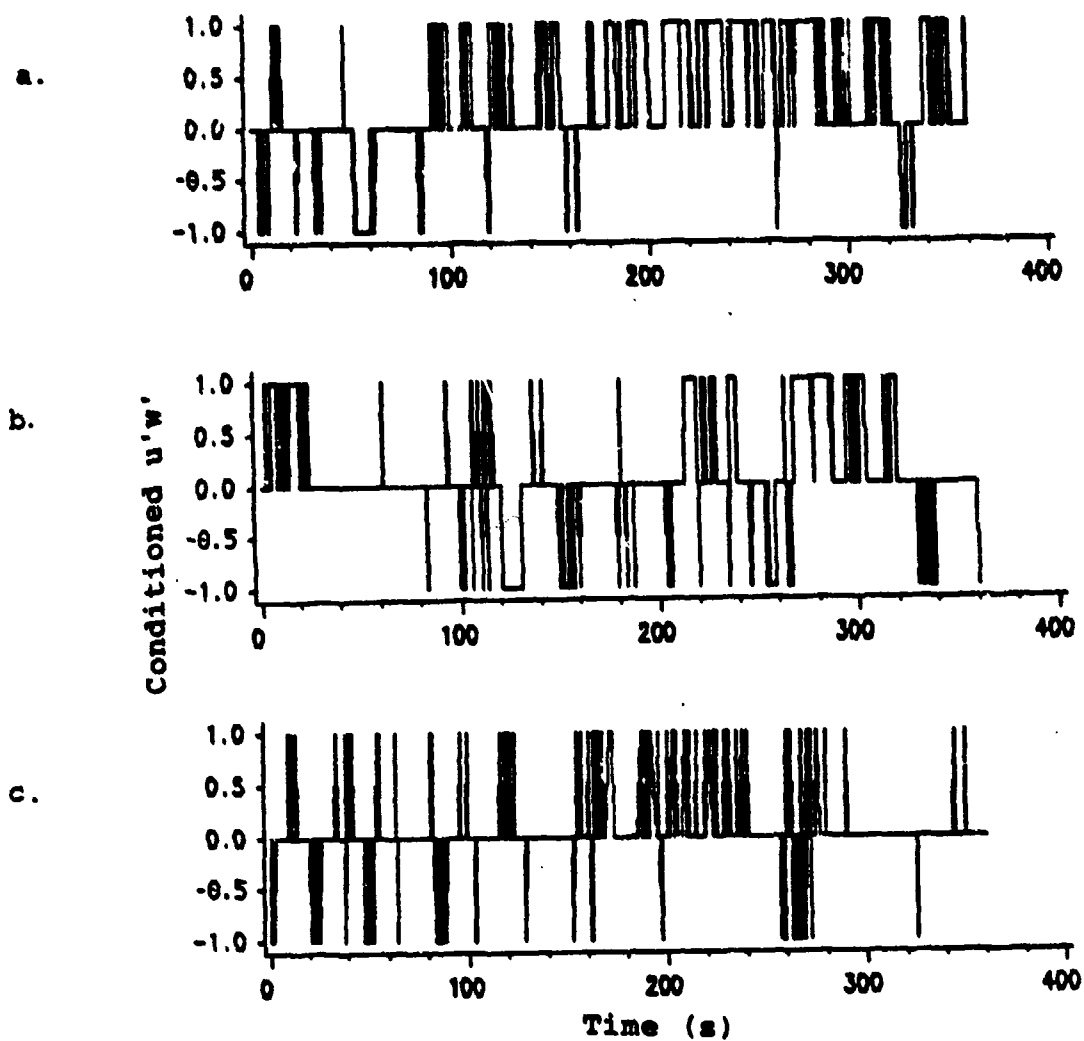


Fig. 48 This figure shows $u'w'$ conditioned by Eqn. 5.42 with hole size = 1 and a gap = 0 at simultaneous data coordinates a) 10,16.5 b) 10,11 c) 10,3. This data was collected in the unfoliated canopy on 11/18/86.

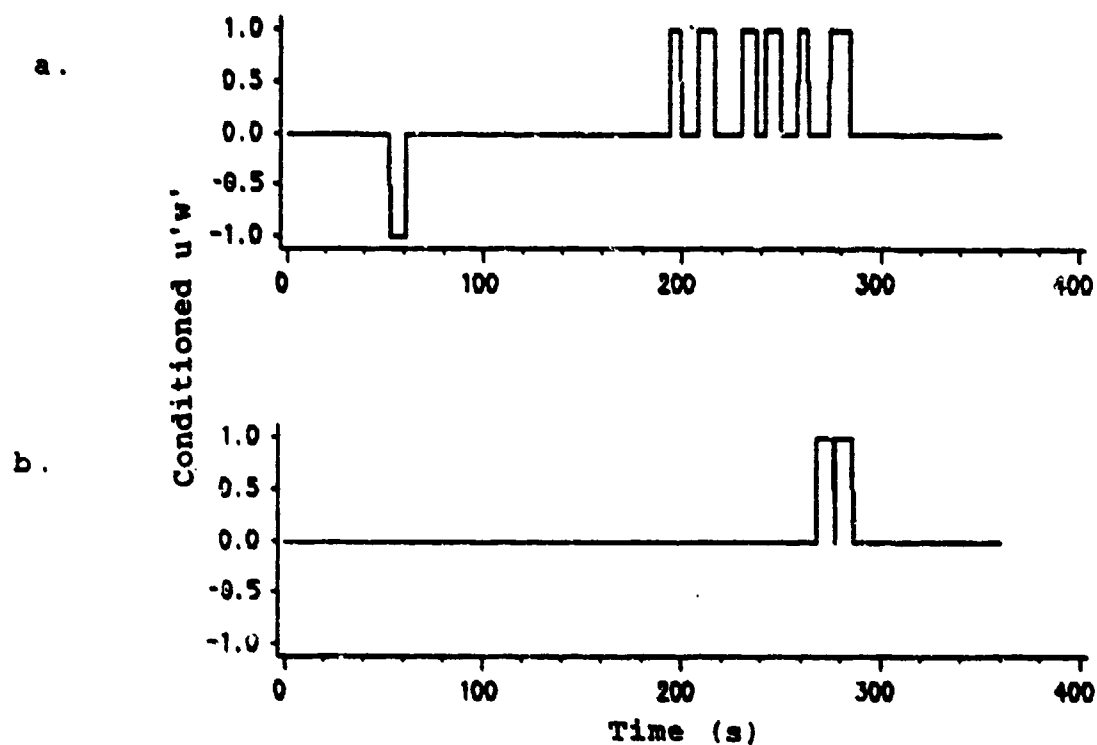


Fig. 49 This figure shows $u'w'$ conditioned by Eqn 5.42 with hole size = 1 and gap = 25 in simultaneous data at coordinates a) 10,16.5 b) 10,11. This data was collected in the unfoliated canopy on 11/18/86. These are the same series shown in Fig. 48. Note there was no data meeting the filter criteria at coordinates 10,3.

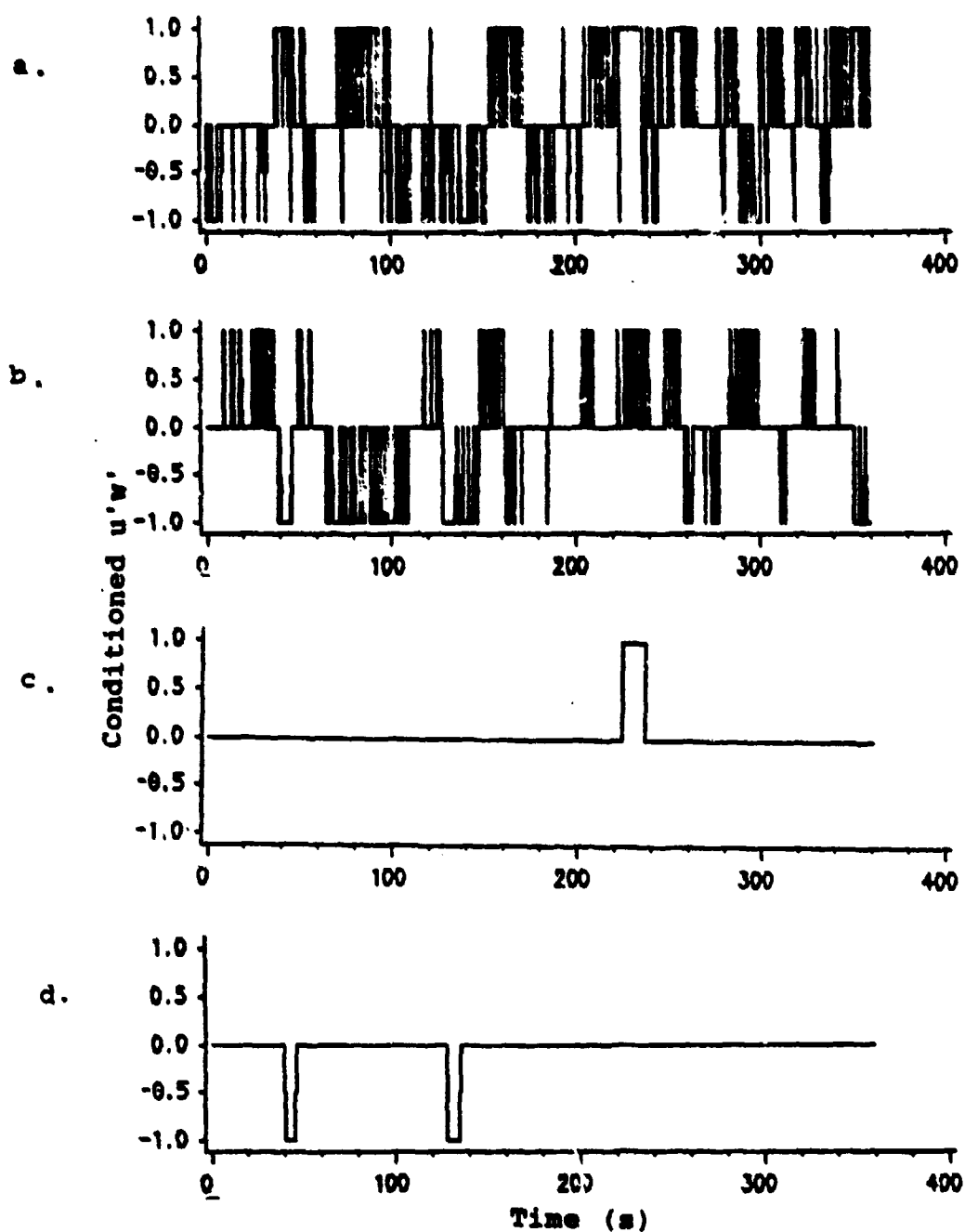


Fig 50 This figure shows $u'w'$ conditioned by Eqn 5.42 with hole size = 1 and a) coordinates 71,15 and gap = 0 b) coordinates 21,16.5 and gap = 0 c) coordinates 71,15 and gap = 25 and d) coordinates 21,16.5 and gap = 25. This data was collected simultaneously in foliated canopy on 9/11/86.

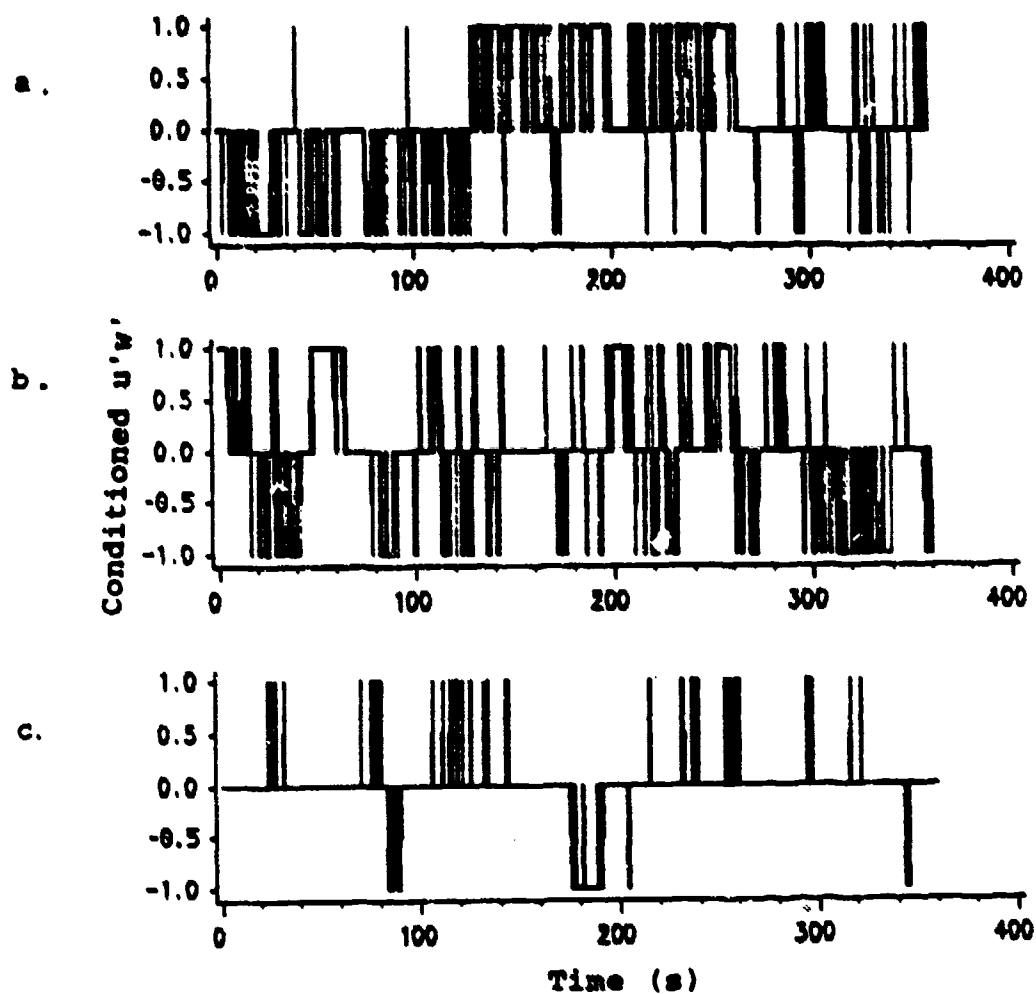


Fig. 51 This figure shows $u'w'$ conditioned by Eqn. 5.42 with hole size = 1 and gap = 0 at coordinates a) 71,3 b) 21,3 c) 10,3. This data is from the unfoliated canopy and was collected on 10/18/86.

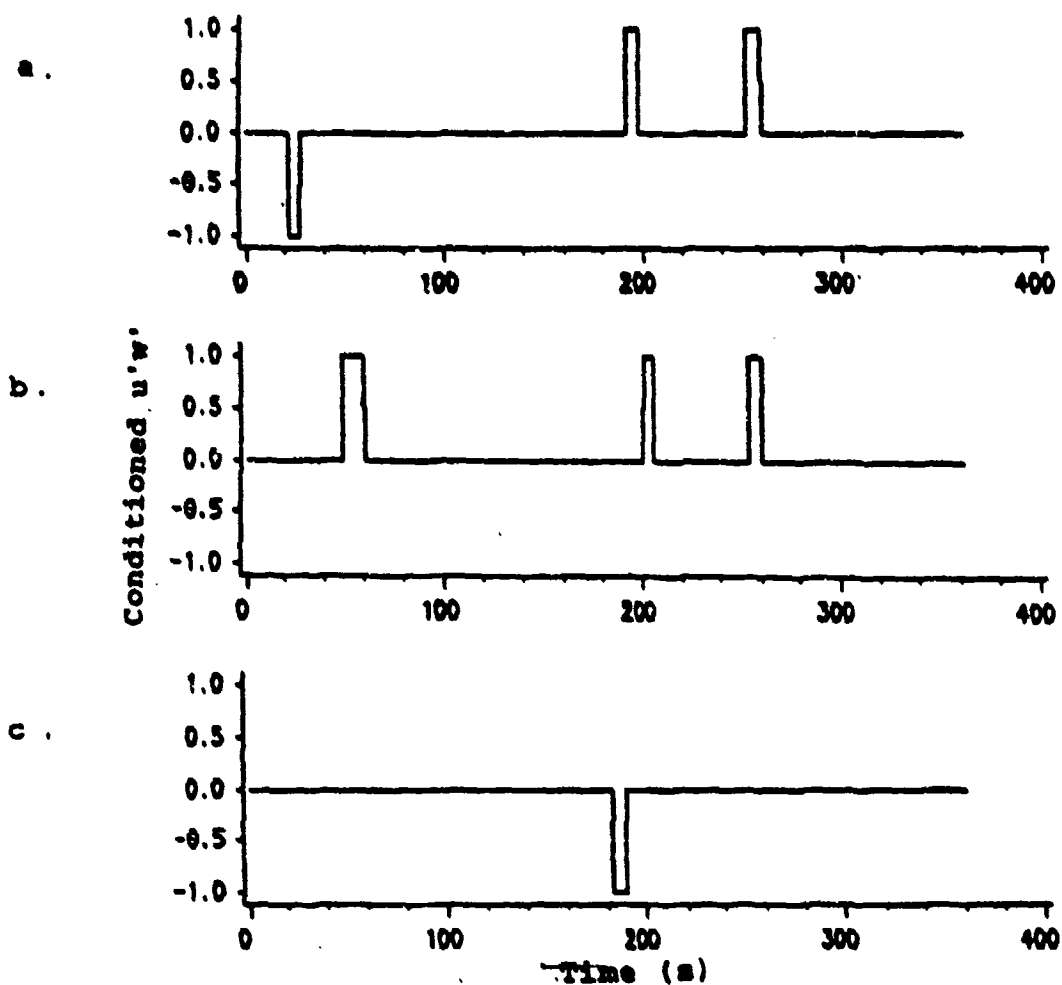


Fig 52 This figure shows $u'w'$ conditioned by Eqn 5.42 with hole size = 1 and gap = 25 at coordinates a) 71, 3 b) 21, 3 c) 10, 3. This data is from the unfoliated canopy and was collected on 10/18 86.

Chapter VII

Conclusions

Conclusions are mainly based on the comparison of foliated and unfoliated statistics to assess the role of the canopy and the comparison of in-canopy and out-of-canopy flows to assess the role of the edge.

The mean statistics indicate that canopy drag dissipates momentum and that this effect is proportional to LAI as expected. The edge provides a longitudinal source of momentum to in canopy, edge fetch flows as the wind penetrates the relatively low density trunk space. This causes a pronounced secondary maximum in the in-canopy velocity profiles in most foliated flows and some unfoliated flows. These flows show very high turbulent intensities, especially in the unfoliated trunk space which is due to eddy shedding by the trunks which is at detectable scales which are not quickly damped. This is contrasted with eddies shed by twigs and leaves which contribute less to the total variance and are quickly dissipated. These conclusions are confirmed by the spectral analysis.

The canopy drag coefficient is sensitive to LAI and mean velocity in this canopy. Values of canopy drag determined in this study agree well with the observations of other researchers. Generally, normalized dispersion is higher in the unfoliated canopy than in the foliated which corresponds to the observation that TI is highest in the unfoliated canopy.

Quadrant analysis confirms that the edge is an important source of to the in-canopy velocity field near the edge. Quadrants 1 and 3 often show a large percentage time fraction, even for strong momentum transfer events at in-canopy sensors at this edge site during edge fetch flows. Spectral analysis demonstrates that there are significant sources of high frequency turbulent production in the canopy. An in canopy length scale around .4m is indicated in a foliated canopy as the longest canopy scale. This length is also occasionally seen in the unfoliated canopy. Production also occurs at most lengths between .4m and f_{\max} in the foliated canopy. In the unfoliated canopy, the high frequency production occurs at more discrete lengths, though these vary between data sets, while in the foliated canopy the production is smeared over a greater range of lengths in a given data set. This .4m length is probably caused by clumps of leaves, higher frequencies are the result of trunks, branches, leaves and twigs. The smearing in the spectra seen in the foliated data are probably due to the fact that foliated vegetation accounts for a greater range of lengths than unfoliated vegetation. There are regions where $b = -5/3$ in most in canopy spectra. Also, the temperature spectra in canopy are smoother than the velocity spectra, indicating that the temperature field is more homogenous than the velocity field.

Finally, the structure analysis techniques discussed demonstrate the complex nature of individual gusts in the in and near-canopy flow field. This technique is still crude, but offers a tool for evaluating the nature of individual flow events.

Bibliography

- Acrivlellis, M. 'Hot-Wire Measurements in Flows of Low and High Turbulence Intensity' DISA Information No. 22 Dec. 1977 15-20
- Albini, F.A. 'A Phenomenological Model for Wind Speed and Shear Stress Profiles in Vegetation Cover Layers' Jour. App. Met. 20 1981 1325-1335
- Allen L.H. 'Turbulence and Wind Speed Spectra within a Japanese Larch Plantation' Jour. of App. Met. Vol. 7, 1968 73-78
- Anderson, D.E., Verma, S.B., Clement, R.J., Baldocchi, D.D. and Matt, D. R. 'Turbulence of Spectra of CO₂, Water Vapor, Temperature and Velocity Over a Deciduous Forest' Ag. and Forest Met. 38 (1986) 81-99
- Armi, L. and Flament, P. 'Cautionary Remarks on the Spectral Interpretation of Turbulent Flows' JGR 90(C6) pp. 11789-11782 Nov. 20, 1982
- Arya, S.P.S. and Gadiyaram, P.S. 'An Experimental Study of Flow and Dispersion in the Wakes of Three Dimensional Low Hills' Atmospheric Environment 20 #4 1986 729-740
- Aydin, M. and Leutheusser, H.J.
'Very Low Velocity Calibration and Application of Hot-Wire Probes'
DISA Information No. 25 Feb. 1980 17-18
- Bache, D.H. 'Momentum Transfer to Plant Canopies: Influence of Structure and Variable Drag' Atmospheric Environment 20 #7 1369-1378
- Baldocchi, D.D., Verma, S.B. and Rosenberg, N.J. 'Characteristics of Airflow Above and Within Soybean Canopies' Boundary Layer Met. 25 1983 43-54
- Baldocchi, D.D. and Hutchison, B.A. 'Turbulence in an Almond Orchard: Vertical Variations in Turbulent Statistics' ATDD Contribution #86/23 Wind/3 1986

- Batchelor G.K. The Theory of Homogenous Turbulence Cambridge University Press, London 1953
- Bowen, A.J. and Teunissen, H.W. 'Correction Factors for the Directional Response of Gill Propeller Anemometers' *Boundary Layer Met.* 37 #4 1986 407-413
- Businger, J.A. 'Equations and Concepts' Nieuwstadt, F.T.M Ed. and van Dop H. Ed. Atmospheric Turbulence and Air Pollution Modelling D. Reidel Publishing Co. Boston 1982
- Caughey, S.J. 'Observed Characteristics of the Atmospheric Boundary Layer' Nieuwstadt, F.T.M Ed. and van Dop H. Ed. Atmospheric Turbulence and Air Pollution Modelling D. Reidel Publishing Co. Boston 1982
- Chen, C.P. and Blackwelder, R.F. 'Large-Scale Motion in a Turbulent Boundary Layer: A Study Using Temperature Contamination' *Jour. of Fluid Mechanics* Vol. 89 Part 1 1978 1-31
- Cionco, R. 'A Preliminary Model for Air Flow in the Vegetative Canopy' *Bull. Amer. Met. Soc.* 43 p. 319 1962
- Cionco, R. 'A Mathematical Model for Air Flow in a Vegetative Canopy' *Jour. of App. Met.* Vol. 4 Aug. 1965 pp. 517-522
- Cionco, R. 'Modeling Windfields and Surface Layer Wind Profiles Over Complex Terrain and Within Vegetative Canopies' The Forest-Atmosphere Interaction Hutchison, B.A., Ed. and Hicks, B.B., Ed. D. Reidel Publishing Co. Boston 1985
- Claussen, M. 'A Model of Turbulence Spectra in the Atmospheric Surface Layer' *Boundary Layer Met.* 33 1985 151-172
- Claussen, M. 'Estimation of the Monin-Obukov Similarity Functions From a Spectral Model' *Boundary Layer Met.* 33 1985 233-243
- Cooley, J.W. Lewis, P.A.W. and Welch, P.D. 'The Fast Fourier Transform and its Application to Time Series Analysis' Statistical Methods for Digital Computers Vol. III Enslein, K. Ralston, A. and Wilf, H. Ed. John Wiley and Sons, New York pp 377-423
- Coppin, P.A., Raupach, M.R. and Legg, B.J. 'Experiments on Scalar Dispersion in a Model Plant Canopy Part II: An Elevated Plane Source' *Boundary Layer Met.* 35 1986 167-191
- Denmead, O.T. and Bradley, E.F. 'Flux-Gradient Relationships in a Forest Canopy' The Forest Atmosphere Interaction Hutchison, B.A. Ed. and Hicks, B.B. Ed. D. Reidel Publishing Co., Boston 1985
- Diefenderfer, A.J. Principles of Electronic Instrumentation Saunders College Publishing, New York 1979
- Dolman, A.J. 'Estimates of Roughness Length and Zero Plane Displacement for a Foliated and Non-Foliated Oak Canopy' *Ag. and Forest Met.* 36 1986 241-248

- Finnigan, J.J. 'Turbulence in Waving Wheat 1. Mean Statistics and Honami' Boundary Layer Met. 16 1979 181-211
- Finnigan, J.J. 'Turbulent Transport in Flexible Plant Canopies' The Forest Atmosphere Interaction Hutchison, B.A. Ed. and Hicks, B.B. Ed. D. Reidel Publishing Co., Boston 1985
- Garratt, J.R. 'Surface Influence Upon Vertical Profiles in the Atmospheric Near Surface Layer' Quart. Jour. Roy. Met. Soc. 106 1980 803-819
- Gash, J.H.C. 'Observations of Turbulence Downwind of a Forest-Heath Interface' Boundary Layer Met. 36 #3 228-237
- Gaulier, C. 'Measurement of Air Velocity by Means of a Triple Hot-Wire Probe' DISA Information No. 21 April, 1977
- Grant, R.H. 'The Scaling of Flow in Vegetative Structures' Boundary Layer Met. 27 1983 171-184
- Grant, R.H. 'The Mutual Interference of Spruce Canopy Structural Elements' Ag. and Forest Met. 32 1984 145-156
- Haan, C.T. Statistical Methods in Hydrology The Iowa State University Press, Ames IA 1977
- Hayashi, Y. 'Observational Aspects on a Dominant Spectral Frequency in an Airflow Over a Weeping-Lovegrass Stand' Boundary Layer Met. 36 #3 1986 239-243
- Hicks, B.B. 'An Examination of Turbulence Statistics in the Surface Boundary Layer' BLM 21 1981 389-402
- Hicks, B.B. 'Behavior of Turbulence Statistics in the Convective Boundary Layer' J. of Clim. and App. Met. Vol. 24 #6 June 1985 pp 607-614
- Hojstrup, J. 'A Simple Model for the Adjustment of Velocity Spectra in Unstable Conditions Downstream of an Abrupt Change in Roughness and Heat Flux' Boundary Layer Met. 21 1981 341-356
- Hojstrup, J. 'Velocity Spectra in the Unstable Planetary Boundary Layer' Jour. Atmos. Sci. 39 1982 2239-2248
- Holtstag, A.A.M. and Nieuwstadt, F.T.M. 'Scaling the Atmospheric Boundary Layer' Boundary Layer Met. 36 #1/2 1986 201-209
- Horst, T.W. 'Correcting for Response Errors in a Three-Component Propeller Anemometer' J. App. Met. 12 #4 June 1973 pp 716-725
- Hunt, J.C.R. and Richards, K. 'Stratified Airflow Over One or Two Hills' Boundary Layer Met. 30 1985 223-259
- Irwin, H.P.A.H. 'Cross-Spectra of Turbulence Velocities in Isotropic Turbulence' Boundary Layer Met. 16 1979 237-243

- Jenkins, G.M. and Watts, D.G. Spectral Analysis and Its Applications Holden-Day Toronto 1968
- Jones, R.M. and Hooke, W.H. 'The Perturbed Structure of the Neutral Atmospheric Boundary Layer Over Irregular Terrain: I. Model Formulation' Boundary Layer Met. 36 1986 395-416
- Jones, R.M. and Hooke, W.H. 'The Perturbed Structure of the Neutral Atmospheric Boundary Layer Over Irregular Terrain: II. Model Calculations' Boundary Layer Met. 37 #1/2 1986 107-127
- Kaimal, J.C., Wyngaard, J.C., Izumi, Y. and Cote', O.R. 'Spectral Characteristics of Surface-Layer Turbulence' Quart. Jour. Roy. Met. Soc. Vol. 98 No. 417 July, 1972
- Kaimal, J.C., Wyngaard, J.C., Haugen, D.A., Cote, O.R., Izumi, Y., Caughey, S.J. and Readings, C.J. 'Turbulence Structure in the Convective Boundary Layer' Jour. Atmos. Sci. 33 1976 2152-2169
- Kaimal, J.C. 'Horizontal Velocity Spectra in an Unstable Surface Layer' J. Atmos. Sci. 35 1978 18-24
- Kaimal, J.C., Eversole, R.A., Lenschow, D.H., Stankov, B.B., Kahn, P.H., and Businger, J.A. 'Spectral Characteristics of the Convective Boundary Layer Over Uneven Terrain' J. Atmos. Sci. 39 #5 1982 1098-1114
- LI: Kristensen, L. and Jensen, N.O. 'Lateral Coherence in Isotropic Turbulence and in the Natural Wind' Boundary Layer Met. 17 1979 353-373
- Larsen, S.E. and Busch, N.E. 'On the Humidity Sensitivity of Hot-Wire Measurements' DISA Information No. 25 Feb. 1980 4-5
- Legg, B.J., Raupach, M.R. and Coppin, P.A. 'Experiments on Scalar Dispersion Within a Model Plant Canopy Part III: An Elevated Line Source' Boundary Layer Met. 35 1986 277-302
- LeMone, M.A. 'The Structure and Dynamics of Horizontal Roll Vortices in the PBL' Jour. Atmos. Sci. 30 1973 1077-1091
- Li, Z.J. 'A Numerical Model of Air Flow Through and Over a Forest Canopy Edge' M.S. Thesis, Civil Engineering Department, University of Connecticut 1982
- Li, Z.J., Miller, D.R. and Lin, J.D. 'A First-Order Closure Scheme to Describe Counter-Gradient Momentum Transport in Plant Canopies' Boundary Layer Met. 33 1985 77-83
- Lin, J.D., Miller, D.R., Li, Z.J. and Sun, S.F. 'Three Dimensional Hot Film Sensors for Turbulent Flow Measurements in Plant Canopies' 17th Conf. Agr. and For. Met., AMS Scottsdale, AZ 1985 183-184
- Lin, J.D. and Miller, D.R. 'A Preliminary Field Study of Turbulent Flow Over and Inside a Forest Edge' Interim Technical Report USARO 1985

- Lindroth, A. 'Gradient Distributions and Flux Profile Relations Above a Rough Forest' *Quart. Jour. Roy. Met. Soc.* 110 1984 553-563
- Lomas, C.G. Fundamentals of Hot Wire Anemometry Cambridge University Press New York 1986
- Lumley, J.L. and Panofsky, H.A. The Structure of Atmospheric Turbulence John Wiley and Sons New York 1964
- Lumley, J.L. 'Pressure Strain Correlation' *Physics of Fluids* 18 1975 750
- Machen, P.C. 'Correction of Unlinearized Hot-Film Anemometer Measurements for Ambient Temperature Changes' *DANTEC Information* No. 3 Sept. 1986 8-9
- Maitani, T. and Seo, T. 'A Case Study of Temperature Fluctuations Within and Above a Wheat Field Before and After Sunset' *Boundary Layer Met.* 35 1986
- Mardia, K.V. Statistics of Directional Data Academic Press London 1972 357
- Martinez-Val, R., Jimenez, J. and Rebollo, M. 'Sensor Contamination Effects in Hot-Wire Anemometry in Air' *DISA Information* No. 27 Jan. 1982 12-14
- Mason, P.J. and Sykes, R.I. 'Flow Over an Isolated Hill of Moderate Slope' *Quart. Jour. Roy. Met. Soc.* 105 1979 383-395
- Mason, P.J. 'Flow Over the Summit of an Isolated Hill' *Boundary Layer Met.* 37 #4 1986 385-405
- Massman, W.J. 'Mass and Heat Transfer To and From Vegetated Surfaces: An Analytical Approach' June, 1986 Unpublished
- Massman, W.J. 'A Comparative Study of Some Simple Mathematical Models of the Mean Wind Structure Within and the Aerodynamic Drag of Plant Canopies' July, 1986 Submitted to *Boundary Layer Met.*
- Meyers, T. and Paw U, K.T. 'Testing of a Higher Order Closure Model for Modeling Airflow Within and Above Plant Canopies' *Boundary Layer Met.* 37 #3 1986 297-311
- Miller, D.R. and Lin, J.D. 'Canopy Architecture of a Red Maple Edge Stand Measured by a Point Drop Method' The Forest-Atmosphere Interaction Ed. Hutchison, B.A. and Hicks, B.B. D. Reidel Publishing Co. Boston 1985
- Miyake, M., Stewart, R.W. and Burling, R.W. 'Spectra and Cospectra of Turbulence Over Water' *Quart. Jour. Roy. Met. Soc.* 96 1970 138-143
- Moeng, C.H. 'A Large Eddy Simulation for the Study of Planetary Boundary Layer Turbulence' *Jour. Atmos. Sci.* 41 1984 2052-2062
- Moore, C.J. 'Frequency Response Corrections for Eddy Correlation Systems' *Boundary Layer Met.* 37 #1/2 1986 17-35

- Mori, Y. 'Evaluation of Several "Single-Pass" Estimators of the Mean and the Standard Deviation of Wind Direction' Jour. of Clim. and App. Met. 25 #10 1387-1397
- Nieuwstadt, F.T.M Ed. and van Dop H. Ed. Atmospheric Turbulence and Air Pollution Modelling D. Reidel Publishing Co. Boston 1982
- Panofsky, H.A. 'Matching in the Convective Planetary Boundary Layer' Jour. Atmos. Sci. 35 1978 272-276
- Panofsky, H.A., Larko, D., Lipshutz, R. and Stone, G. 'Spectra of Velocity Components Over Complex Terrain' Quart. J. R. Met. Soc. 108 1982 215-230
- Panofsky, H.A. and Dutton, J.A. Atmospheric Turbulence: Models and Methods for Engineering Applications John Wiley and Sons New York 1984
- Priestly, M.B. Spectral Analysis and Time Series Vol. 2: Multivariate Series, Prediction and Control Academic Press New York 1981
- Raupach, M.R. and Thom, A.S. 'Turbulence in and Above Plant Canopies' Annual Review of Fluid Mechanics 1981 13 97-129
- Raupach, M.R. and Shaw, R.H. 'Averaging Procedures for Flow Within Vegetative Canopies' Boundary Layer Met. 22 1982 79-90
- Raupach, M.R., Coppin, P.A. and Legg, B.J. 'Experiments on Scalar Dispersion Within a Model Plant Canopy Part 1: The Turbulent Structure' Boundary Layer Met. 35 1986 21-52
- Rosenberg, N.J. Microclimate: The Biological Environment Wiley-Interscience Publication John Wiley and Sons, NY 1974
- Schols, J.L.J. 'The Determination of Turbulent Structures in the Atmospheric Surface Layer' PhD. Dissertation, Dept. of Physics and Meteorology, Agricultural University of Wageningen Dec. 1984
- Seginer, I., Mulhearn, P.J., Bradley, E.F. and Finnigan, J.J. 'Turbulent Flow in a Model Plant Canopy' Boundary Layer Met. 10 1976 423-453
- Seifert, G. and Graichen, K. 'A Calibration Method for Hot-Wire Probes Including the Low Velocity Range' DISA Information No. 27 Jan. 1982 8-11
- Shaw, R.H., Silversides, R.H. and Thurtell, G.W. 'Some Observations of Turbulence and Turbulent Transport Within and Above Plant Canopies' Boundary Layer Met. 5 1974 429-449
- Shaw, R.H., Ward, D.P. and Aylor, D.E. 'Frequency of Occurrence of Fast Gusts of Wind Inside a Corn Canopy' Jour. App. Met. Vol. 18 No. 2 Feb. 1979
- Shaw, R.H., Tavanger, J. and Ward, D.P. 'Structure of the Reynolds Stress in a Canopy Layer' Jour. Clim. and App. Met. 22 1983 1922-1931

- Shaw, R.H. 'On Diffusive and Dispersive Fluxes in Forest Canopies' The Forest-Atmosphere Interaction Hutchison, B.A., Ed. and Hicks, B.B., Ed. D. Reidel Publishing Co. Boston 1985
- Shaw, R.H. and McCartney, H.A. 'Gust Penetration into Plant Canopies' *Atmospheric Environment* Vol. 19 #5 1985
- Shaw, R.H., den Hartog, G. and Neumann, H.H. 'Observation of Deciduous Forest Turbulence and the Influence of Leaf Area Index and Thermal Stability' *Proceedings of the AMS 18th Conference of Agricultural and Forest Meteorology* 1987
- Silversides, R.H. 'On Scaling Parameters for Turbulence Spectra Within Plant Canopies' *Ag. Met.* 13 1974 203-211
- Smedman, A. and Bergstrom, H. 'Flow Characteristics Above a Very Low and Gently Sloping Hill' *Boundary Layer Met.* 29 1984 21-37
- Tan-atichat, J. and George, W.K. 'Use of Computer for Data Acquisition and Processing' Handbook of Fluids and Fluid Machinery Fuhs, A.E. Ed. John Wiley and Sons, To be Published
- Taylor, P.A., Walmsley, J.L. and Salmon, J.R. 'A Simple Model of Neutrally Stratified Boundary Layer Flow Over Real Terrain Incorporating Wavenumber Scaling' *Boundary Layer Met.* 26 1983 169-189.
- Tennekes, H. and Lumley, J.L. A First Course in Turbulence MIT Press Cambridge MA 1972
- Thompson, N. 'Turbulence Measurement Above a Pine Forest' *Boundary Layer Met.* 16 1979 293-310
- Verma, S.B., Baldocchi, D.D., Anderson, D.E., Matt, D.R. and Clement, R. J. 'Eddy Fluxes of CO₂, Water Vapor and Sensible Heat Over a Deciduous Forest' *BLM* 36 (1986) 71-91
- Walmsley, J.L., Taylor, P.A. and Keith, T. 'A Simple Model of Neutrally Stratified Boundary-Layer Flow Over Complex Terrain With Surface Roughness Modulations (MS3DJII/3R)' *Boundary Layer Met.* 36 #1/2 1986 157-186
- Wang, Y.S. 'Quantification of a Red Maple Forest Canopy' M.S. Thesis Renewable Natural Resources Dept. University of Connecticut 1985
- Wang, Y.S. and Miller, D.R. 'Calibration of the Hemispherical Photographic Technique to Measure Leaf Area Index Distributions in Hardwood Forests' *Forest Science* March 1987
- Wilson, N.R. and Shaw, R.H. 'A Higher Order Closure Model for Canopy Flow' *Jour. of App. Met.* Vol. 18 No. 2 Feb. 1977
- Wyngaard, J.C. 'Boundary Layer Modeling' Nieuwstadt, F.T.M Ed. and van Dop H. Ed. Atmospheric Turbulence and Air Pollution Modelling D. Reidel Publishing Co. Boston 1982

Zank, I. 'Sources of Error and Running Calibration of Three-Dimensional Hot-Film Anemometers Especially Near the Sea Surface' DISA Information No. 26
Feb. 1981 11-18

Appendix A Software Systems

The computer system used in these experiments was purchased from Data-Translation Inc. and is marketed with a set of modular, Fortran, device access subroutines which provide access to the $D \rightarrow D$ and some control of sampling modes. Initially, a set of sampling software which accessed the Data-Translation routines and provided interactive control of sampling parameters was put-up on the system by Wildfire Software, Inc. As is typically the case using packaged software in a specialized application, the existing software had to be modified and and expanded to fit the specialized needs. Since all analysis could not be performed on the LSI 11/23, a link to The University of Connecticut main frame computer (IBM 3084) had to be established.

The sampling program is named REC64 and is a modified version of a Wildfire Software program. REC64 is a Fortran program which accesses Data Translation subroutines and provides a menu of sampling options. The user controls frequency, length of block, number of blocks, channels sampled (up to 64), etc. The program also allows a brief description of the run to be entered as text and sensor identifications to be associated with the corresponding channel. For instance, channel 1

may be associated with F 31 which would mean the signal from wire 1 of TFWOES 23 is on channel 1. This feature became the heart of the system, as channel tags associated sensors and channels throughout the processing routines. This program yielded mean statistics to the screen for inspection and allowed the data set to be stored if desired. Credit for development of the DEC-IBM transfer software is given to Mr. John Sieval who developed a coherent, flexible system for data transfer and access. The first step was to write code that allowed an automated transfer to tape of multiple files, in a format easily accessible to the IBM. This was accomplished by a program named WLDWND which allows up to 20 files to be reformatted and moved to 9-track tapes in a given run. Sieval then expanded on code written by the author on the IBM and the calibration program as coded by Mr. Wang, to translate the DEC format tapes to yield data files of physical quantities on IBM system disk packs.

This is accomplished in two steps. First, the tape is catalogued on the IBM system as a non-labeled, read only tape. Next, the system exec named LODIND is run on the IBM. This exec reads a specified tape and creates an index file which contains sensor, channel and run information as specified in REC64, for each data file on tape. The second step is to run a system exec named LODDAT. This exec associates a specified calibration file with data in a specified data set and completes all voltage to physical quantity conversions by associating calibration polynomials in the calibration file, which are identified by sensor IDs, with sensor IDs in the index file which designate channels. The calibration polynomials require zero voltages for both the triple-films and the WOES channels. In REC64, runs are designated as zero runs and this information is now available to the calibration file by way of the index file. Average zero run voltages are actually calculated in the calibration program. LODDAT accesses the last zero run that was loaded when the zero values

are required. The final step performed by the LODDAT exec is a write to system user disk where the data is accessible to analysis programs. Some associated software was also written, such as an interactive PRTVOL exec which will dump raw voltages to the screen, and a similar PRTDAT exec. These peripheral programs were primarily used to troubleshoot the system and were not often used after the system had been tested.